

NASA Technical Paper 1861

Design and Experimental Results
for a Natural-Laminar-Flow Airfoil
for General Aviation Applications

Dan M. Somers

JUNE 1981

CASE FILE
COPY

NASA

NASA Technical Paper 1861

Design and Experimental Results
for a Natural-Laminar-Flow Airfoil
for General Aviation Applications

Dan M. Somers
Langley Research Center
Hampton, Virginia

NASA

National Aeronautics
and Space Administration

**Scientific and Technical
Information Branch**

1981

Use of trade names or names of manufacturers in this report does not constitute an official endorsement of such products or manufacturers, either expressed or implied, by the National Aeronautics and Space Administration.

SYMBOLS

Values are given in both SI and U.S. Customary Units. Measurements and calculations were made in U.S. Customary Units.

C_p	pressure coefficient, $\frac{p_l - p_\infty}{q_\infty}$
c	airfoil chord, cm (in.)
c_c	section chord-force coefficient, $\oint C_p d\left(\frac{z}{c}\right)$
c_d	section profile-drag coefficient, $\int_{\text{Wake}} c_d' d\left(\frac{h}{c}\right)$
c_d'	point drag coefficient (ref. 10)
c_l	section lift coefficient, $c_n \cos \alpha - c_c \sin \alpha$
c_m	section pitching-moment coefficient about quarter-chord point, $-\oint C_p \left(\frac{x}{c} - 0.25\right) d\left(\frac{x}{c}\right) + \oint C_p \left(\frac{z}{c}\right) d\left(\frac{z}{c}\right)$
c_n	section normal-force coefficient, $-\oint C_p d\left(\frac{x}{c}\right)$
h	vertical height in wake profile, cm (in.)
M	free-stream Mach number
p	static pressure, Pa (lbf/ft ²)
q	dynamic pressure, Pa (lbf/ft ²)
R	Reynolds number based on free-stream conditions and airfoil chord
t	airfoil thickness, cm (in.)
x	airfoil abscissa, cm (in.)
z	airfoil ordinate, cm (in.)
α	angle of attack relative to chord line, deg

INTRODUCTION

Research on advanced-technology airfoils for general aviation applications has received considerable attention over the past decade at the NASA Langley Research Center. The initial emphasis in this research program was on the design and testing of turbulent-flow airfoils with the basic objective of producing a series of airfoils which could achieve higher maximum lift coefficients than the airfoils in use on general aviation airplanes at that time. For this series of airfoils, it was assumed that the flow over the entire airfoil would be turbulent, primarily because of the construction techniques in use (mostly riveted sheet metal). A summary of this work is presented in reference 1. While these new NASA low-speed airfoils did achieve higher maximum lift coefficients, the cruise drag coefficients were no lower than the earlier NACA four- and five-digit airfoils. Accordingly, the emphasis in the research program has been shifted toward natural-laminar-flow (NLF) airfoils in an attempt to obtain lower cruise drag coefficients while retaining the high maximum lift coefficients of the new NASA airfoils. In this report, the term "natural-laminar-flow airfoil" refers to an airfoil which can achieve significant extents of laminar flow (≥ 30 -percent chord) solely through favorable pressure gradients (no boundary-layer suction or cooling).

Research on natural-laminar-flow airfoils dates back to the late 1930's at the National Advisory Committee for Aeronautics (NACA). (See ref. 2.) The work at NACA was culminated with the 6-series airfoils (ref. 3). The 6-series airfoils were not generally successful as low-drag airfoils, however, because of the construction techniques available at the time.

The advent of composite structures has led to a resurgence in NLF research. The initial applications were sailplanes, but recently, a number of powered general aviation airplanes have been constructed of composites - most notably, the Bellanca Skyrocket II (ref. 4) and the Windecker Eagle (ref. 5). In Europe, powered composite airplanes have also been produced. One such aircraft, the LFU 205, used an NLF airfoil specifically tailored for its mission (ref. 6).

Thus, the introduction of composite construction has allowed aerodynamicists to design NLF airfoils which achieve, in flight, the low-drag characteristics measured in the wind tunnel (ref. 7). The goal of the present research on NLF airfoils at Langley Research Center is to combine the high maximum lift capability of the NASA low-speed airfoils with the low-drag characteristics of the NACA 6-series airfoils.

As part of the present research, an NLF airfoil has been designed using the method of reference 8. An experimental investigation was then conducted in the Langley Low-Turbulence Pressure Tunnel (LTPT) (ref. 9) to obtain the basic, low-speed, two-dimensional aerodynamic characteristics of the airfoil. The results have been compared with the predictions from the method of reference 8 and also with data from the LTPT for other laminar-flow, as well as turbulent-flow, airfoils.

Subscripts:

l	local point on airfoil
max	maximum
min	minimum
T	transition
∞	free-stream conditions

Abbreviations:

ls	lower surface
LTPT	Langley Low-Turbulence Pressure Tunnel
NLF	natural laminar flow
us	upper surface

AIRFOIL DESIGN

OBJECTIVES AND CONSTRAINTS

The target application for this airfoil is an advanced, light, single-engine, general aviation airplane. For this application, low profile-drag coefficients c_d at a Reynolds number R of about 4.0×10^6 are desirable for the cruise lift coefficient ($c_l = 0.4$) as well as for the climb lift coefficients ($c_l = 0.5$ to 1.0).

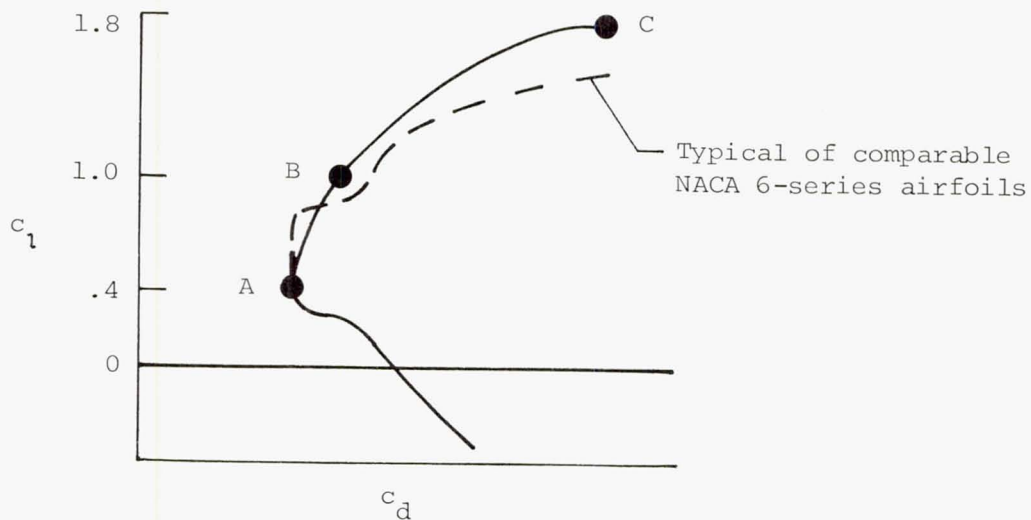
Two objectives were identified for this airfoil. The first objective was to design an airfoil which would produce a maximum lift coefficient $c_{l,max}$ at $R = 3.0 \times 10^6$ at least as great as that of the LS(1)-0413 (formerly, GA(W)-2) airfoil (i.e., $c_{l,max} \geq 1.76$). (See ref. 11.) A requirement related to the first objective was that $c_{l,max}$ not decrease with transition fixed near the leading edge on both surfaces. This means that the maximum lift coefficient cannot depend on the achievement of laminar flow. Thus, if the leading edge of the wing is contaminated by insect remains or other matter, the $c_{l,max}$ should not decrease. This requirement is set by safety considerations relating to stall and, therefore, landing speeds. The second objective was to obtain profile-drag coefficients for the cruise lift coefficient of 0.4 similar to those achieved by comparable NACA 6-series airfoils. In addition, profile-drag coefficients lower than those typical of comparable laminar-flow or turbulent-flow airfoils were desired for $c_l = 1$.

To further define the airfoil, three constraints were placed on this design. First, the extent of the favorable pressure gradient (decreasing pressure coefficient C_p with increasing x/c) on the upper surface was not to exceed 30-percent chord at the cruise lift coefficient. Second, the airfoil

thickness t/c must be greater than 12 percent. Third, the pitching-moment coefficient c_m should be no more negative than that of the LS(1)-0413. Thus, for $c_l = 0$, $c_m \geq -0.10$. (See ref. 11.)

PHILOSOPHY

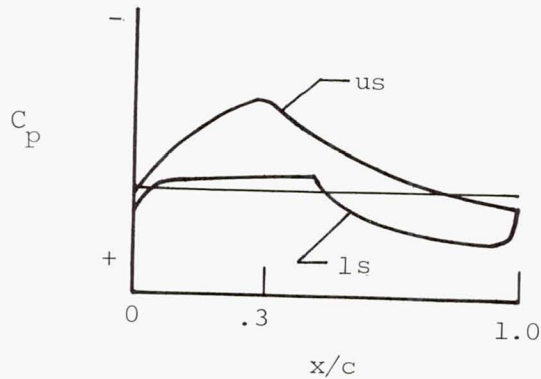
Given the previously mentioned objectives and constraints, certain characteristics of the design are evident. The following sketch illustrates the desired plot of c_l versus c_d which meets the goals for this design.



Sketch 1

The desired airfoil shape can be related to the pressure distributions which occur at the various lift coefficients shown in the sketch. Point A is the cruise condition ($c_l = 0.4$) where c_d is the lowest. The value of c_d for this point is determined by the constraint on the extent of the favorable pressure gradient on the upper surface ($(x/c)_{US} \leq 0.30$) and by the extent of the favorable pressure gradient on the lower surface (unconstrained). For this design, there is little aerodynamic advantage in achieving low drag below the cruise lift coefficient. If low drag were desired below the cruise lift coefficient, the maximum lift coefficient (point C) would be decreased by a roughly proportionate amount because of the required reduction in camber. Notice that there is relatively low drag at point B ($c_l = 1.0$), although not as low as at point A (cruise). This feature is quite important because it shows that the transition point on the upper surface moves slowly and steadily toward the leading edge with increasing c_l , as opposed to the sudden jump characteristic of the NACA 6-series airfoils. This sudden jump results in a rapid increase in drag at the upper limit of the low-drag range as shown in sketch 1. A slow and steady movement of the transition point, however, leads to an airfoil with a relatively blunt leading edge which, in turn, should produce a high maximum lift coefficient.

From this outline of the desired section characteristics, the pressure distributions at points A and B (sketch 1) can be deduced. The pressure distribution at point A (cruise) should probably look something like this:

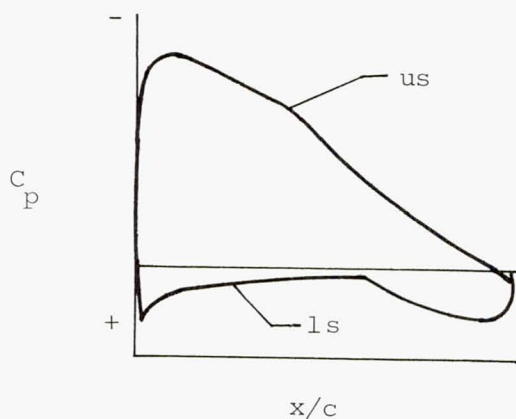


Sketch 2

A favorable pressure gradient on the upper surface is desirable up to the maximum extent allowed by the constraint of $(x/c)_{us} \leq 0.30$. Aft of $0.30c$ on the upper surface, a short region of slightly adverse pressure gradient is desirable to promote the efficient transition from laminar to turbulent flow (ref. 12). Thus, the initial slope of the pressure recovery is relatively shallow. This short region is followed by a steeper, concave pressure recovery. The concave pressure recovery produces lower drag and has less tendency to separate than the corresponding linear or convex pressure recovery (ref. 12). The proposed pressure recovery, although concave, does not approach the extreme shape of a Stratford recovery (ref. 13). The Stratford recovery is well suited for point designs but is not appropriate for an airfoil which must operate over a range of lift coefficients and Reynolds numbers (ref. 14).

Because no constraints were placed on the extent of the favorable pressure gradient on the lower surface, the pressure distribution along that surface is relatively arbitrary, except that it must satisfy the objectives of low drag at cruise and high maximum lift. The low cruise-drag objective can be met by incorporating a shallow, favorable pressure gradient over the forward portion of the lower surface. This is followed by a rather abrupt and steep concave pressure recovery, which results in a fair amount of aft camber. This camber, although limited by the pitching-moment constraint ($c_m \geq -0.10$), helps produce the high maximum lift coefficient.

At point B in sketch 1 ($c_l = 1.0$), the pressure distribution should look like this:



Sketch 3

No suction spike exists at the leading edge. Instead, a gently rounded peak occurs just aft of the leading edge. This feature is the result of incorporating increasingly favorable pressure gradients toward the leading edge. It is quite important in that it allows higher lift coefficients to be reached without significant separation.

EXECUTION

Given the pressure distributions for $c_l = 0.4$ and $c_l = 1.0$, the design of the airfoil is reduced to the inverse problem of transforming the pressure distributions into an airfoil shape. The method of reference 8 was used because it is capable of handling multipoint designs - designs where more than one angle of attack must be considered.

The inviscid pressure distributions computed by the method of reference 8 for $c_l = 0.4$ and $c_l = 1.0$ are shown in figures 1(a) and 1(b), respectively. For $c_l = 0.4$ (fig. 1(a)), the amount of pressure recovery achieved on the upper surface is relatively small. This feature contributes to achieving a high maximum lift coefficient. The pressure distribution along the lower surface at $c_l = 0.4$ is slightly adverse which probably limits the low cruise-drag characteristics of this airfoil to Reynolds numbers below 4 to 6×10^6 . The position of the beginning of the pressure-recovery region on the lower surface ($x/c = 0.6$) was selected by trial and error with priority given to $c_{l,max}$ without violating the pitching-moment constraint or increasing the cruise drag significantly. For $c_l = 1.0$ (fig. 1(b)), the gently rounded peak in the pressure distribution along the upper surface is evident just aft of the leading edge. At this lift coefficient, separation should be expected somewhere along the very steep pressure gradient aft of $0.95c$ on the upper surface. This separation should have little effect on either the drag or the lift.

The resulting shape is shown in figure 2 and the coordinates are presented in table I. The designation, NLF(1)-0416, follows the form:

<u>Application</u>	<u>Airfoil number</u>		<u>$c_{l,design}$</u>	<u>t/c</u>
Natural Laminar Flow	(1)	-	0.4	0.16

For this airfoil, $c_{l,design}$ is defined as the cruise lift coefficient. It must be emphasized, however, that this in no way implies that this airfoil was designed at only one point, $c_{l,design}$; all of the objectives and constraints were considered.

The objectives and constraints are compared in the following table with the values calculated by the method of reference 8:

	<u>Objective/constraint</u>	<u>Calculated</u>
$c_{l,max}$ at $R = 3.0 \times 10^6$	≥ 1.76	1.64
c_d for $c_l = 0.4$ at $R = 4.0 \times 10^6$. .	similar to 6-series airfoils	0.0063
Extent of favorable gradient on upper surface at cruise c_l	$\leq 0.30c$	0.26c
t/c	≥ 0.12	0.16
$C_{m,c_l} = 0$	≥ -0.10	-0.11

The calculated maximum lift coefficient at $R = 3.0 \times 10^6$ is 1.64, which is below the objective of $c_{l,max} \geq 1.76$. The objective of drag similar to that of the NACA 6-series airfoils was achieved, and the constraints on the extent of the favorable pressure gradient on the upper surface at the cruise lift coefficient and on the airfoil thickness were satisfied. The constraint on the pitching-moment coefficient was violated.

EXPERIMENTAL PROCEDURE

WIND TUNNEL

The Langley Low-Turbulence Pressure Tunnel (LTPT) (ref. 9) is a closed-throat, single-return tunnel which can be operated at stagnation pressures from 3 to 1000 kPa (0.03 to 10 atm). The minimum unit Reynolds number is approximately 3.9×10^4 per meter (1.2×10^4 per foot) at a Mach number of 0.05, whereas the maximum unit Reynolds number is approximately 4.9×10^7 per meter (1.5×10^7 per foot) at a Mach number of 0.23. The maximum, tunnel-empty,

test-section Mach number of 0.46 occurs at a stagnation pressure of about 100 kPa (1 atm).

The test section is 91.44 cm (36.00 in.) wide by 228.6 cm (90.00 in.) high. Hydraulically actuated circular plates provide positioning and attachment for the two-dimensional model. The plates, 101.6 cm (40.00 in.) in diameter, are flush with the tunnel sidewalls and rotate with the model. The model ends were mounted to rectangular model-attachment plates as shown in figure 3.

MODEL

The wind-tunnel model of the NLF(1)-0416 airfoil consisted of a metal spar surrounded by plastic filler with two thin layers of fiberglass forming the aerodynamic surface. The model had a chord of 60.902 cm (23.977 in.) and a span of 91.44 cm (36.00 in.). Upper- and lower-surface orifices were located 7.62 cm (3.00 in.) to one side of the midspan at the chord stations listed in table II. Spanwise orifices were located only in the upper surface in order to monitor the two-dimensionality of the flow at high angles of attack. The model surface was sanded with No. 600, dry silicon-carbide paper to insure an aerodynamically smooth finish. Accuracy of the model contour was generally within ± 0.08 mm (± 0.003 in.). After the tests of the design shape were completed, the sharp trailing edge was modified to a blunt trailing edge by bonding a wedge to the upper surface as shown in figure 4. This configuration was tested to determine if any aerodynamic penalties are incurred by this structurally advantageous concept.

WAKE RAKE

A fixed, wake rake (fig. 5) was cantilevered from the tunnel sidewall at the model midspan and 1.0 chord downstream from the trailing edge of the model. The wake rake employed 91 total-pressure tubes, 0.152 cm (0.060 in.) in diameter, and 5 static-pressure tubes, 0.318 cm (0.125 in.) in diameter. The total-pressure tubes were flattened to 0.102 cm (0.040 in.) for a length of 0.61 cm (0.24 in.) from the tips of the tubes. Each static-pressure tube had four flush orifices located 90° apart, 8 tube diameters from the tip of the tube in the measurement plane of the total-pressure tubes.

INSTRUMENTATION

Measurements of the static pressures on the model surfaces and of the wake-rake pressures were made by an automatic pressure-scanning system utilizing variable-capacitance precision transducers. Basic tunnel pressures were measured with precision quartz manometers. Geometric angle of attack was measured by a calibrated, digital, shaft encoder driven by a pinion gear and a rack attached to the circular plates. Data were obtained by a high-speed data-acquisition system and were recorded on magnetic tape.

TESTS AND METHODS

The model was tested at Reynolds numbers based on the airfoil chord from approximately 1.0×10^6 to 9.0×10^6 . The Mach number was varied from about 0.1 to 0.4. The model was tested smooth (transition free) and with transition fixed by roughness at 0.075c on both surfaces. The roughness was sized for each Reynolds number by the method of reference 15. The granular roughness was sparsely distributed along 3-mm (0.1-in.) wide strips applied to the model with lacquer.

For several test runs, the model upper surface was coated with oil to determine the location, as well as the nature, of the boundary-layer transition from laminar to turbulent flow (ref. 16). Transition was also located by connecting a microphone to the orifices on the model (ref. 17). This technique allows an observer to start at the leading edge and progress from orifice to orifice toward the trailing edge. The beginning of the turbulent boundary layer is detected as an increase in noise level over that for the laminar boundary layer, which is essentially silent. No measurements were obtained for $R > 4.0 \times 10^6$, because the ambient noise level in the tunnel became too high.

The static-pressure measurements at the model surface were reduced to standard-pressure coefficients and numerically integrated to obtain section normal-force and chord-force coefficients and section pitching-moment coefficients about the quarter-chord point. Section profile-drag coefficients were computed from the wake-rake total and static pressures by the method of reference 10.

Standard, low-speed, wind-tunnel boundary corrections (ref. 18), a maximum of approximately 3 percent of the measured section coefficients, have been applied to the data. These corrections decrease the maximum lift coefficient and increase the pitching-moment coefficient. The wake-rake total-pressure-tube displacement correction (ref. 10), a maximum increase of approximately 2 percent of the measured profile-drag coefficients, has not been taken into account in order that the data be directly comparable to previously published airfoil data.

DISCUSSION OF RESULTS

EXPERIMENTAL RESULTS

Pressure Distributions

The pressure distributions for various angles of attack at a Reynolds number of 4.0×10^6 and a Mach number of 0.10 are shown in figure 6. At $\alpha = -16.08^\circ$ (fig. 6(a)), the entire lower surface is separated. As the angle of attack is increased from -15.23° which corresponds to $c_{l,\min}$ (fig. 6(b)), the leading-edge peak decreases in magnitude until it has disappeared at $\alpha = -2.04^\circ$ (fig. 6(o)). The lift coefficient at this angle of attack corresponds roughly to the lower limit of the low-drag range. As the angle of attack is increased further, the position of minimum pressure on the upper surface moves slowly forward (figs. 6(o) to 6(bb)). This feature was one of the design goals discussed

in "Philosophy" and represents an improvement over the sudden jump of $C_{p,min}$, typical of the NACA 6-series airfoils. At $\alpha = 11.19^\circ$ (fig. 6(bb)), the minimum pressure on the upper surface occurs at $x/c = 0.0$, thus forming a leading-edge peak. As the angle of attack is increased even further, turbulent trailing-edge separation occurs on the upper surface (figs. 6(ee) and 6(ff)). The leading-edge peak does not completely collapse, even beyond $c_{l,max}$, indicating that leading-edge separation does not occur up through the maximum angle of attack tested (figs. 6(ff) to 6(hh)).

Transition Location

For a Reynolds number of 2.0×10^6 , the mechanism of the boundary-layer transition from laminar to turbulent flow on the upper surface, at an angle of attack of 0.0° , was a laminar separation bubble which extends from laminar separation to turbulent reattachment as shown in figure 7(a). This bubble was caused by the slight adverse pressure gradient immediately downstream of the minimum pressure on the upper surface (fig. 6(q)). This gradient was a design goal as discussed in "Philosophy." As the angle of attack is increased, the laminar separation bubble disappears and the transition location on the upper surface moves slowly forward (figs. 7(b) to 7(e)). When the Reynolds number is increased to 4.0×10^6 , no laminar separation bubble occurs on the upper surface (fig. 8).

The variation of transition location with lift coefficient, as determined by microphone measurements, is shown in figure 9. Because the microphone is connected to individual orifices on the model, the transition location can only be determined as lying somewhere between two adjacent orifices. In figure 9, the open symbols represent orifice locations at which the flow is laminar and the solid symbols represent orifice locations at which the flow is turbulent. In fairing the curves, a generally linear variation of transition location with lift coefficient was assumed. Although not shown, the transition locations were unaffected by the blunt trailing edge. The effect of Reynolds number on transition location is shown in figure 10.

Section Characteristics

Reynolds number effects.- The section characteristics at a Mach number of 0.10 are shown in figure 11. The effects of Reynolds number on the section characteristics are summarized in figure 12. The angle of attack for zero lift coefficient, approximately -3.8° , was unaffected by Reynolds number. The lift-curve slope increased slightly with increasing Reynolds number, whereas the pitching-moment coefficient was relatively insensitive to Reynolds number variation. The pitching-moment coefficient for $c_l = 0$ was approximately -0.09 , which satisfies the design constraint of $c_m \geq -0.10$ for $c_l = 0$. (See "Objectives and Constraints.")

The variation of maximum lift coefficient with Reynolds number is shown in figure 13. The maximum lift coefficient at $R = 3.0 \times 10^6$ was approximately 1.69, which is somewhat below the design objective of $c_{l,max} \geq 1.76$. (See "Objectives and Constraints.")

The variation of minimum drag coefficient with Reynolds number is shown in figure 14. It should be noted that, although the minimum drag coefficient decreases steadily with increasing Reynolds number, it occurs at increasingly higher lift coefficients. (See fig. 12.) This result can be traced to the forward movement of the transition location on the lower surface. As shown in figure 10, the lift coefficient at which this forward movement occurs increases with increasing Reynolds number.

Mach number effects.- The section characteristics for a Reynolds number of 6.0×10^6 are shown in figure 15. The effects of Mach number on the section characteristics are summarized in figure 16. The angle of attack for zero lift coefficient was unaffected by Mach number. The lift-curve slope increased moderately with increasing Mach number, whereas the pitching-moment coefficient decreased slightly with increasing Mach number. The maximum lift coefficient and the minimum drag coefficient were unaffected by Mach number as shown in figures 17 and 18, respectively.

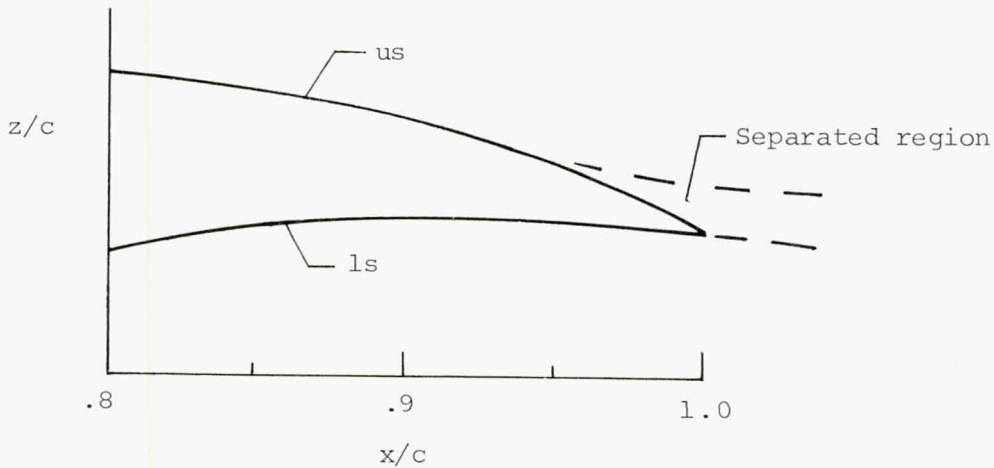
Effect of roughness.- The effect of roughness on the section characteristics for various Reynolds numbers is shown in figure 19. The angle of attack for zero lift coefficient and the pitching-moment coefficients increased with transition fixed, whereas the lift-curve slope decreased. All of these results are a consequence of the displacement effect which decambers the airfoil slightly. This effect is a result of the boundary-layer displacement thickness which is greater for the transition-fixed condition than for the transition-free condition. An increase in Reynolds number decreases the displacement thickness and, therefore, the displacement effect.

Of more importance, however, is the effect of roughness on the maximum lift coefficient and the drag coefficients. The addition of roughness had no significant effect on $c_{l,max}$ for any of the Reynolds numbers (fig. 20). Thus, one of the most important design requirements has been achieved. (See "Objectives and Constraints.") The minimum drag coefficients were, of course, adversely affected by the roughness (fig. 21).

The effect of roughness on the section characteristics at various Mach numbers is shown in figure 22. The effect of roughness on maximum lift coefficient and minimum drag coefficient at various Mach numbers is shown in figures 23 and 24, respectively. All of the previously mentioned effects are again apparent except that the displacement effect is not altered by Mach number.

Effect of blunt trailing edge.- The effect of the blunt trailing edge (fig. 4) on the section characteristics for various Reynolds numbers is shown with transition free in figure 25 and with transition fixed in figure 26. The angle of attack for zero lift coefficient and the pitching-moment coefficients increased with the addition of the blunt trailing edge, whereas the minimum lift coefficient decreased. All of these results are a consequence of the reduction in camber near the trailing edge which resulted from the addition of the wedge to the upper surface to form the blunt trailing edge. (See fig. 4.) It is surprising, however, that the maximum lift coefficient was unaffected (fig. 27). This is probably the result of a small separation on the upper surface of the

sharp trailing edge at the higher lift coefficients, as shown in the following sketch:



Sketch 4

The wedge used to form the blunt trailing edge merely replaces the separated region and, therefore, no decambering effect occurs at the higher lift coefficients.

The minimum drag coefficients increased slightly with the addition of the blunt trailing edge (fig. 28). These increased drag coefficients imply that the trailing-edge thickness is too large, resulting in a drag penalty due to base drag. This implication is substantiated by the increase in the drag penalty with increasing Reynolds number (thinner boundary layers). (See fig. 25.) Further, the drag penalty disappears with transition fixed for a Reynolds number of 2.0×10^6 (thicker boundary layers). (See fig. 26.)

COMPARISON OF THEORETICAL AND EXPERIMENTAL RESULTS

Pressure Distributions

The comparison of theoretical and experimental pressure distributions is shown in figure 29. The pressure distributions predicted by the method of reference 8 are inviscid (potential flow) and incompressible. The experimental pressure distributions were obtained for a Reynolds number of 4.0×10^6 and a Mach number of 0.10 and, thus, contain the same data presented in figures 6(q), 6(v), and 6(ee). At $\alpha = 0.01^\circ$ (fig. 29(a)), the theoretical predictions and the experimental data are in close agreement. Although the values of the pressure coefficients do not match exactly, the pressure gradients agree well. At $\alpha = 5.09^\circ$ (fig. 29(b)), the decambering viscous effects have become more apparent and the disparities include small differences in the pressure gradients as well as larger differences in the values of the pressure coefficients. At $\alpha = 14.23^\circ$ (fig. 29(c)), which corresponds to the experimental maximum lift

coefficient, the agreement is poor primarily because of the upper-surface, trailing-edge separation which is not modeled in the method of reference 8.

Transition Location

The comparison of theoretical and experimental transition locations is shown in figure 30. The method of reference 8 consistently predicts transition upstream of the locations measured in the wind tunnel. This result is obtained because the theoretical method predicts transition immediately following laminar separation; whereas, transition can be confirmed in the wind tunnel, only by the occurrence of attached turbulent flow. This deduction is substantiated by the improved agreement between theory and experiment for conditions which result in shorter laminar separation bubbles (higher lift coefficients for the upper surface and lower lift coefficients for the lower surface and/or higher Reynolds numbers).

Section Characteristics

The comparison of theoretical and experimental section characteristics with transition free is shown in figure 31. The magnitudes of both the angle of attack for zero lift coefficient and the pitching-moment coefficients are over-predicted by the method of reference 8. These results are obtained because the theoretical method does not contain a boundary-layer-displacement iteration. The agreement between theoretical and experimental lift-curve slopes and maximum lift coefficients is quite good. The calculated maximum lift coefficients are increasingly conservative (low) with increasing Reynolds number. The agreement between theoretical and experimental drag coefficients is very good. Again, the predicted values become more and more conservative (high) with increasing Reynolds number.

The comparison of theoretical and experimental section characteristics with transition fixed is shown in figure 32. The results are the same as for the transition-free condition except that the small differences between the predicted and measured drag coefficients do not increase with increasing Reynolds number.

COMPARISONS WITH OTHER AIRFOILS

Laminar-Flow Airfoils

Shown in figure 33 is a comparison of the maximum lift coefficients at various Reynolds numbers for the NLF(1)-0416 airfoil and for two NACA 6-series airfoils of similar design lift coefficient and thickness, the 632-415 and 632-615. The significant increases in maximum lift coefficients over those for the 6-series airfoils show that the first design objective, $c_{l,max} \geq 1.76$, was essentially achieved. The drag coefficients for these three airfoils at lift coefficients of 0.4 and 1.0 are compared in figures 34 and 35, respectively. For $c_l = 0.4$ (fig. 34), the 6-series airfoils exhibit somewhat lower drag coefficients. Some of the difference in drag levels can be attributed to the fact that the 6-series airfoils are thinner ($t/c = 0.15$) than the NLF(1)-0416

airfoil ($t/c = 0.16$). For $c_l = 1.0$ (fig. 35), the NLF(1)-0416 airfoil exhibits lower drag coefficients because this lift coefficient is outside the low-drag range of both of these 6-series airfoils.

Turbulent-Flow Airfoils

The comparison of the maximum lift coefficients for various Reynolds numbers for the NLF(1)-0416, LS(1)-0417 (formerly, GA(W)-1), and NACA 23015 and 4415 airfoils is shown in figure 36. The maximum lift coefficients for the NLF(1)-0416 airfoil with transition free, as well as fixed, are comparable to those for the LS(1)-0417 airfoil. These maximum lift coefficients are substantially higher than those for the NACA 23015 and 4415 airfoils. The drag coefficients for these four airfoils at lift coefficients of 0.4 and 1.0 are compared in figures 37 and 38, respectively. For $c_l = 0.4$ (fig. 37), the NLF(1)-0416 airfoil exhibits a significantly lower drag coefficient with transition free at the cruise Reynolds number of 4.0×10^6 . With transition fixed, the NLF(1)-0416 airfoil exhibits lower drag coefficients than those for the LS(1)-0417 airfoil. Most, if not all, of the difference in drag levels can be attributed to the difference in airfoil thickness, however. For $c_l = 1.0$ (fig. 38), the NLF(1)-0416 airfoil exhibits lower drag coefficients with transition free. With transition fixed, the NLF(1)-0416 airfoil exhibits significantly lower drag coefficients than those for the LS(1)-0417 airfoil. Little of the difference in drag levels is associated with the difference in airfoil thickness, however. In fact, a comparison between the NLF(1)-0416 and LS(1)-0413 (formerly, GA(W)-2) airfoils (not shown) indicates that, at this lift coefficient with transition fixed, the NLF(1)-0416 airfoil exhibits the same drag coefficients as the much thinner LS(1)-0413 airfoil ($t/c = 0.13$).

CONCLUDING REMARKS

A new natural-laminar-flow airfoil for general aviation applications, the NLF(1)-0416, has been designed and analyzed theoretically and verified experimentally in the Langley Low-Turbulence Pressure Tunnel. The basic objective of combining the high maximum lift of the NASA low-speed airfoils with the low cruise drag of the NACA 6-series airfoils has been achieved. The safety requirement that the maximum lift coefficient not be significantly affected with transition fixed near the leading edge has also been met.

Comparisons of the theoretical and experimental results show excellent agreement. Comparisons with other airfoils, both laminar-flow and turbulent-flow, confirm the achievement of the basic objective.

The most important result is that the new natural-laminar-flow airfoil, even with transition fixed near the leading edge, achieves the same maximum lift coefficients as the NASA low-speed airfoils. At the same time, the new airfoil, with transition fixed, exhibits no higher cruise drag and lower climb drag coefficients than comparable turbulent-flow airfoils. Thus, if the new airfoil is employed in an aircraft design and laminar flow is not achieved, nothing is lost relative to the NASA low-speed airfoils. If laminar flow is achieved, a substantial profile-drag reduction results.

Finally, this airfoil demonstrates the unique and powerful capabilities of the theoretical method to design and analyze multipoint designs.

Langley Research Center
National Aeronautics and Space Administration
Hampton, VA 23665
April 24, 1981

REFERENCES

1. McGhee, Robert J.; Beasley, William D.; and Whitcomb, Richard T.: NASA Low- and Medium-Speed Airfoil Development. NASA TM-78709, 1979.
2. Jacobs, Eastman N.: Preliminary Report on Laminar-Flow Airfoils and New Methods Adopted for Airfoil and Boundary-Layer Investigations. NACA WR L-345, 1939 (formerly, NACA ACR).
3. Abbott, Ira H.; Von Doenhoff, Albert E.; and Stivers, Louis S., Jr.: Summary of Airfoil Data. NACA Rep. 824, 1945. (Supersedes NACA WR L-560.)
4. Payne, Henry E.: Laminar Flow Rethink - Using Composite Structure. [Preprint] 760473, Soc. Automot. Eng., Apr. 1976.
5. Alther, G. A.: A Significant Role for Composites in Energy-Efficient Aircraft. Technical Sessions of the Thirty-Sixth Annual Conference - Reinforced Plastics/Composites Institute, Soc. Plast. Ind., Inc., Feb. 1981, Sess. 12-D, pg. 1 - Sess. 12-D, pg. 4.
6. Eppler, R. (Francesca Neffgen, transl.): Laminar Airfoils for Reynolds Numbers Greater Than 4×10^6 . B-819-35, Apr. 1969. (Available from NTIS as N69-28178.)
7. Eppler, Richard: Some New Airfoils. Science and Technology of Low Speed and Motorless Flight, NASA CP-2085, Part I, 1979, pp. 131-153.
8. Eppler, Richard; and Somers, Dan M.: A Computer Program for the Design and Analysis of Low-Speed Airfoils. NASA TM-80210, 1980.
9. Von Doenhoff, Albert E.; and Abbott, Frank T., Jr.: The Langley Two-Dimensional Low-Turbulence Pressure Tunnel. NACA TN 1283, 1947.
10. Pankhurst, R. C.; and Holder, D. W.: Wind-Tunnel Technique. Sir Isaac Pitman & Sons, Ltd. (London), 1965.
11. McGhee, Robert J.; Beasley, William D.; and Somers, Dan M.: Low-Speed Aerodynamic Characteristics of a 13-Percent-Thick Airfoil Section Designed for General Aviation Applications. NASA TM X-72697, 1975.
12. Wortmann, F. X.: Experimental Investigations on New Laminar Profiles for Gliders and Helicopters. TIL/T.4906, British Minist. Aviat., Mar. 1960.
13. Stratford, B. S.: The Prediction of Separation of the Turbulent Boundary Layer. J. Fluid Mech., vol. 5, pt. 1, Jan. 1959, pp. 1-16.
14. Eppler, Richard; and Somers, Dan M.: Low Speed Airfoil Design and Analysis. Advanced Technology Airfoil Research - Volume I, NASA CP-2045, Part 1, 1979, pp. 73-99.

15. Braslow, Albert L.; and Knox, Eugene C.: Simplified Method for Determination of Critical Height of Distributed Roughness Particles for Boundary-Layer Transition at Mach Numbers From 0 to 5. NACA TN 4363, 1958.
16. Loving, Donald L.; and Katzoff, S.: The Fluorescent-Oil Film Method and Other Techniques for Boundary-Layer Flow Visualization. NASA MEMO 3-17-59L, 1959.
17. Hood, William R.; and Somers, Dan M.: Detection of Boundary-Layer Transitions in Wind Tunnels. NASA Tech Brief 12261, 1978.
18. Allen, H. Julian; and Vincenti, Walter G.: Wall Interference in a Two-Dimensional-Flow Wind Tunnel, With Consideration of the Effect of Compressibility. NACA Rep. 782, 1944. (Supersedes NACA WR A-63.)

TABLE I.- NLF(1)-0416 AIRFOIL COORDINATES

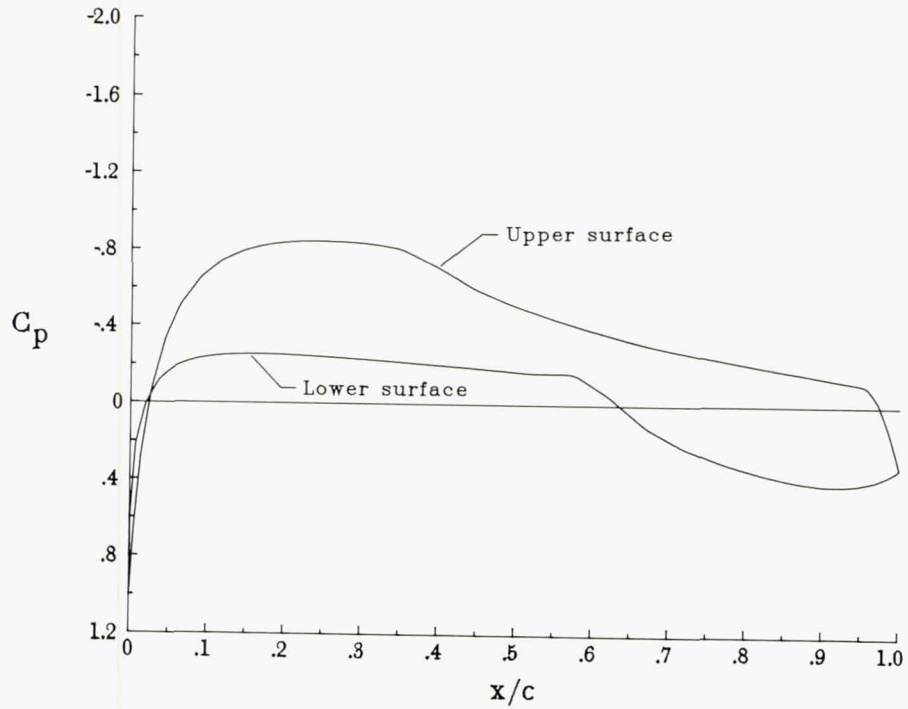
[c = 60.902 cm (23.977 in.)]

UPPER SURFACE		LOWER SURFACE	
X/C	Z/C	X/C	Z/C
.00049	.00403	.00073	-.00439
.00509	.01446	.00709	-.01154
.01393	.02573	.01956	-.01883
.02687	.03729	.03708	-.02594
.04383	.04870	.05933	-.03254
.06471	.05964	.08609	-.03847
.08936	.06984	.11708	-.04361
.11761	.07904	.15200	-.04787
.14925	.08707	.19050	-.05121
.18404	.09374	.23218	-.05357
.22169	.09892	.27659	-.05494
.26187	.10247	.32326	-.05529
.30422	.10425	.37167	-.05462
.34839	.10405	.42127	-.05291
.39438	.10162	.47150	-.05009
.44227	.09729	.52175	-.04614
.49172	.09166	.57122	-.04063
.54204	.08515	.62019	-.03250
.59256	.07801	.67014	-.02231
.64262	.07047	.72107	-.01221
.69155	.06272	.77156	-.00364
.73872	.05493	.82012	.00278
.78350	.04724	.86536	.00667
.82530	.03977	.90576	.00792
.86357	.03265	.93978	.00696
.89779	.02594	.96638	.00478
.92749	.01974	.98520	.00242
.95224	.01400	.99633	.00065
.97197	.00862	1.00000	.00000
.98686	.00398		
.99656	.00098		
1.00000	.00000		

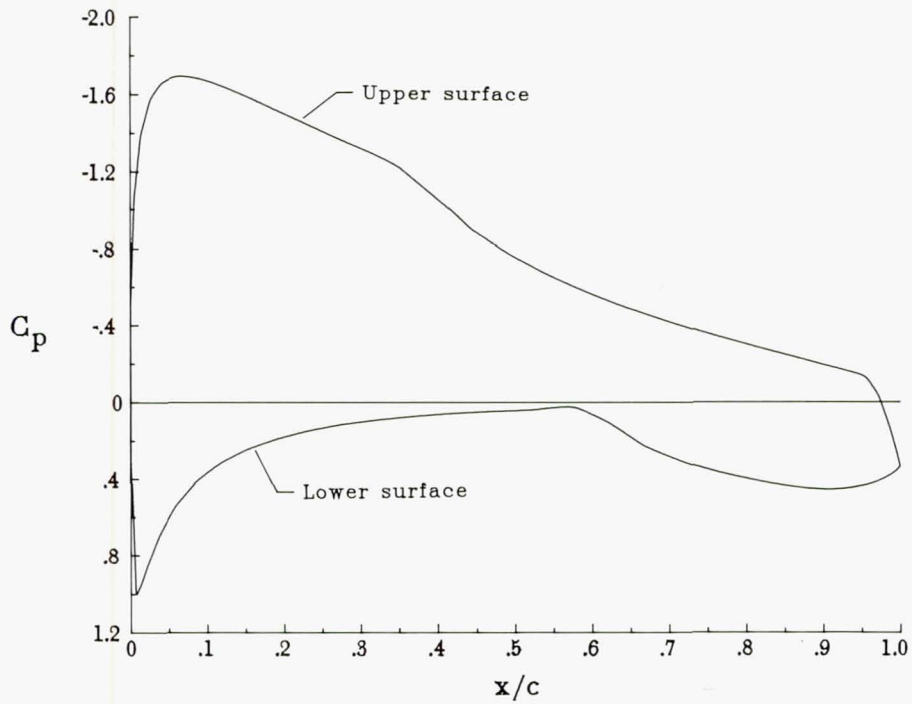
TABLE II.- MODEL ORIFICE LOCATIONS

[c = 60.902 cm (23.977 in.)]

UPPER SURFACE		LOWER SURFACE	
X/C	Z/C	X/C	Z/C
.000213	.000859	.005238	-.010039
.005943	.015289	.010714	-.014013
.010810	.022021	.015148	-.016712
.015611	.027234	.020378	-.019343
.020386	.031763	.025253	-.021479
.025562	.036101	.030470	-.023606
.030900	.040180	.040205	-.027092
.040805	.046765	.050131	-.030191
.049943	.052062	.060298	-.032931
.060449	.057546	.075229	-.036434
.075659	.064419	.100803	-.041272
.100465	.073778	.150867	-.047912
.150788	.087445	.200622	-.052037
.200643	.096307	.250769	-.054397
.250853	.101771	.300666	-.055373
.300862	.104269	.350768	-.055156
.350976	.104081	.400998	-.053872
.401194	.101229	.451004	-.051524
.451321	.096478	.500884	-.048074
.501385	.090685	.551094	-.043320
.551373	.084104	.601012	-.036197
.601583	.076935	.651163	-.026500
.651438	.069357	.701223	-.016240
.701515	.061358	.750277	-.007240
.751383	.053054	.800637	.000279
.800888	.044425	.850238	.005489
.850063	.035458	.901883	.007849
.900636	.025678	.951037	.006273
.952055	.014247	.976816	.003687
.976540	.007570		



(a) $c_l = 0.4$.



(b) $c_l = 1.0$.

Figure 1.- Inviscid pressure distributions.

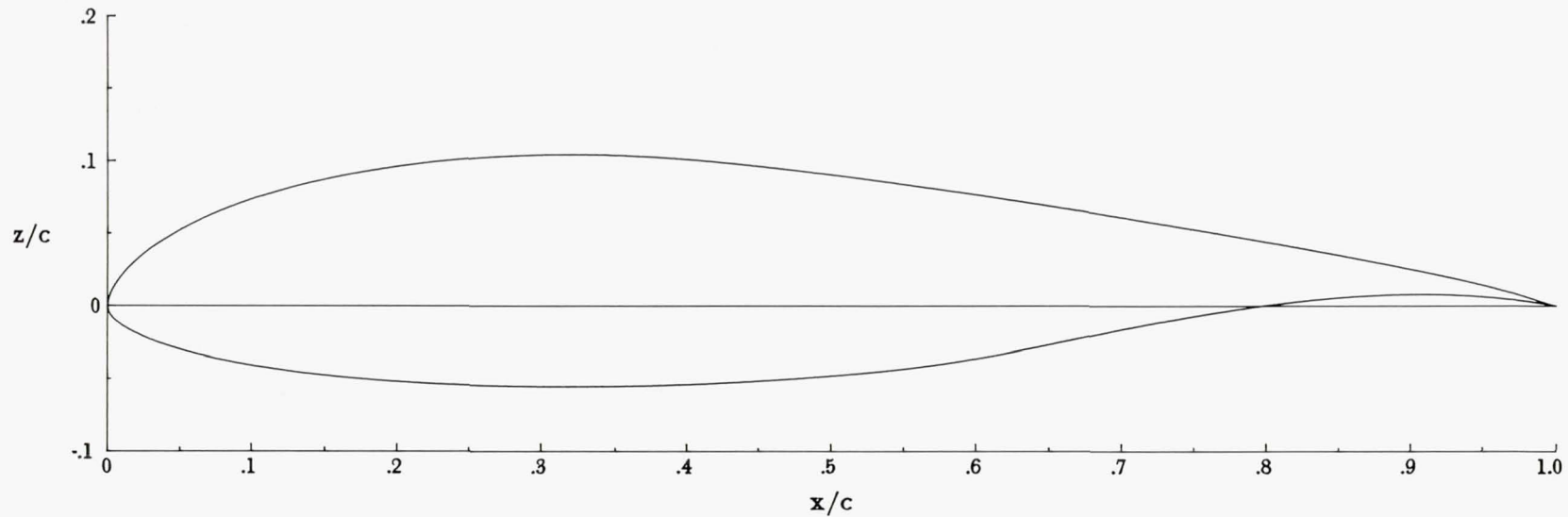


Figure 2.- NLF(1)-0416 airfoil shape.

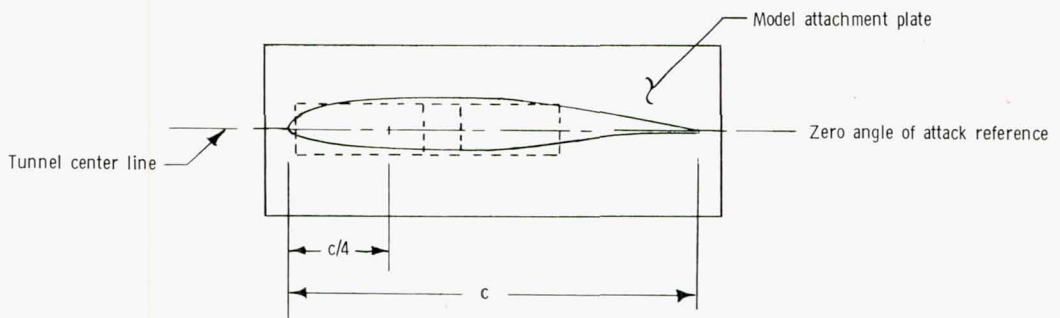
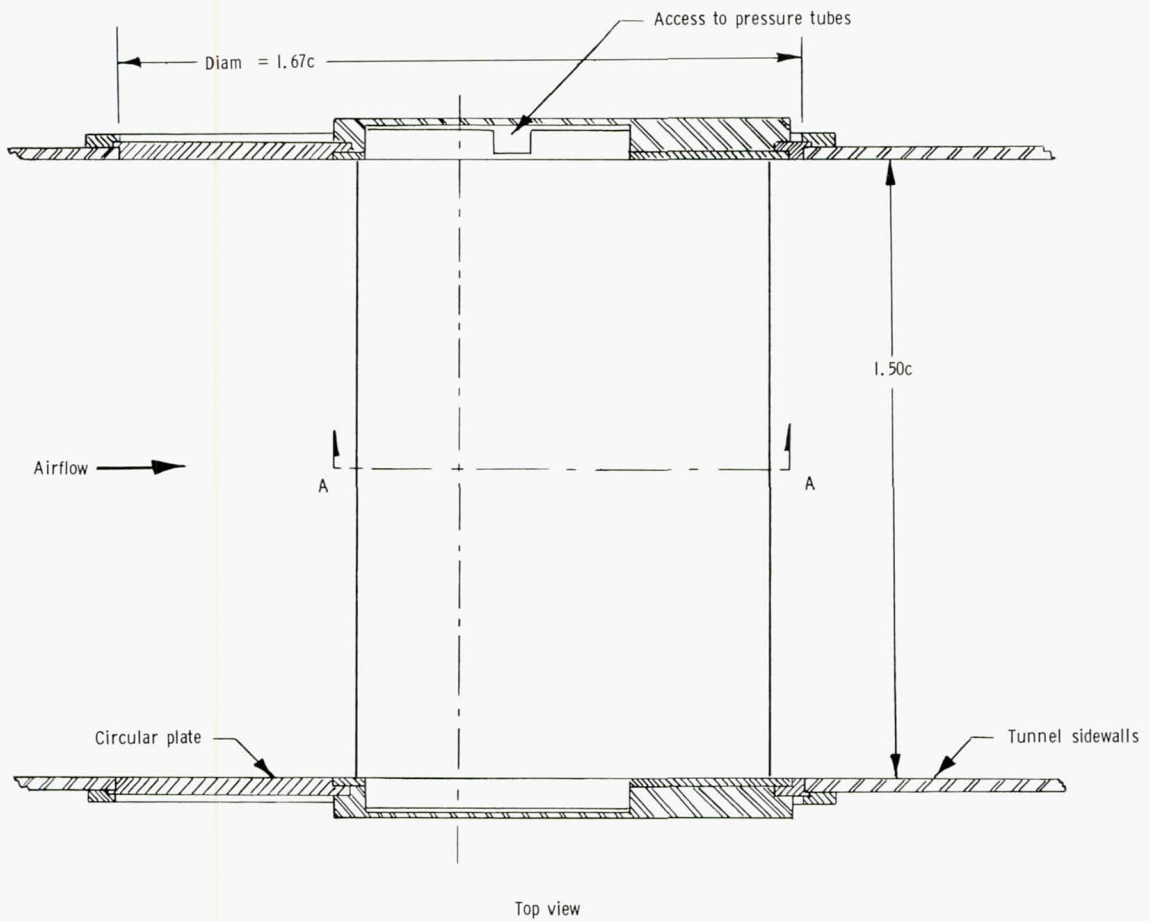


Figure 3.- Typical airfoil model mounted in wind tunnel. All dimensions are in terms of model chord; $c = 61.0 \text{ cm (24.0 in.)}$.

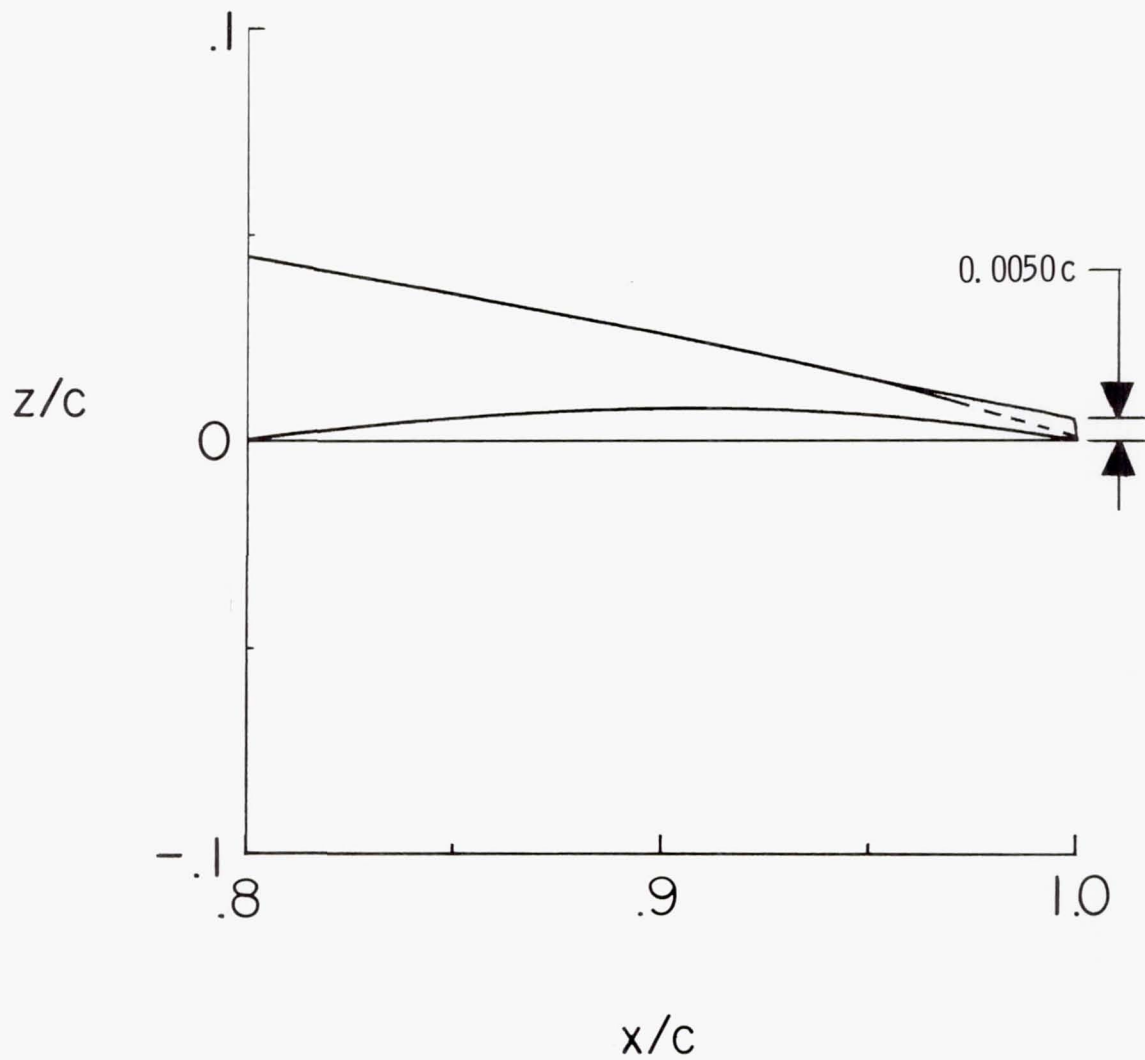


Figure 4.- Blunt trailing edge; $c = 60.902$ cm (23.977 in.).

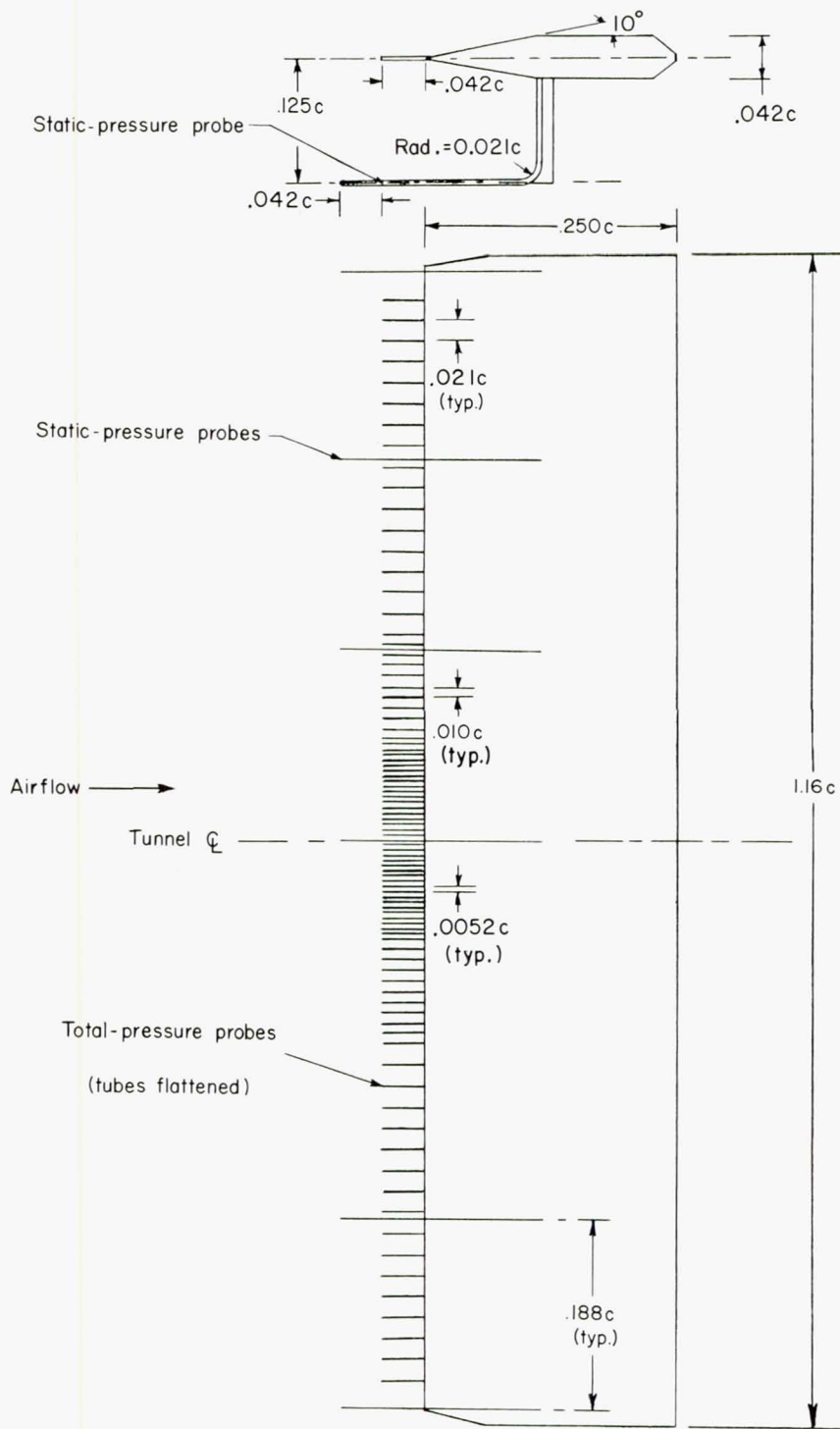
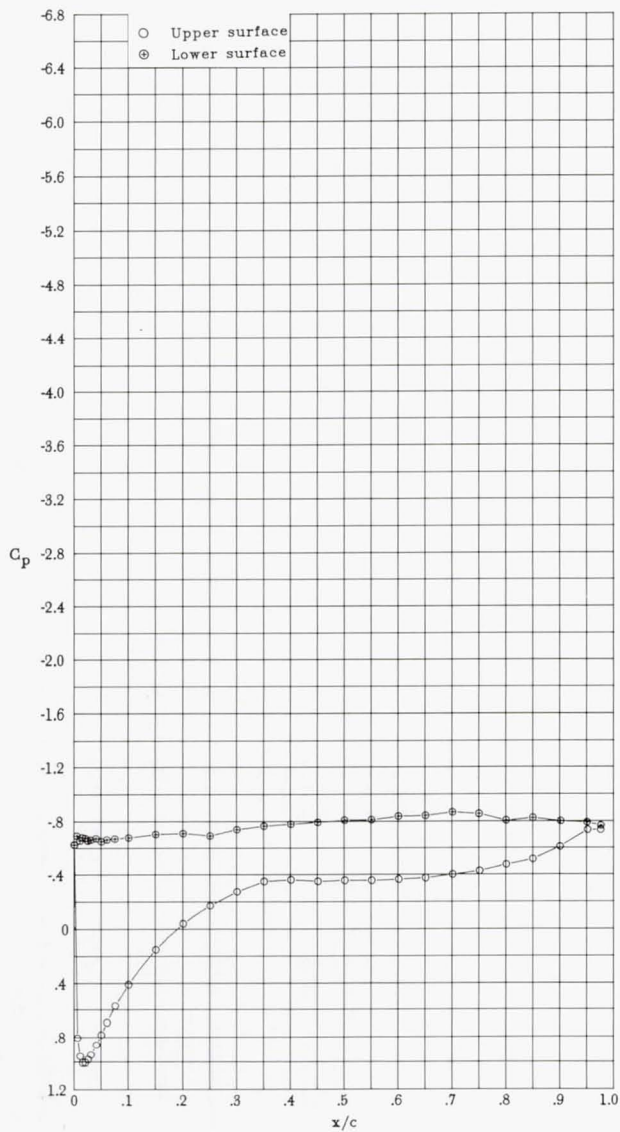
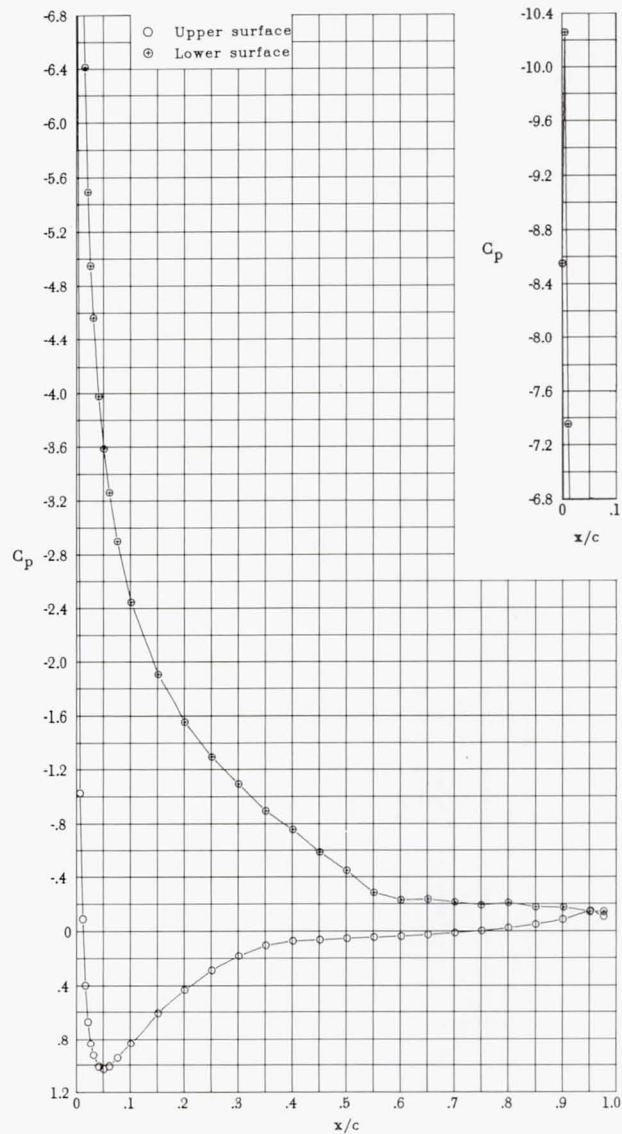


Figure 5.- Wake rake. All dimensions are in terms of model chord; $c = 61.0$ cm (24.0 in.).

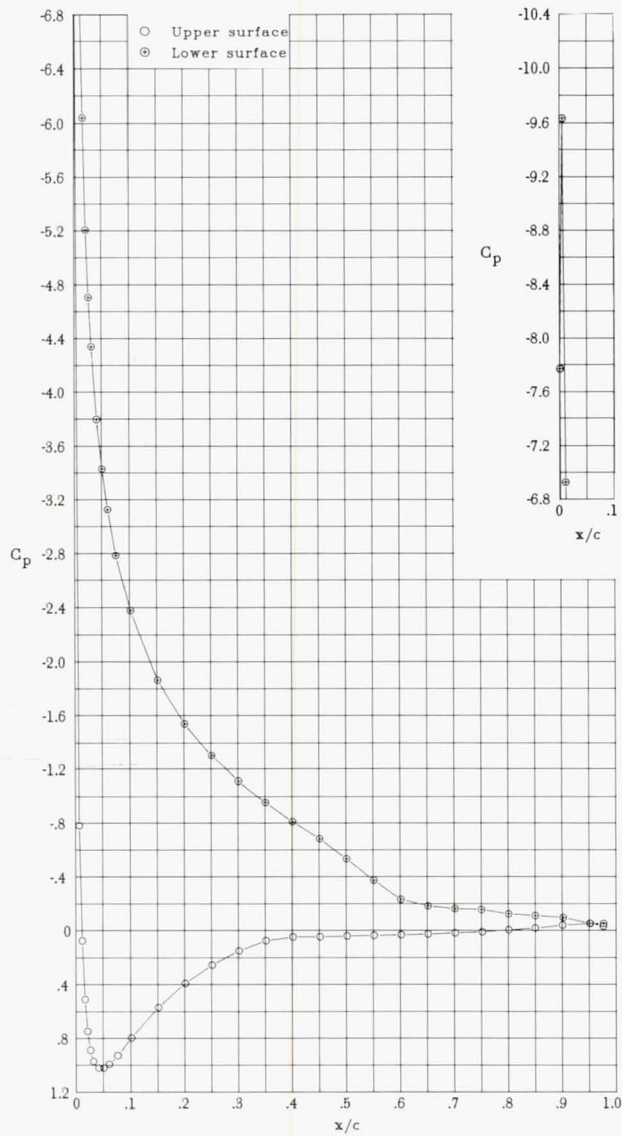


(a) $\alpha = -16.08^\circ$; $c_l = -0.456$; $c_d = 0.2427$; $c_m = 0.052$.

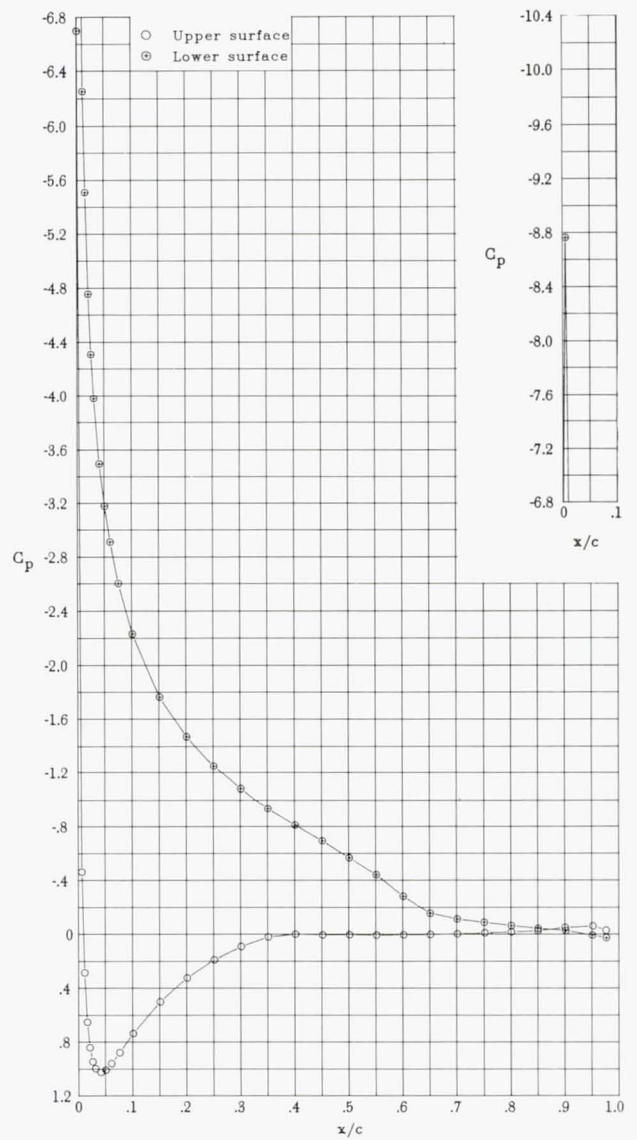


(b) $\alpha = -15.23^\circ$; $c_l = -1.161$; $c_d = 0.0516$; $c_m = -0.061$.

Figure 6.- Pressure distributions for $R = 4.0 \times 10^6$ and $M = 0.10$.

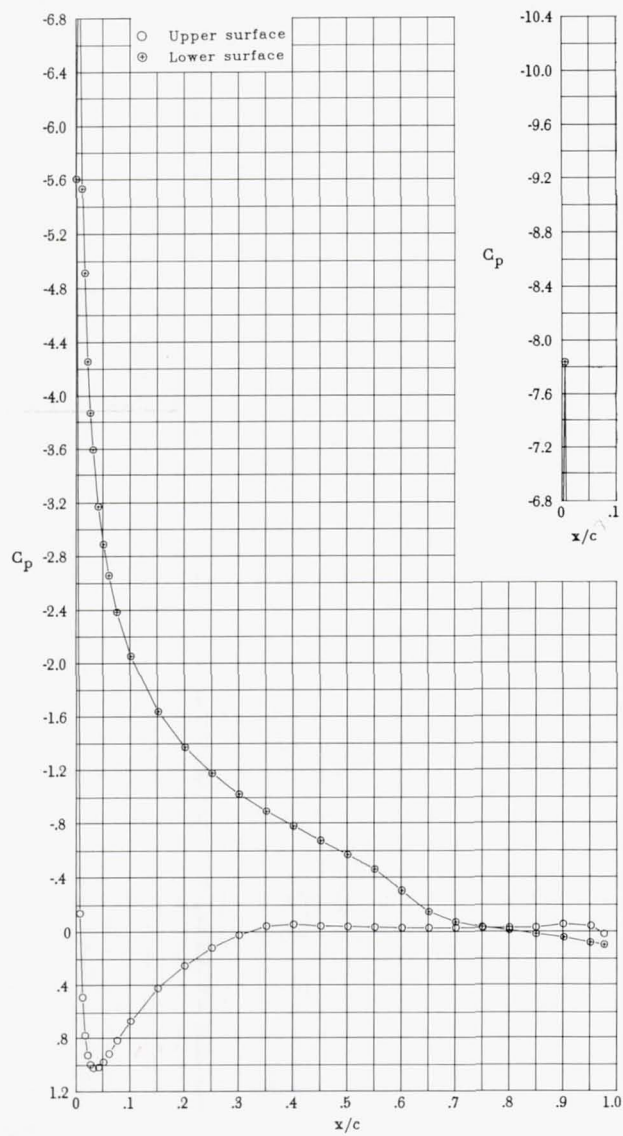


(c) $\alpha = -14.22^\circ$; $c_l = -1.134$; $c_d = 0.0367$; $c_m = -0.060$.

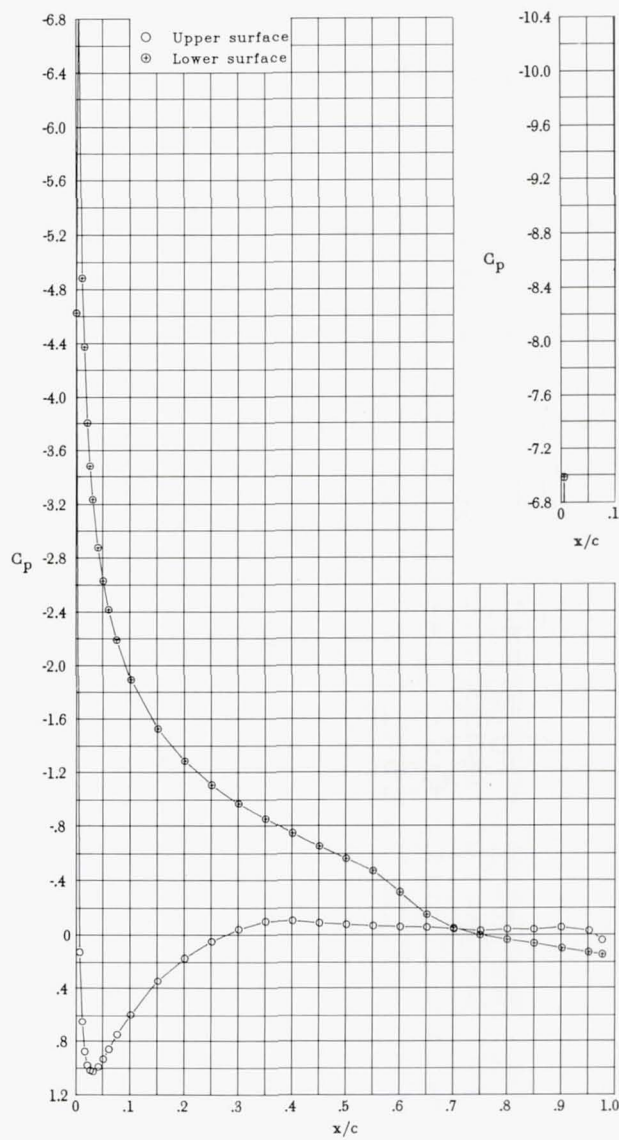


(d) $\alpha = -13.21^\circ$; $c_l = -1.041$; $c_d = 0.0259$; $c_m = -0.068$.

Figure 6.- Continued.

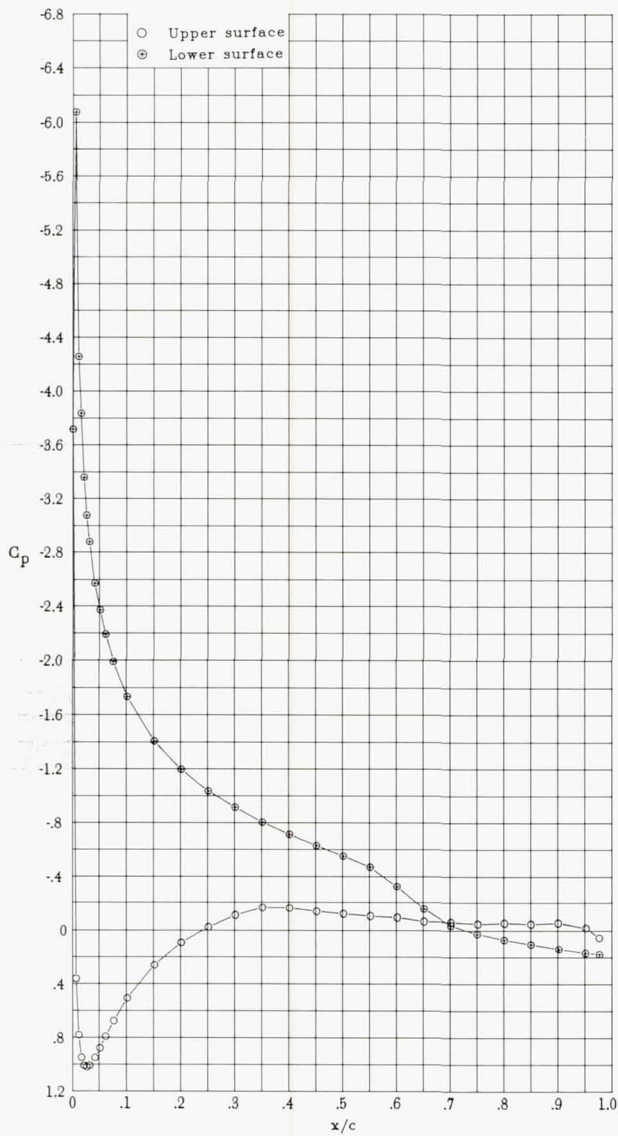


(e) $\alpha = -12.21^\circ$; $c_l = -0.930$; $c_d = 0.0193$; $c_m = -0.074$.

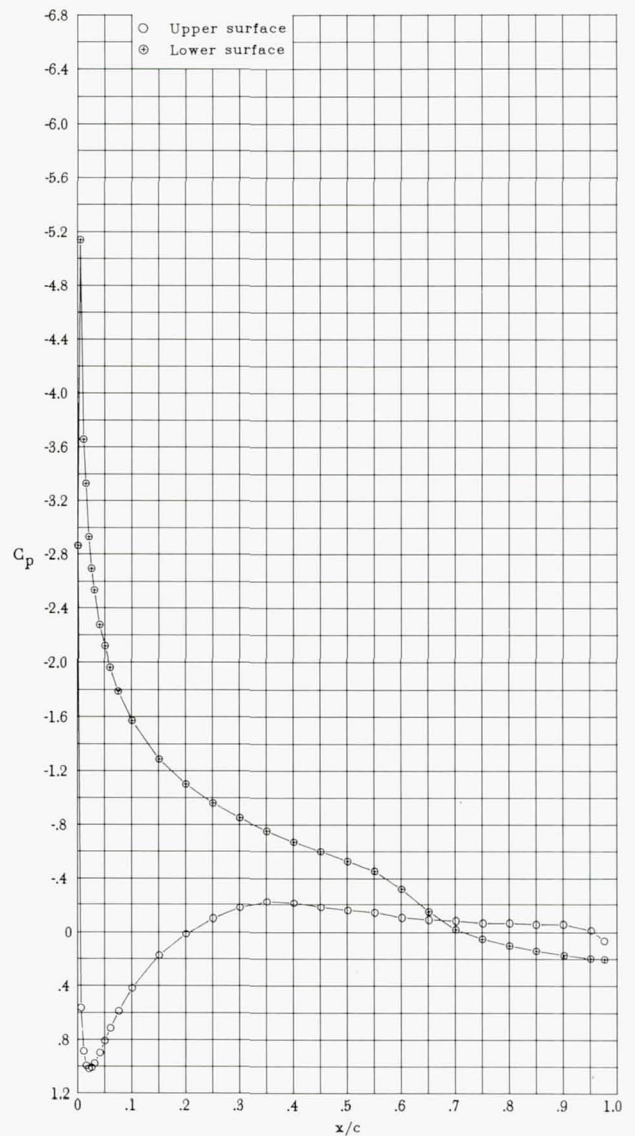


(f) $\alpha = -11.20^\circ$; $c_l = -0.828$; $c_d = 0.0152$; $c_m = -0.078$.

Figure 6.- Continued.

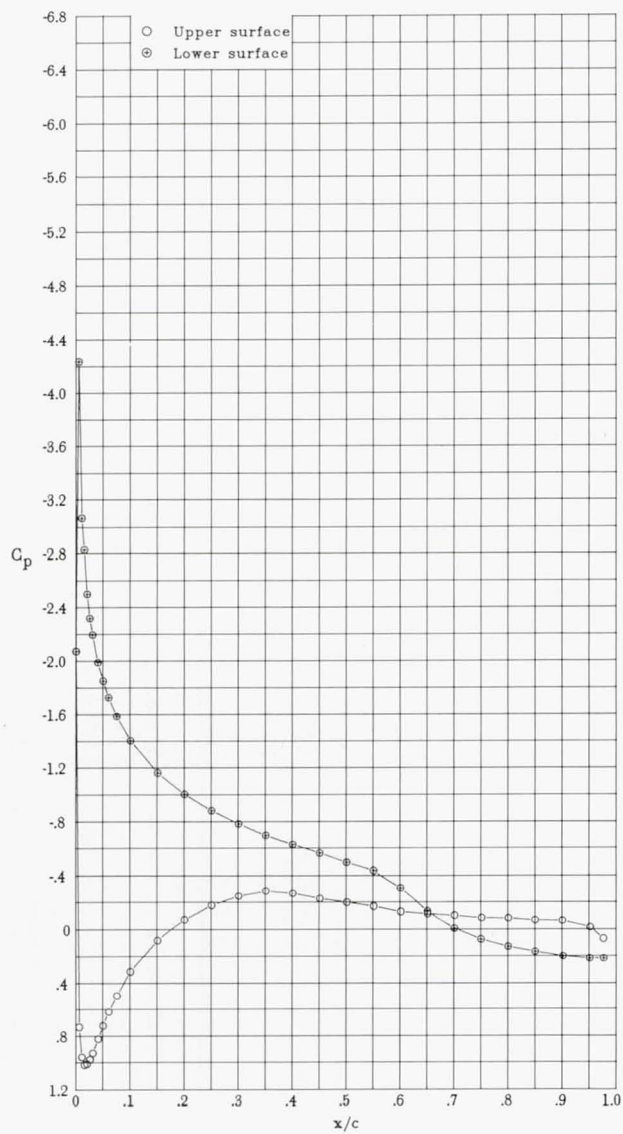


(g) $\alpha = -10.17^\circ$; $c_l = -0.725$; $c_d = 0.0138$; $c_m = -0.079$.

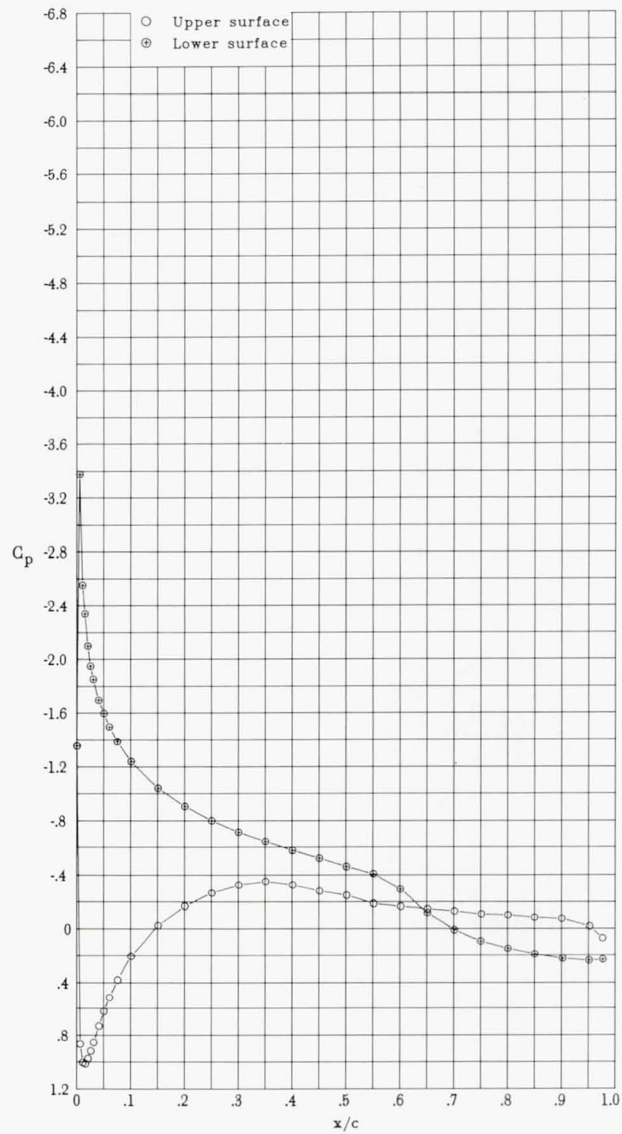


(h) $\alpha = -9.16^\circ$; $c_l = -0.617$; $c_d = 0.0124$; $c_m = -0.082$.

Figure 6.- Continued.

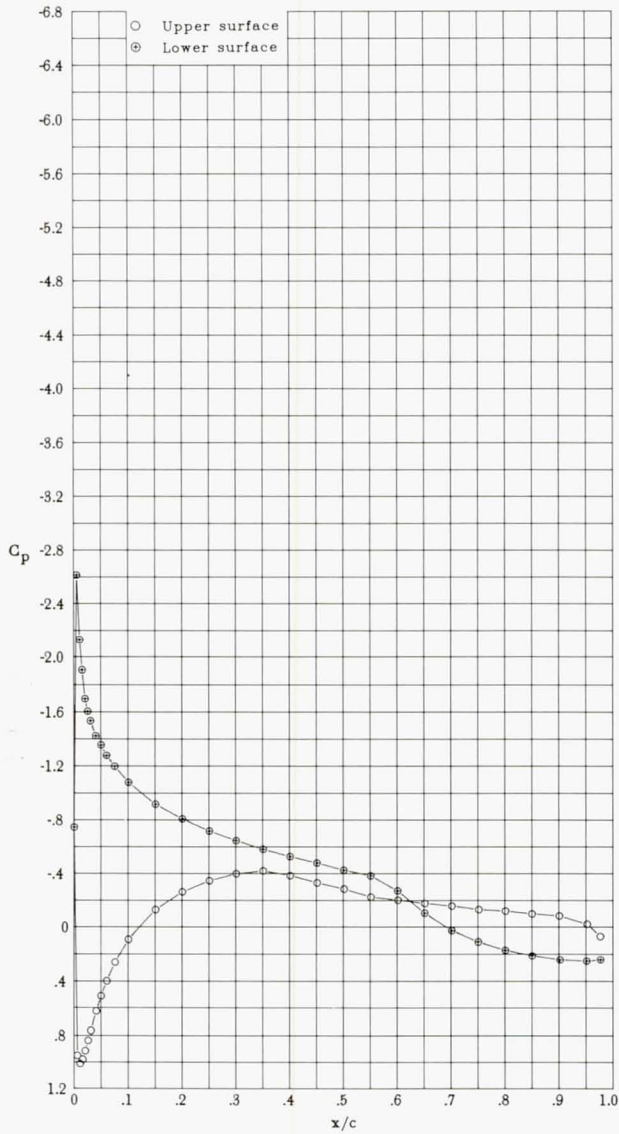


(i) $\alpha = -8.14^\circ$; $c_l = -0.502$; $c_d = 0.0111$; $c_m = -0.084$.

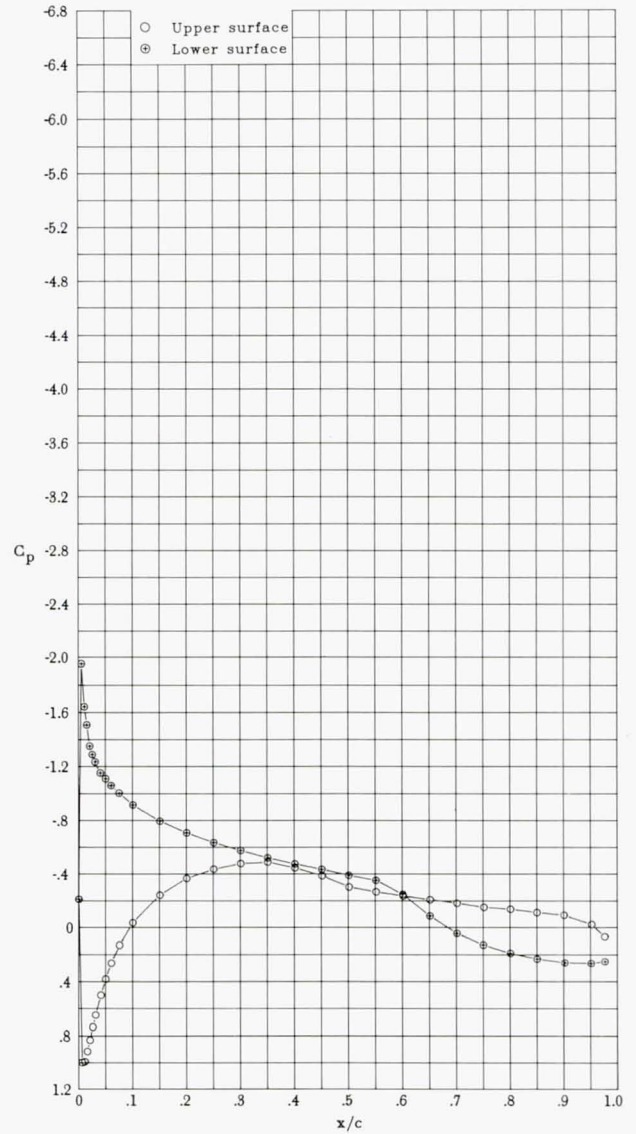


(j) $\alpha = -7.11^\circ$; $c_l = -0.385$; $c_d = 0.0101$; $c_m = -0.086$.

Figure 6.- Continued.

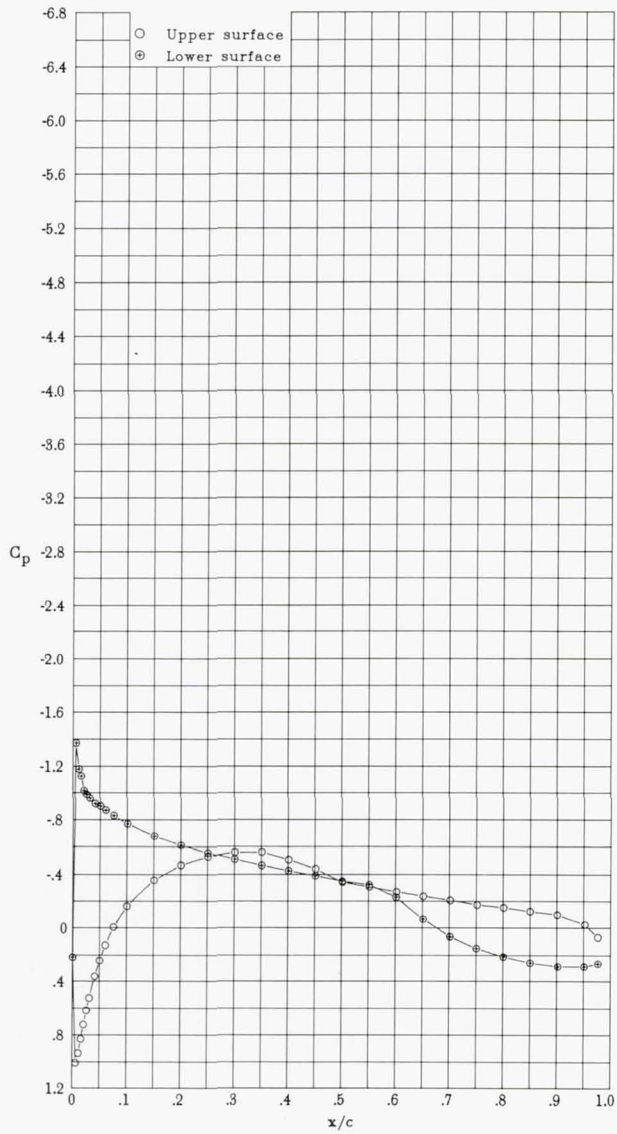


(k) $\alpha = -6.10^\circ$; $c_l = -0.269$; $c_d = 0.0093$; $c_m = -0.089$.

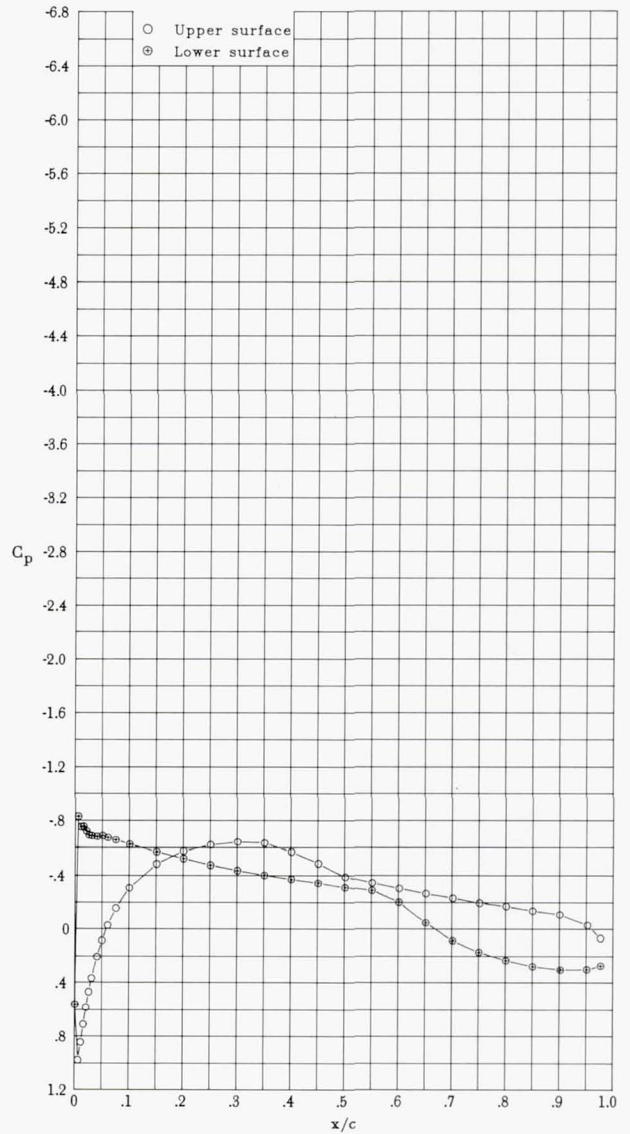


(l) $\alpha = -5.07^\circ$; $c_l = -0.149$; $c_d = 0.0083$; $c_m = -0.091$.

Figure 6.- Continued.

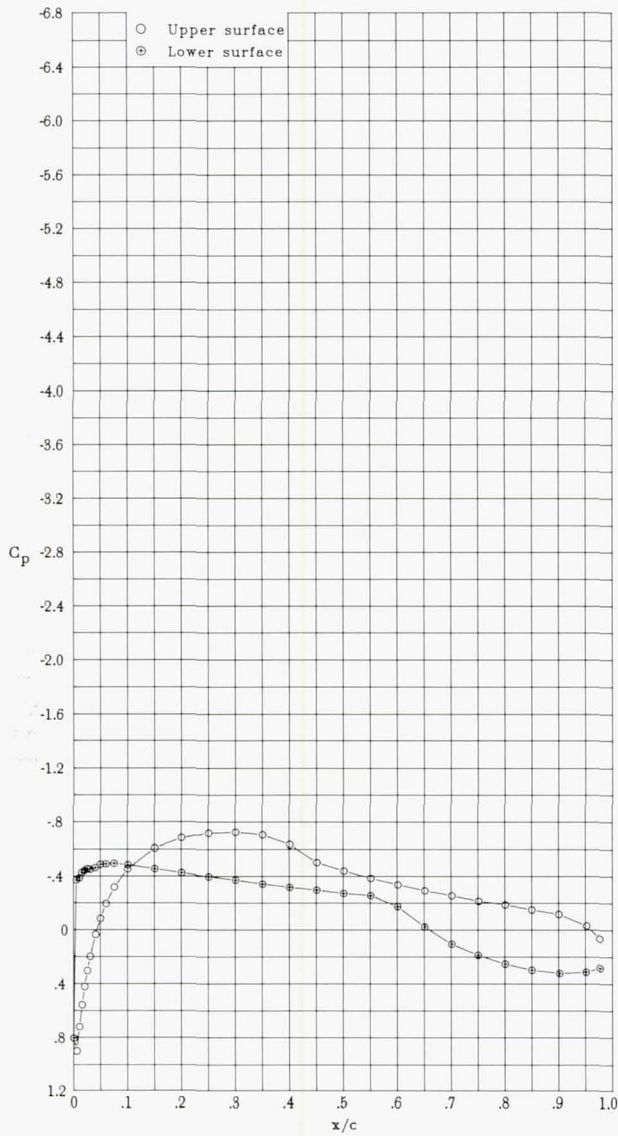


(m) $\alpha = -4.08^\circ$; $c_l = -0.031$; $c_d = 0.0073$; $c_m = -0.094$.

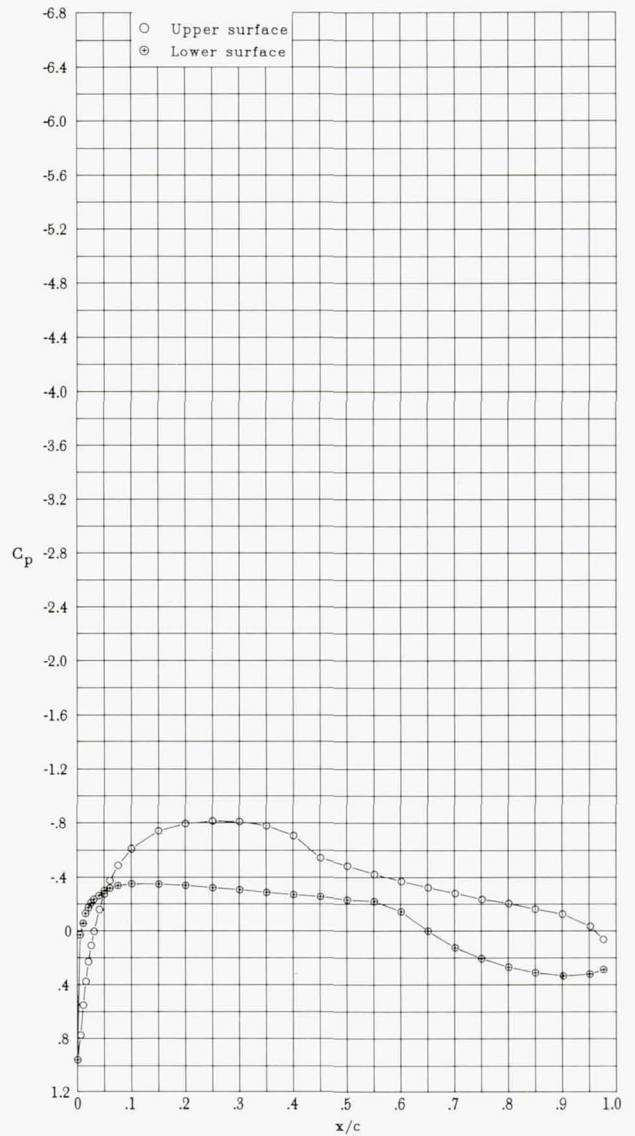


(n) $\alpha = -3.06^\circ$; $c_l = 0.090$; $c_d = 0.0065$; $c_m = -0.097$.

Figure 6.- Continued.

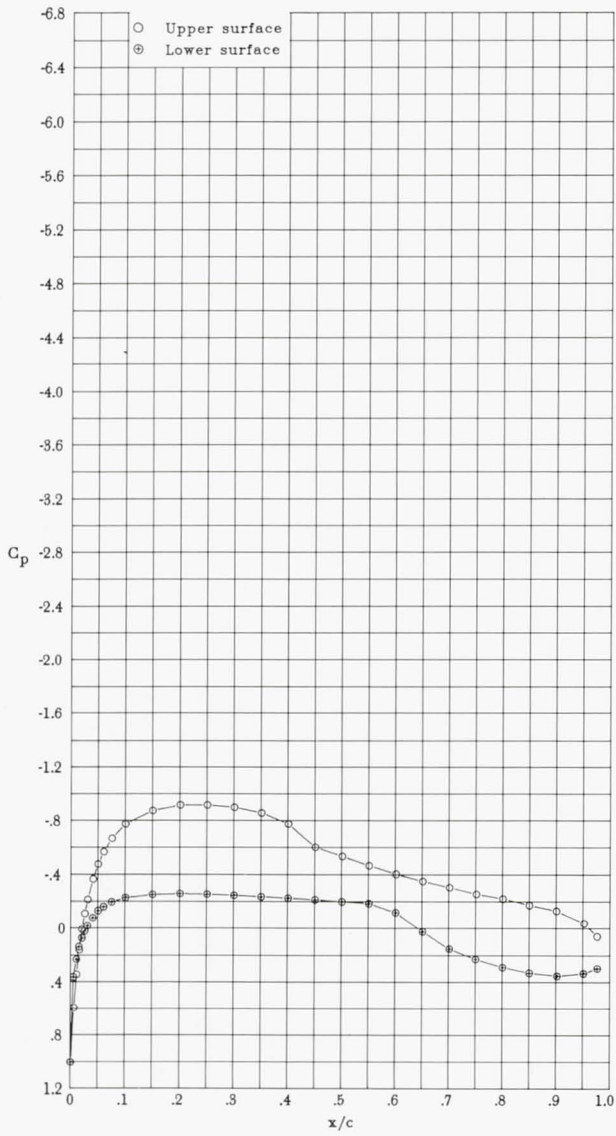


(o) $\alpha = -2.04^\circ$; $c_l = 0.208$; $c_d = 0.0062$; $c_m = -0.099$.

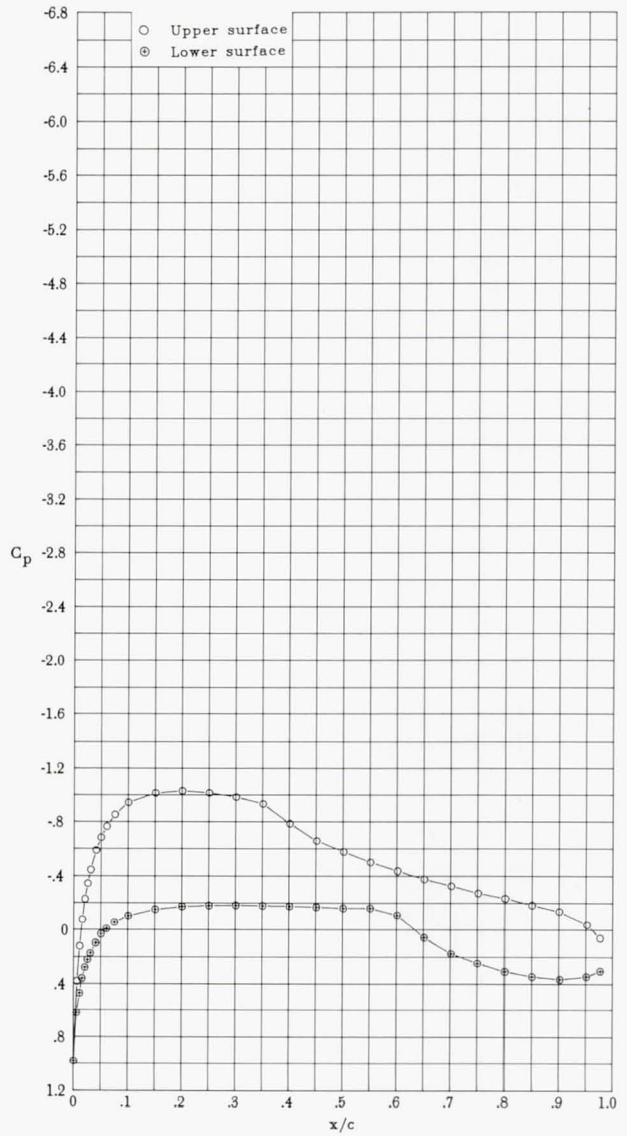


(p) $\alpha = -1.02^\circ$; $c_l = 0.327$; $c_d = 0.0060$; $c_m = -0.101$.

Figure 6.- Continued.

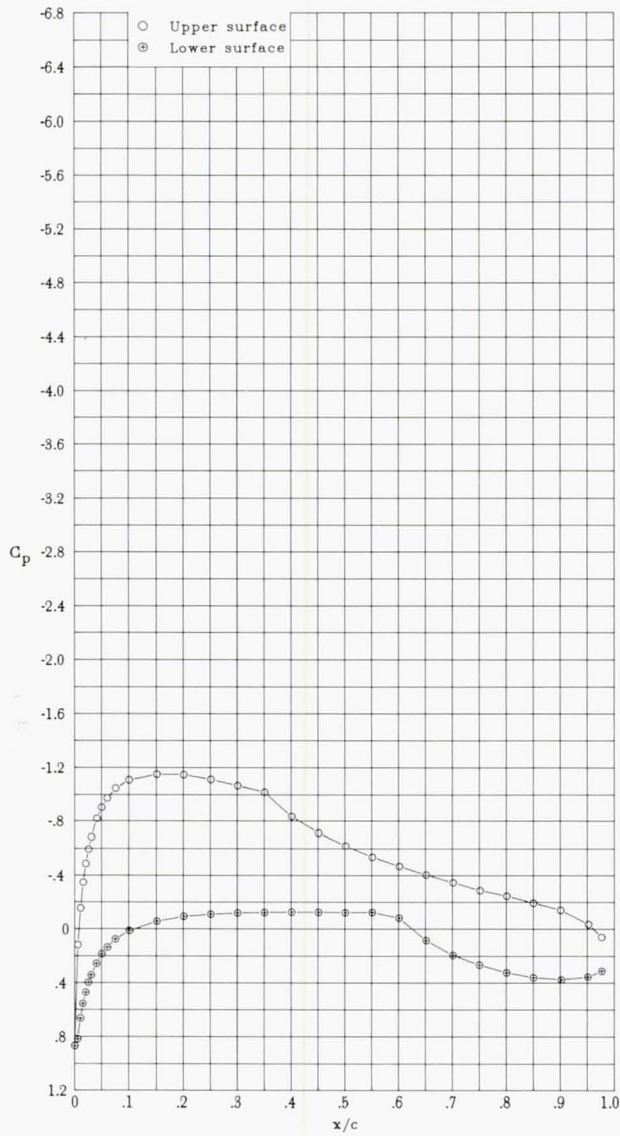


(q) $\alpha = 0.01^\circ$; $c_l = 0.447$; $c_d = 0.0059$; $c_m = -0.104$.

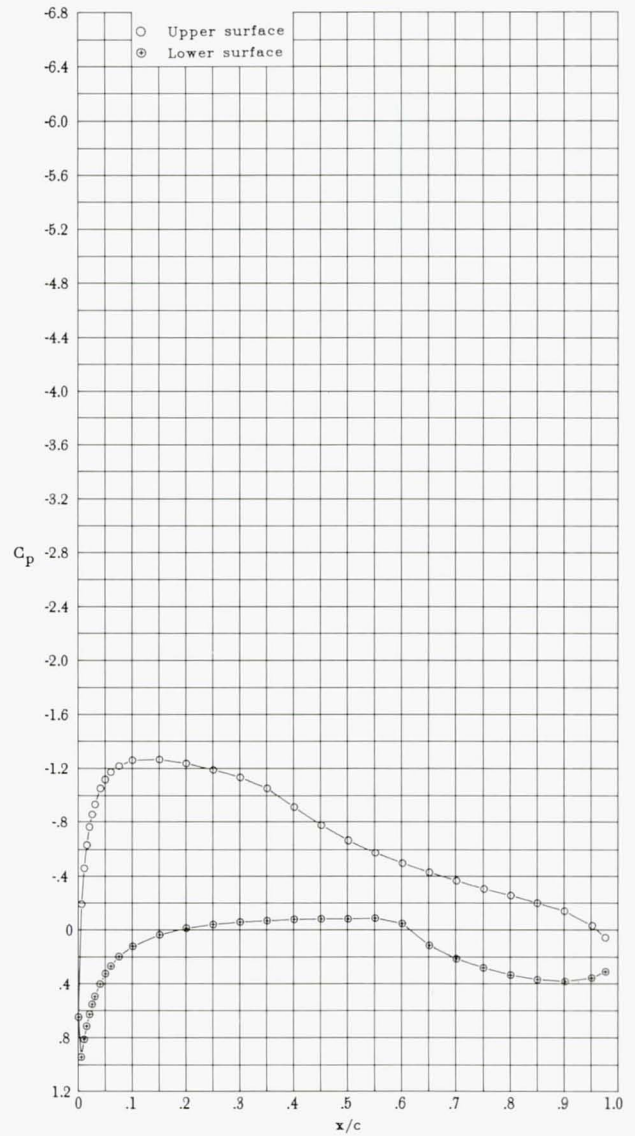


(r) $\alpha = 1.01^\circ$; $c_l = 0.561$; $c_d = 0.0059$; $c_m = -0.106$.

Figure 6.- Continued.

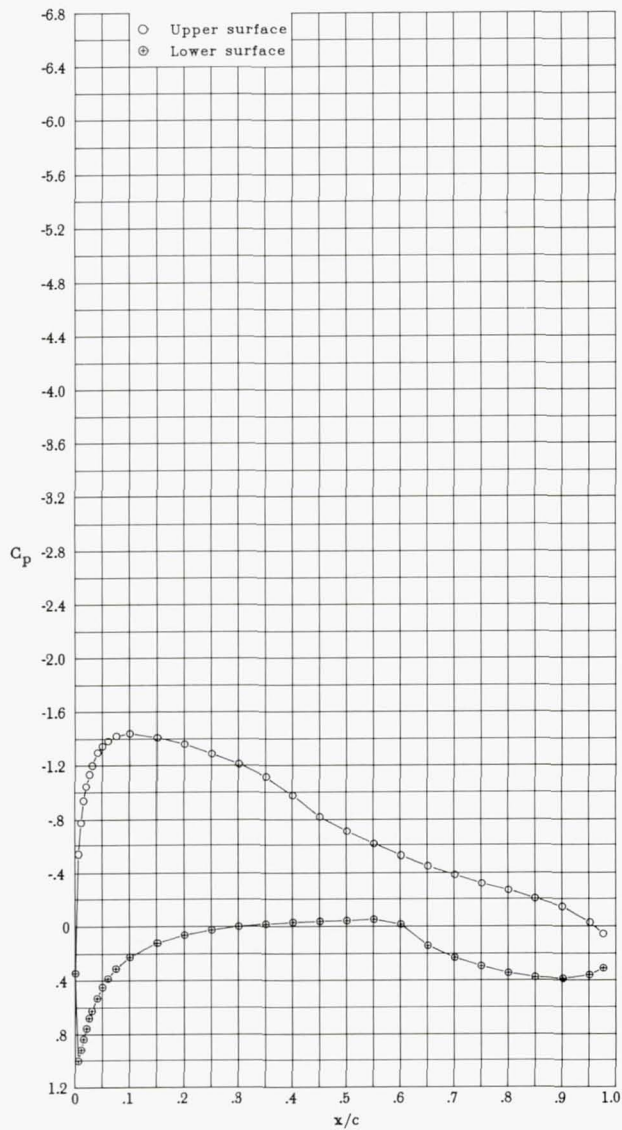


(s) $\alpha = 2.03^\circ$; $c_l = 0.677$; $c_d = 0.0061$; $c_m = -0.107$.

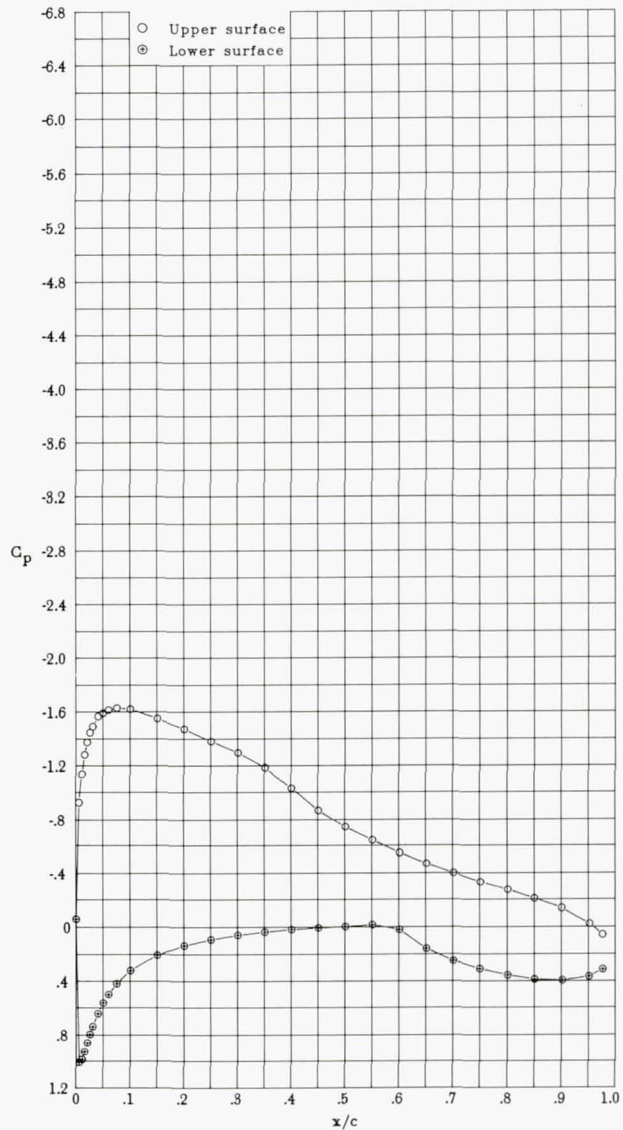


(t) $\alpha = 3.06^\circ$; $c_l = 0.784$; $c_d = 0.0062$; $c_m = -0.108$.

Figure 6.- Continued.

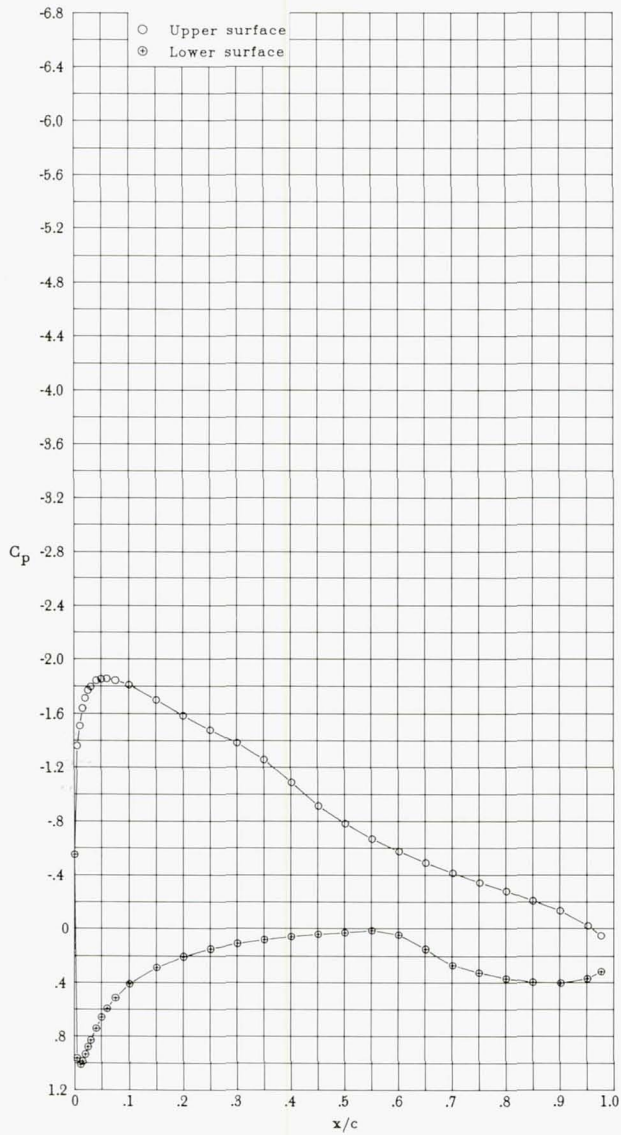


(u) $\alpha = 4.07^\circ$; $c_l = 0.894$; $c_d = 0.0067$; $c_m = -0.108$.

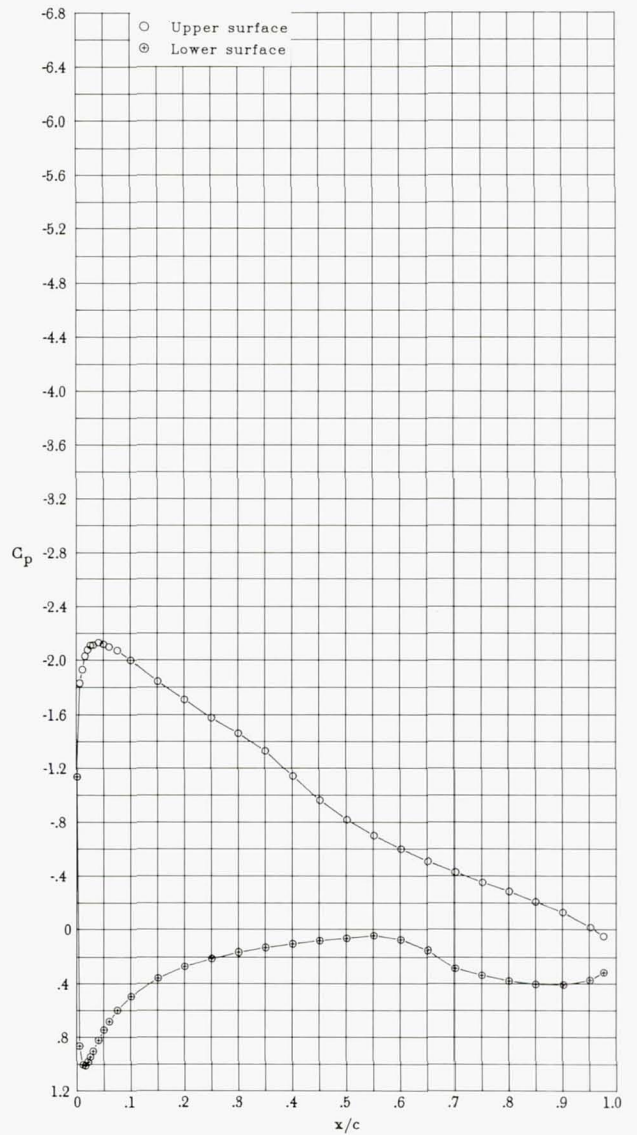


(v) $\alpha = 5.09^\circ$; $c_l = 1.004$; $c_d = 0.0076$; $c_m = -0.108$.

Figure 6.- Continued.

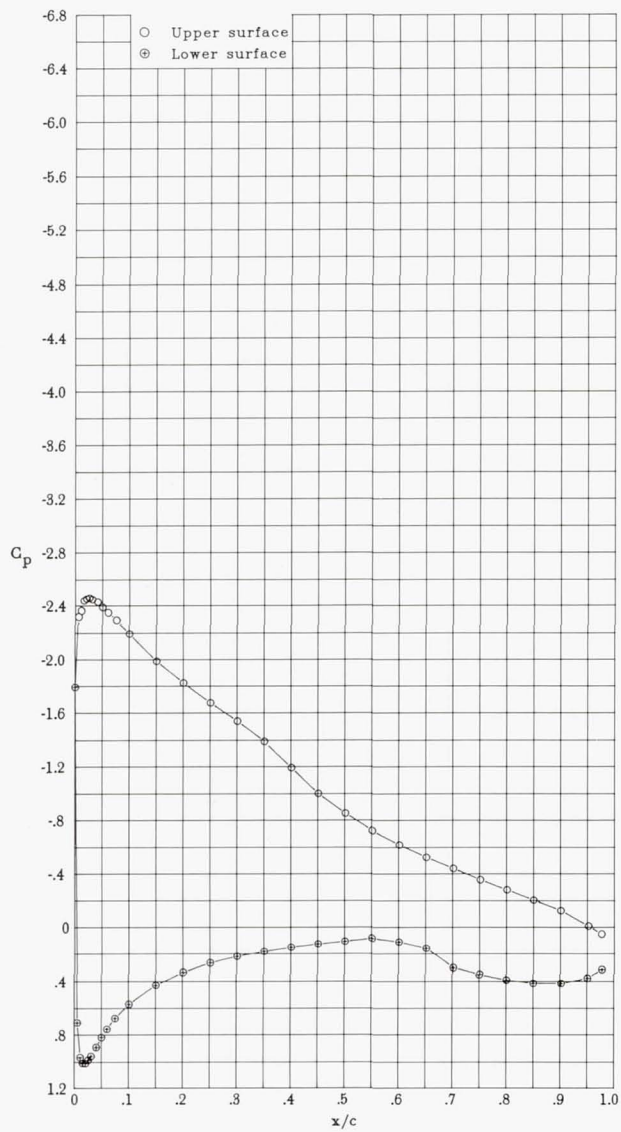


(w) $\alpha = 6.10^\circ$; $c_l = 1.110$; $c_d = 0.0087$; $c_m = -0.107$.

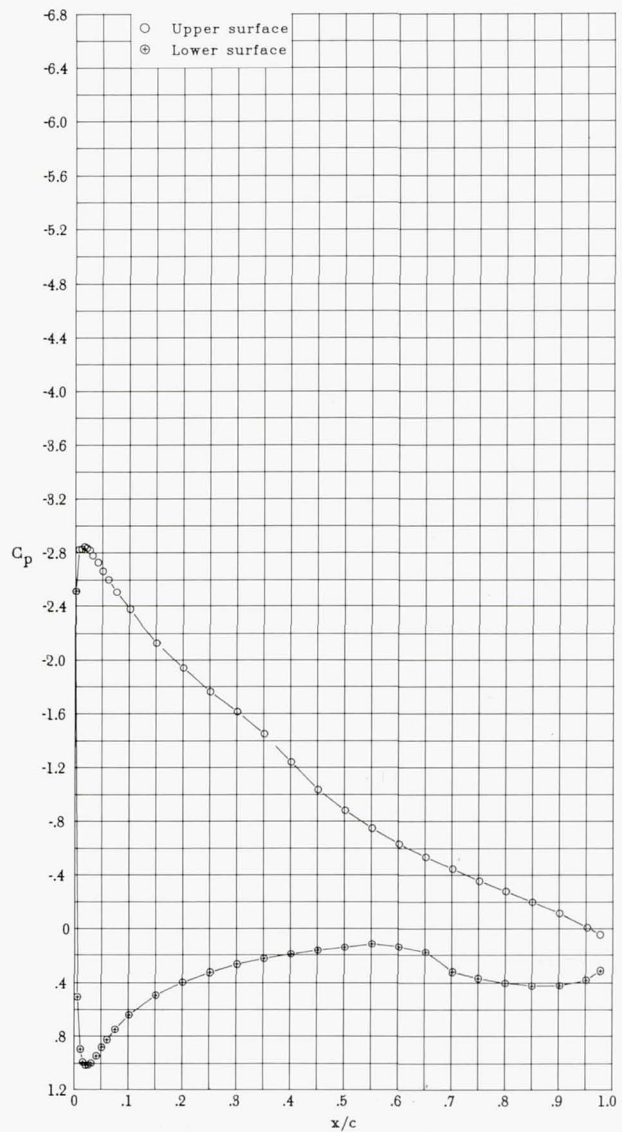


(x) $\alpha = 7.13^\circ$; $c_l = 1.216$; $c_d = 0.0097$; $c_m = -0.106$.

Figure 6.- Continued.

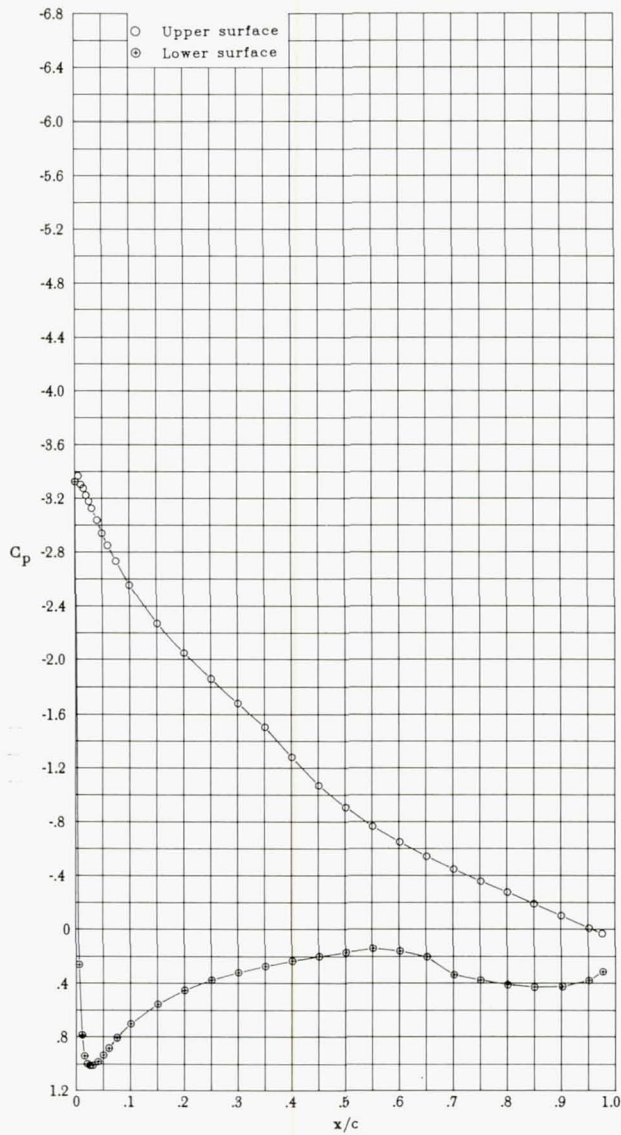


(y) $\alpha = 8.16^\circ$; $c_l = 1.317$; $c_d = 0.0107$; $c_m = -0.105$.

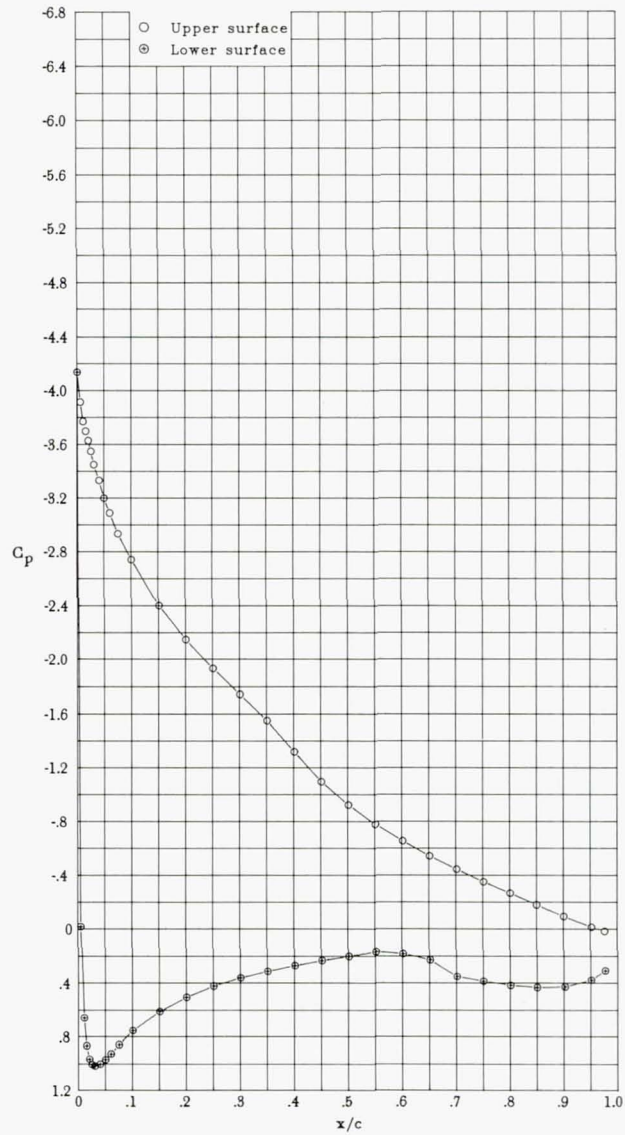


(z) $\alpha = 9.16^\circ$; $c_l = 1.415$; $c_d = 0.0116$; $c_m = -0.103$.

Figure 6.- Continued.

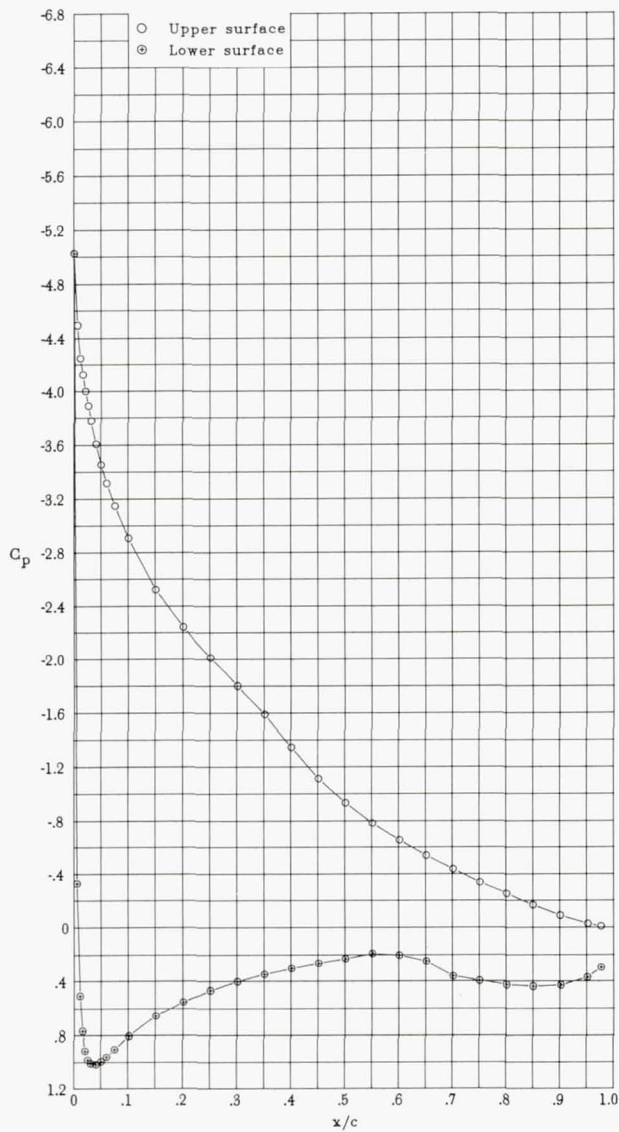


(aa) $\alpha = 10.18^\circ$; $c_l = 1.508$; $c_d = 0.0132$; $c_m = -0.101$.

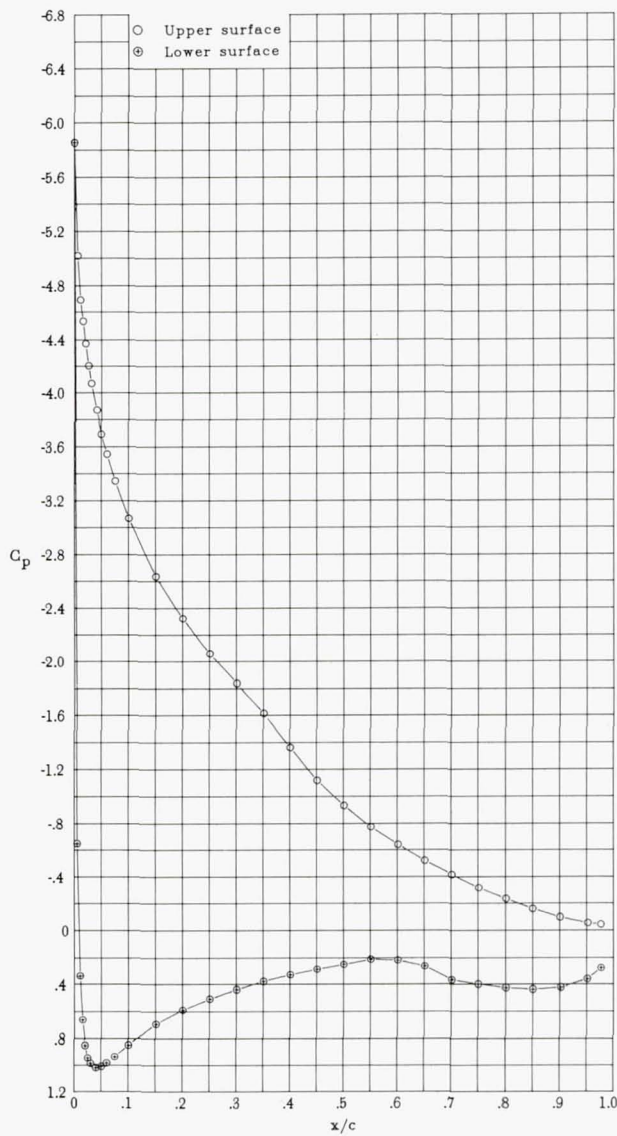


(bb) $\alpha = 11.19^\circ$; $c_l = 1.593$; $c_d = 0.0150$; $c_m = -0.098$.

Figure 6.- Continued.

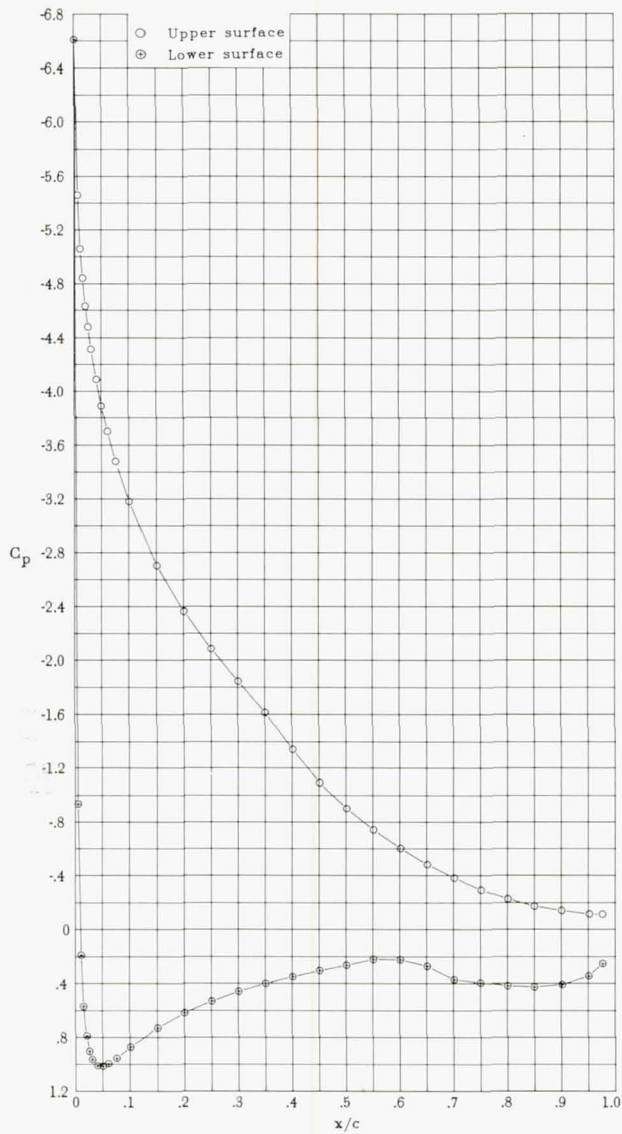


(cc) $\alpha = 12.21^\circ$; $c_l = 1.669$; $c_d = 0.0178$; $c_m = -0.094$.

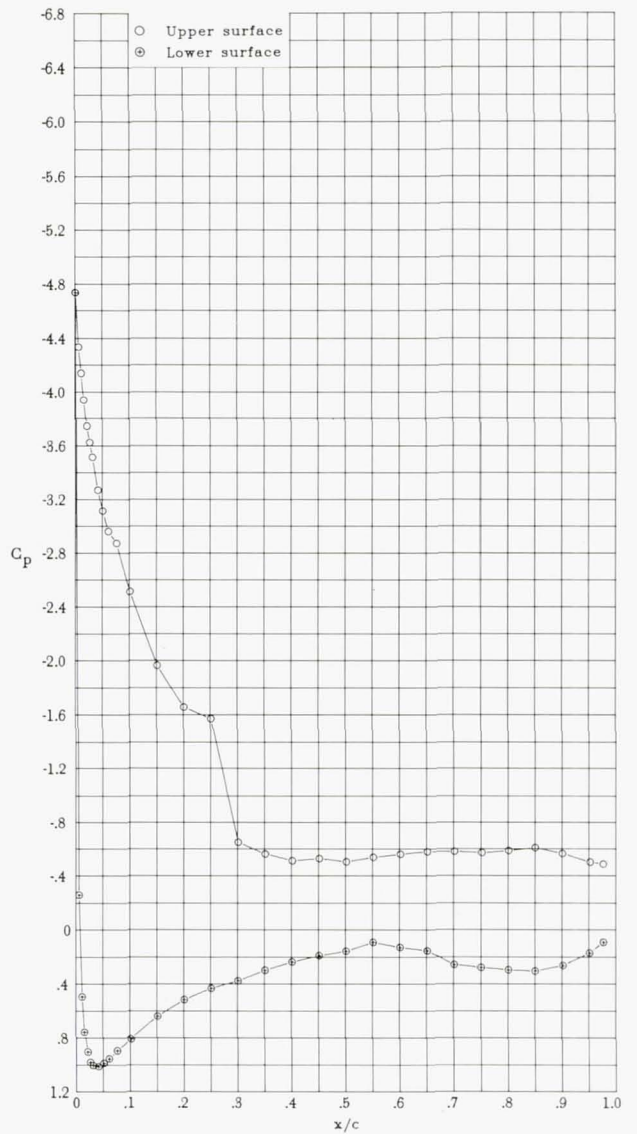


(dd) $\alpha = 13.24^\circ$; $c_l = 1.731$; $c_d = 0.0212$; $c_m = -0.090$.

Figure 6.- Continued.

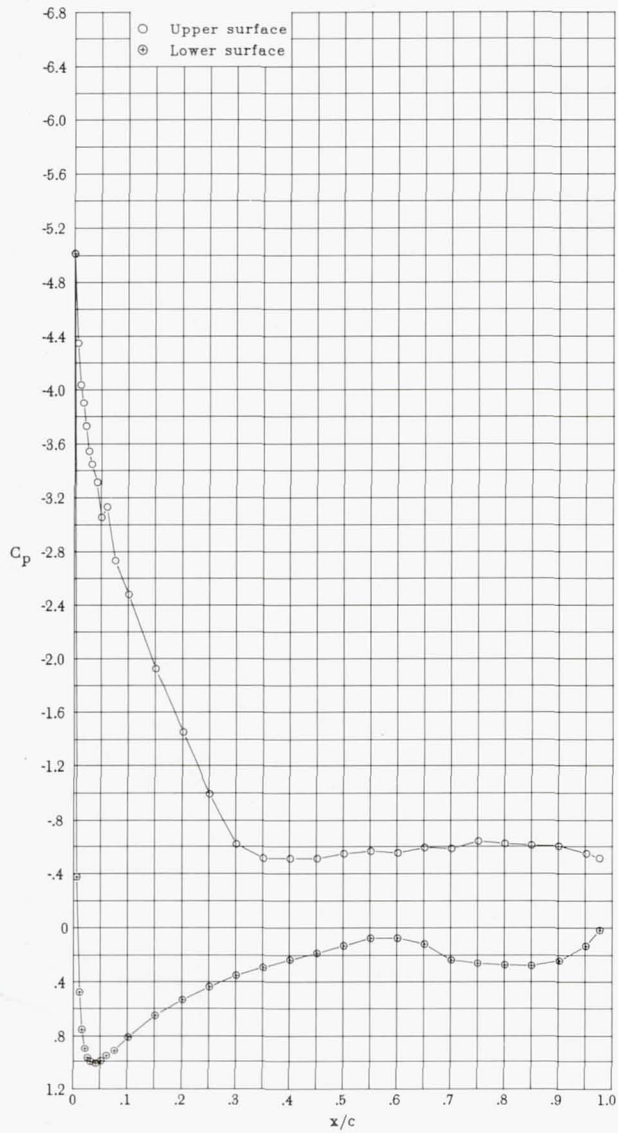


(ee) $\alpha = 14.23^\circ$; $c_l = 1.765$; $c_d = 0.0249$; $c_m = -0.085$.

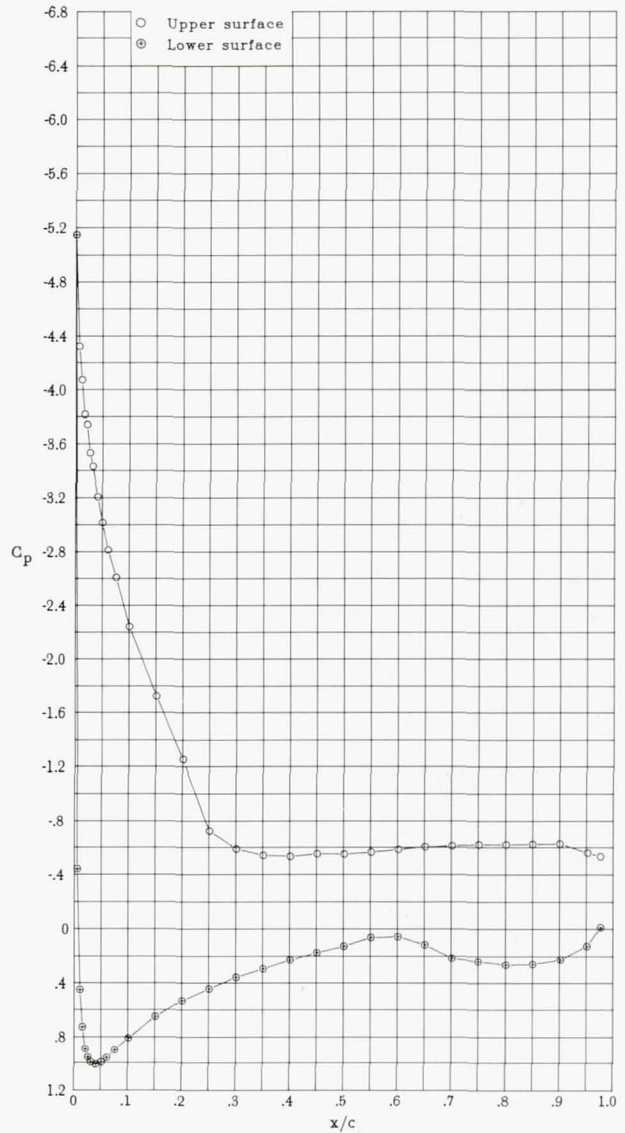


(ff) $\alpha = 15.17^\circ$; $c_l = 1.346$; $c_d = 0.1550$; $c_m = -0.109$.

Figure 6.- Continued.

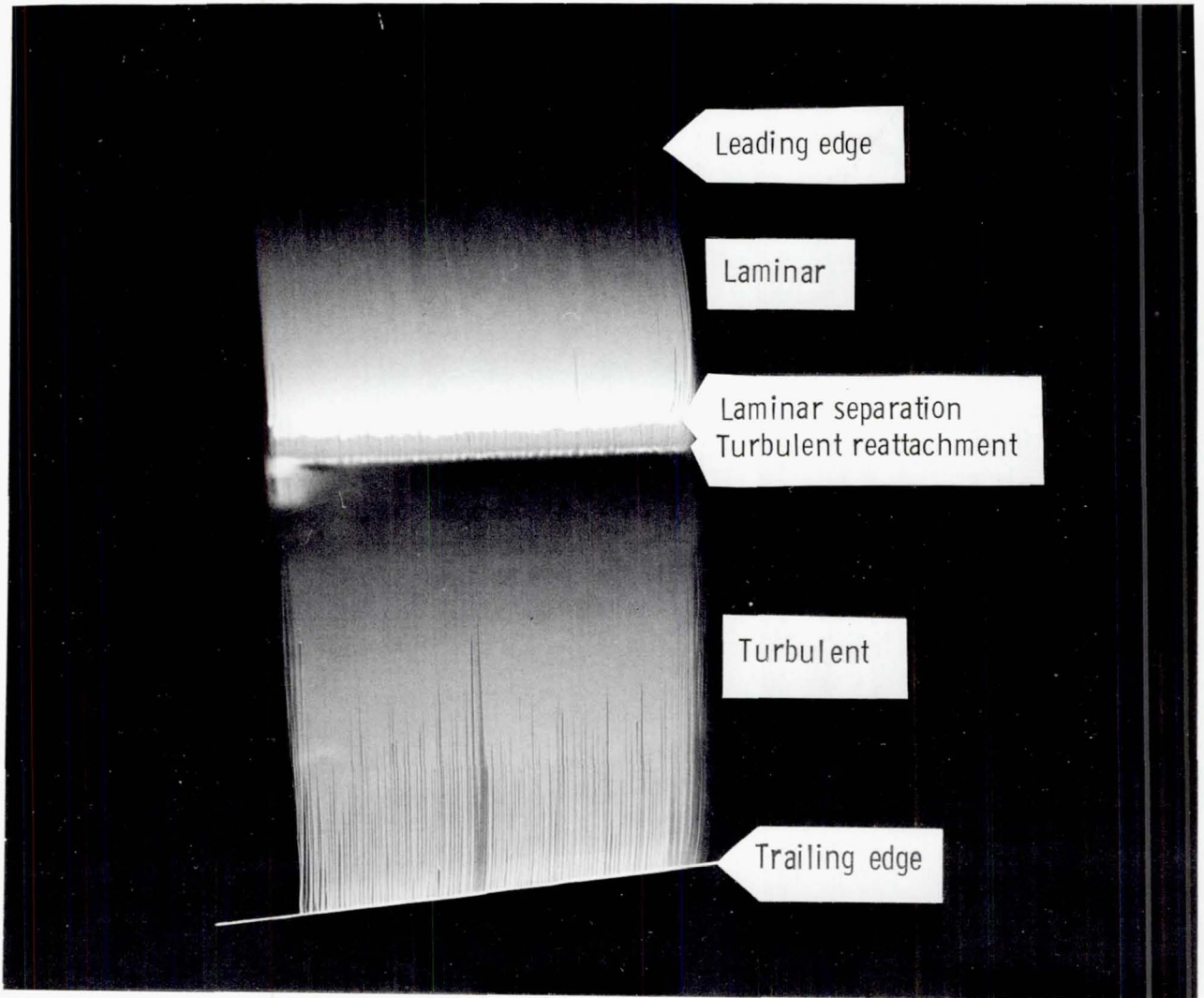


(gg) $\alpha = 16.17^\circ$; $c_l = 1.291$; $c_d = 0.1762$; $c_m = -0.108$.



(hh) $\alpha = 17.16^\circ$; $c_l = 1.234$; $c_d = 0.1977$; $c_m = -0.110$.

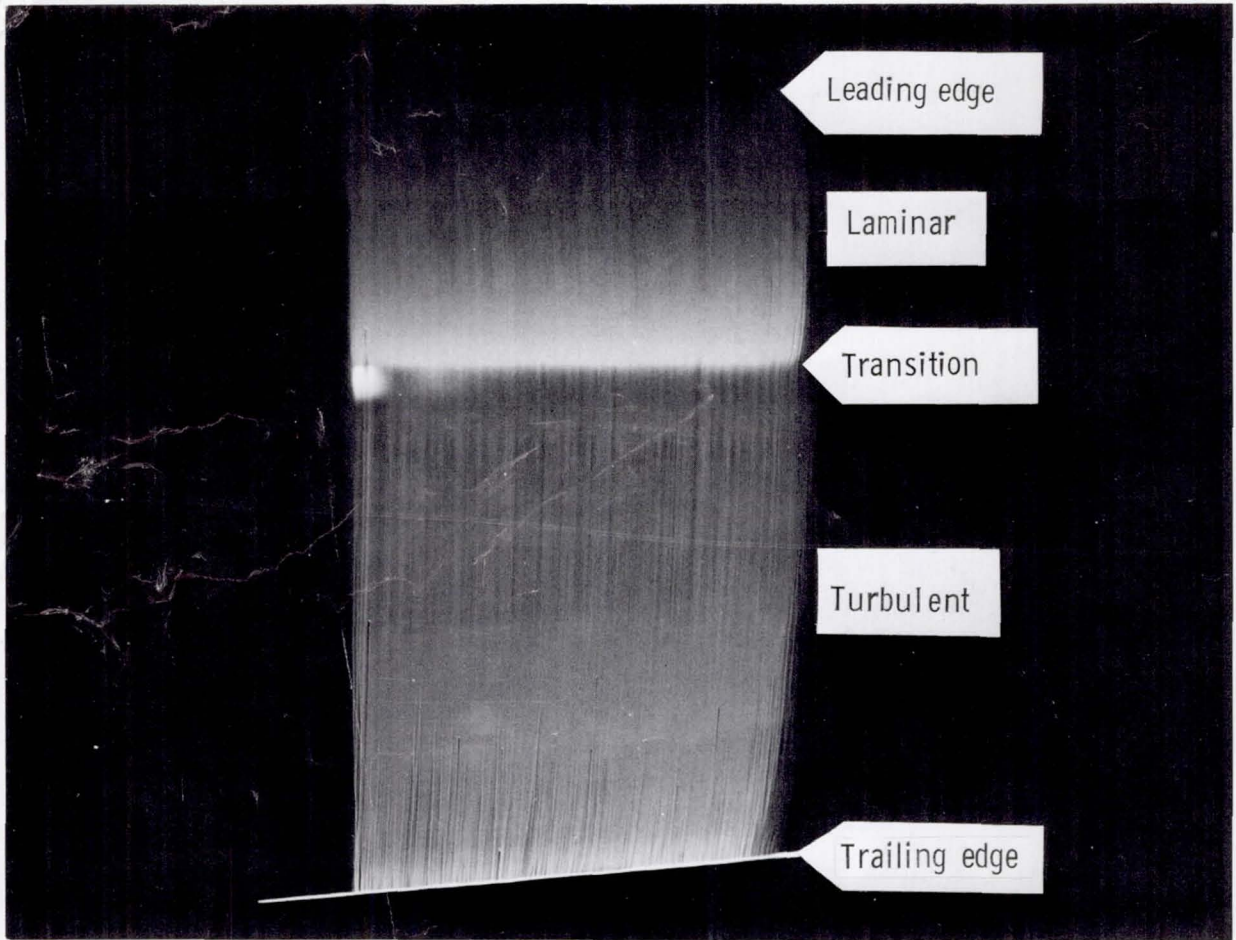
Figure 6.- Concluded.



L-81-123

(a) $\alpha = 0.0^\circ$; $c_l = 0.4$.

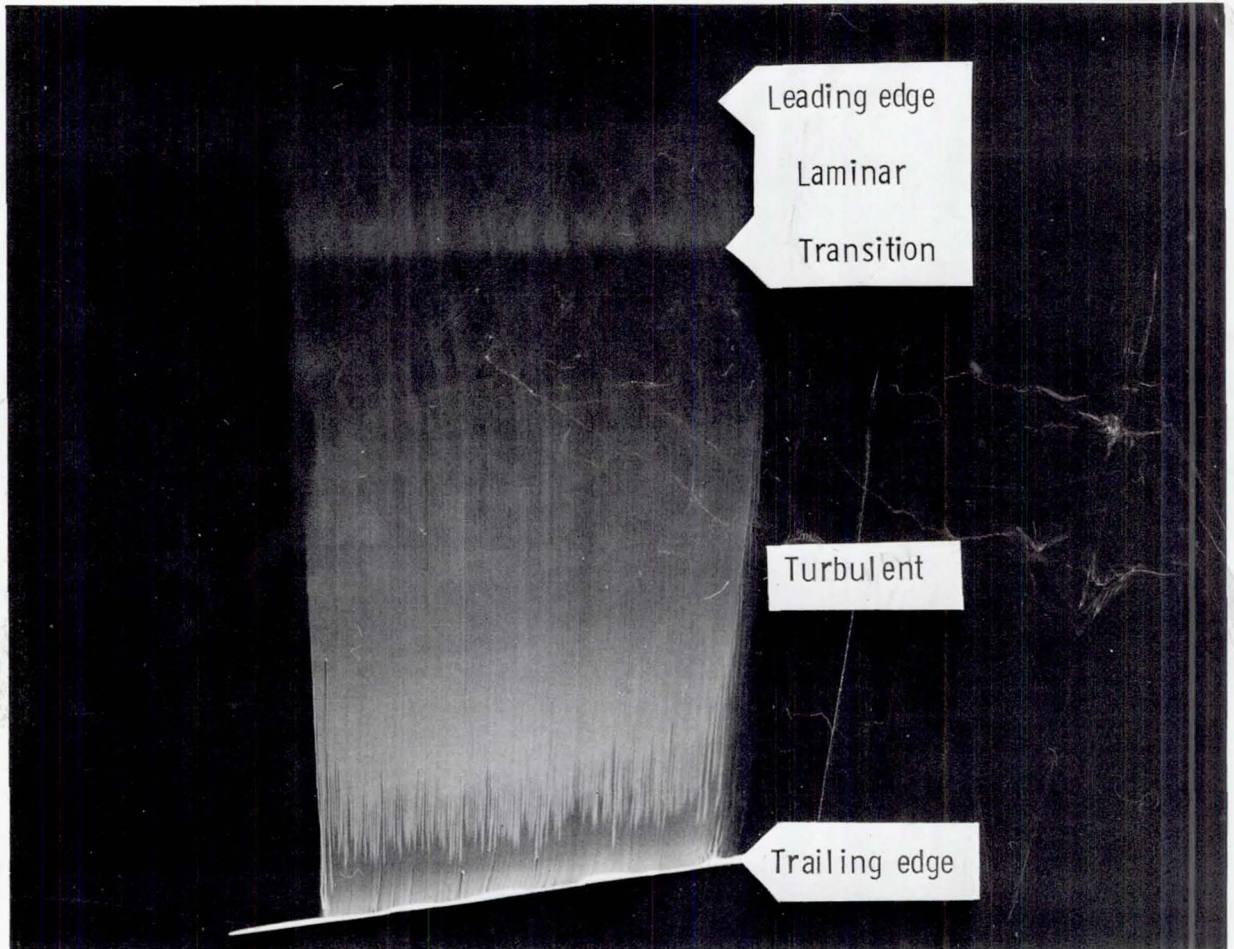
Figure 7.- Oil-flow photographs of upper surface for $R = 2.0 \times 10^6$
and $M = 0.14$.



(b) $\alpha = 4.0^\circ$; $c_l = 0.9$.

L-81-124

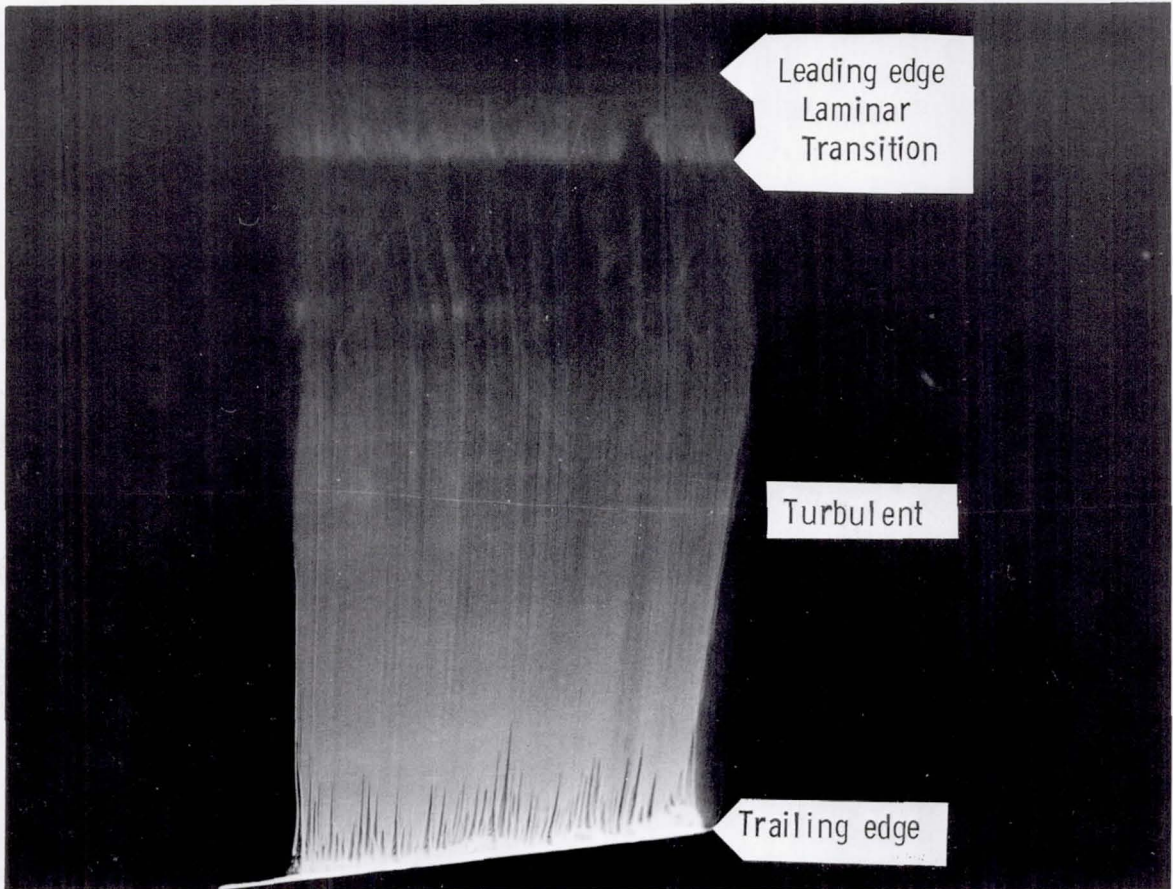
Figure 7.- Continued.



(c) $\alpha = 8.0^\circ$; $c_l = 1.3$.

L-81-125

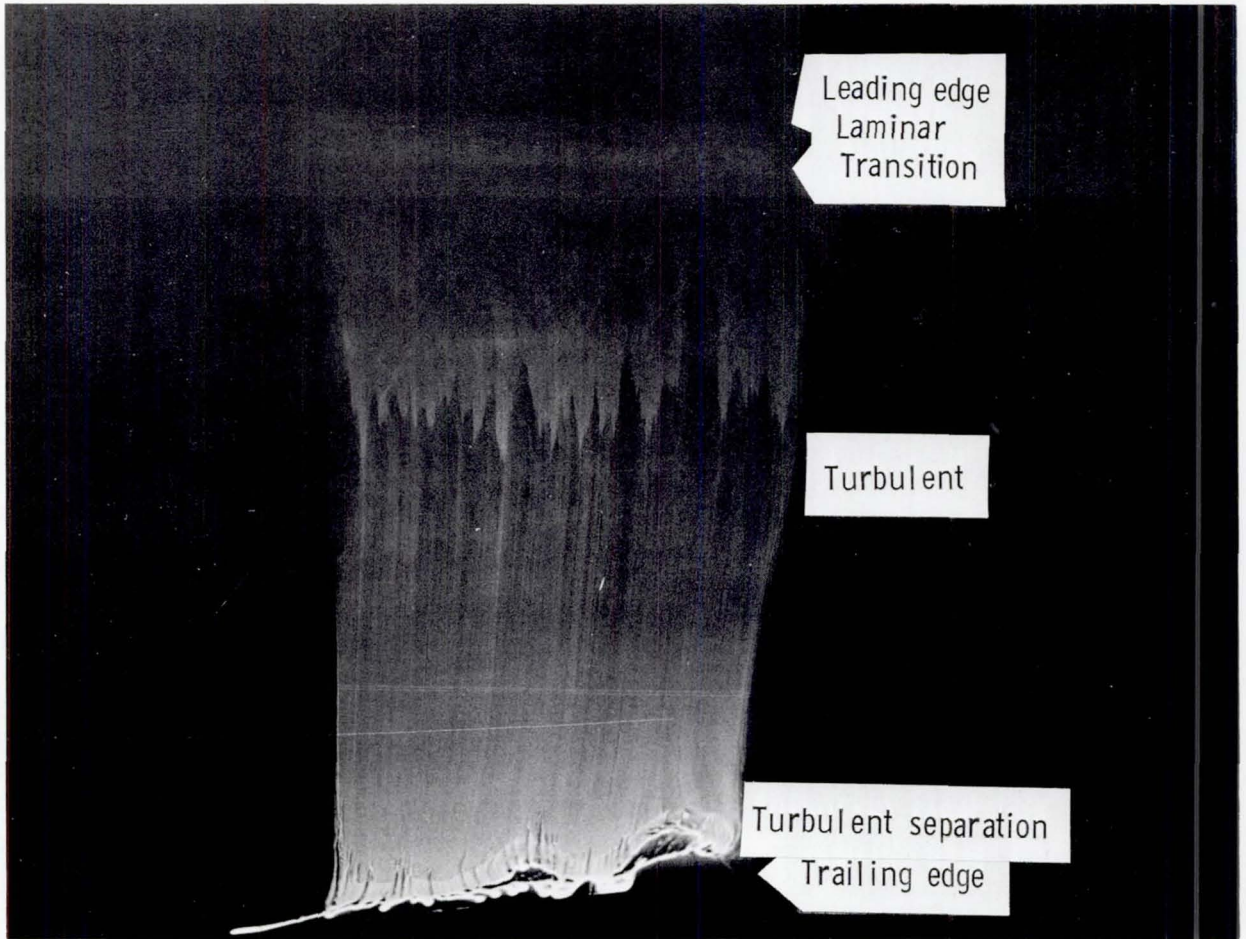
Figure 7.- Continued.



(d) $\alpha = 10.0^\circ$; $c_l = 1.5$.

L-81-126

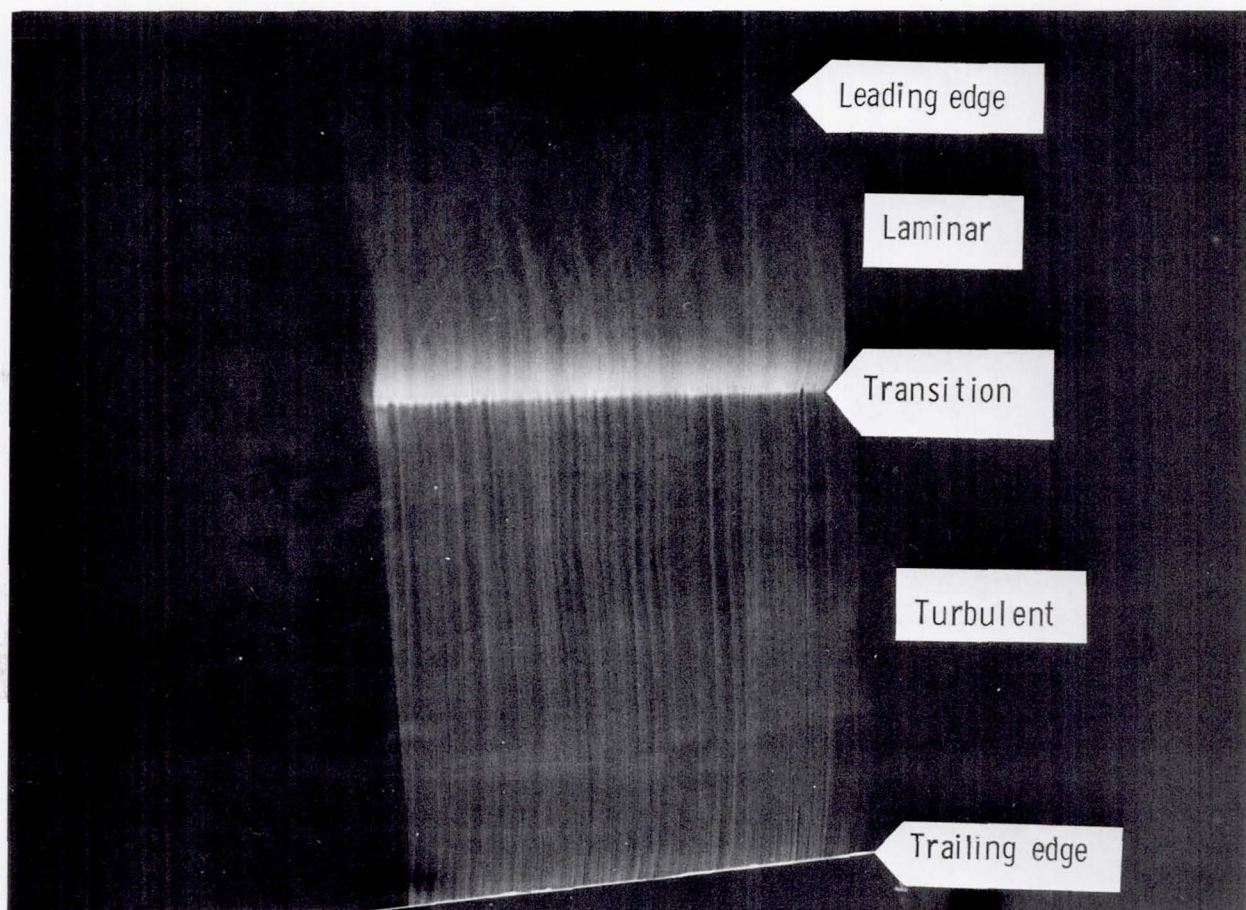
Figure 7.- Continued.



(e) $\alpha = 12.0^\circ$; $c_l = 1.6$.

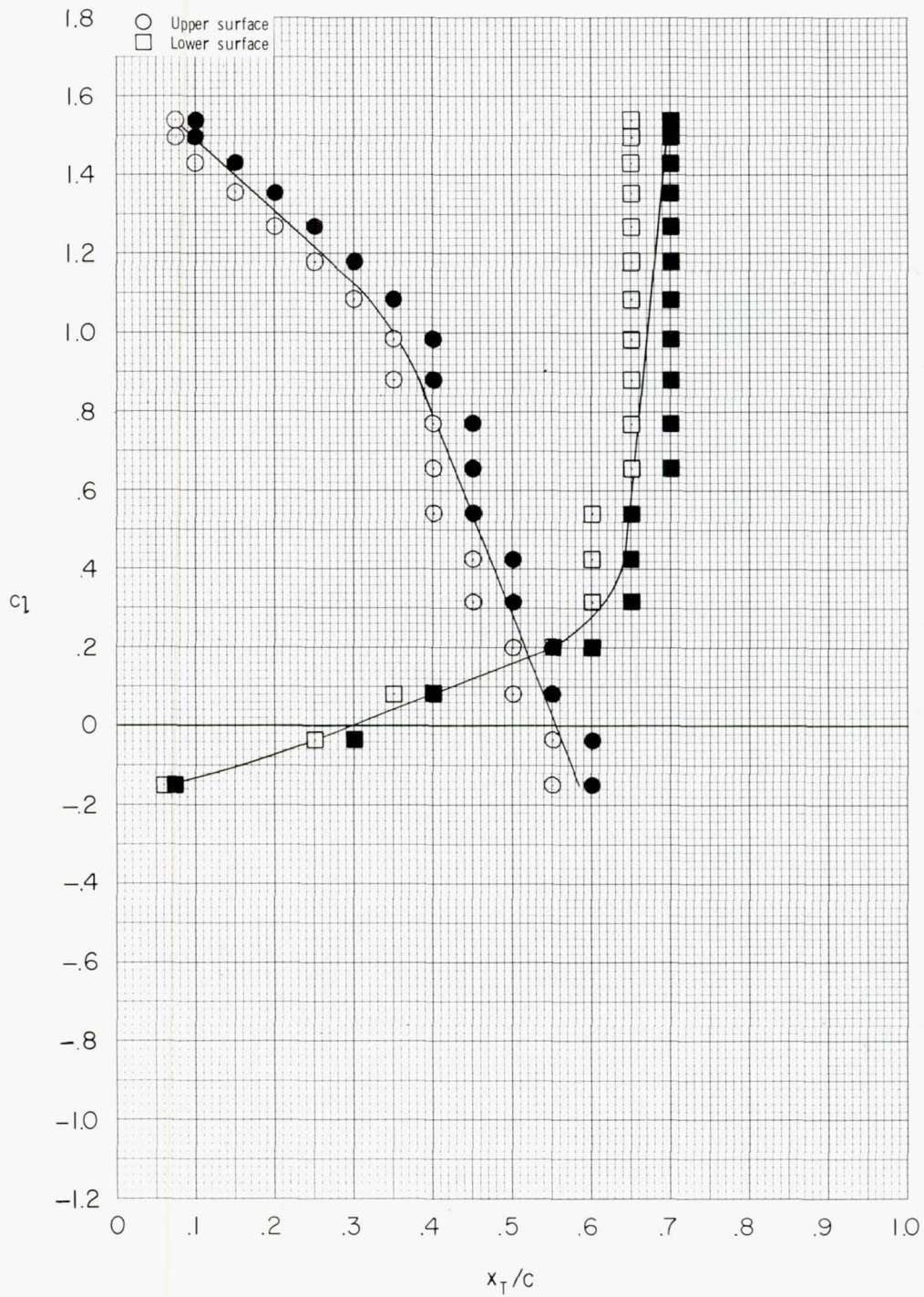
L-81-127

Figure 7.- Concluded.



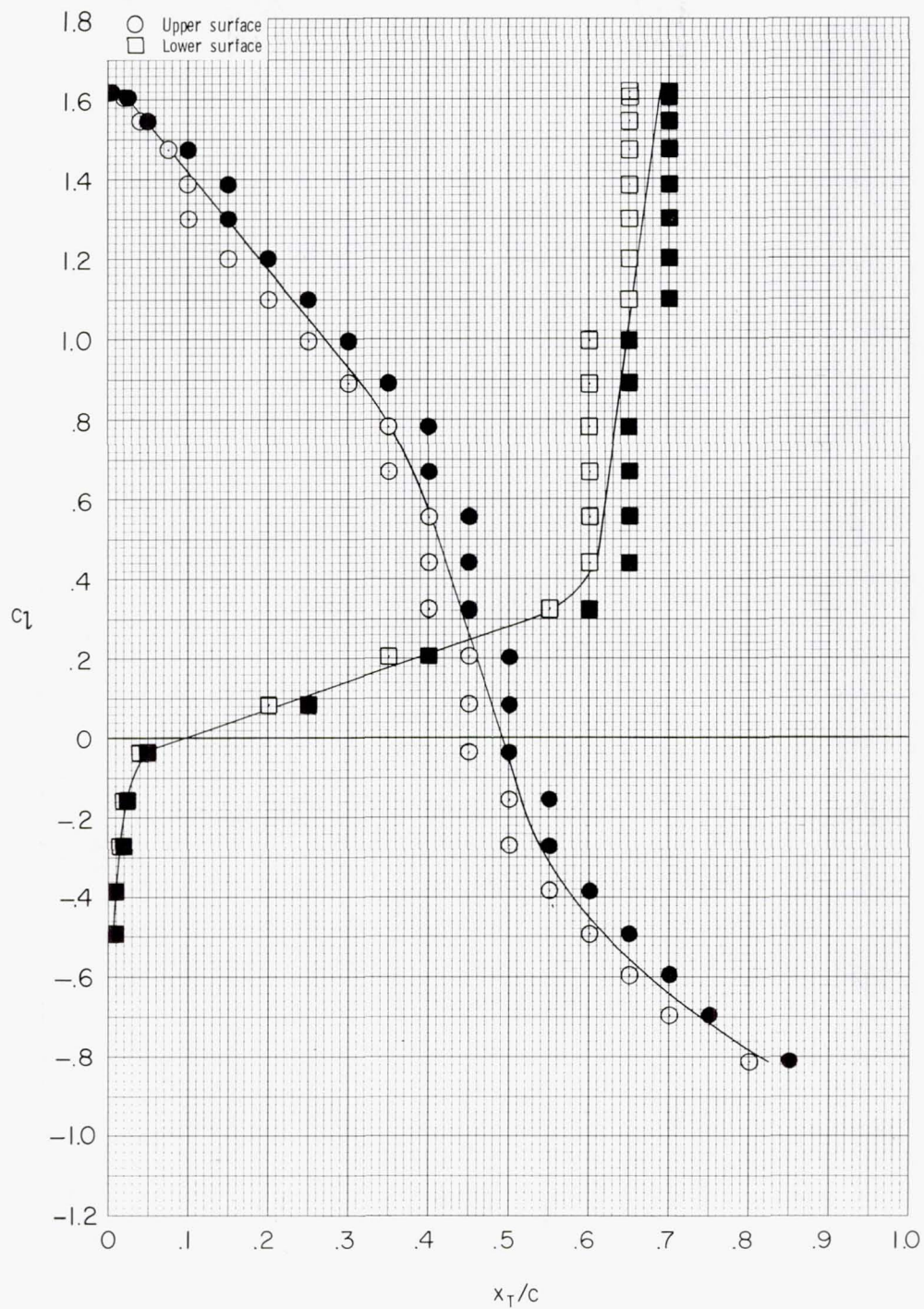
L-81-128

Figure 8.- Oil-flow photograph of upper surface for $R = 4.0 \times 10^6$, $M = 0.29$,
 $\alpha = 0.0^\circ$, and $c_l = 0.5$.



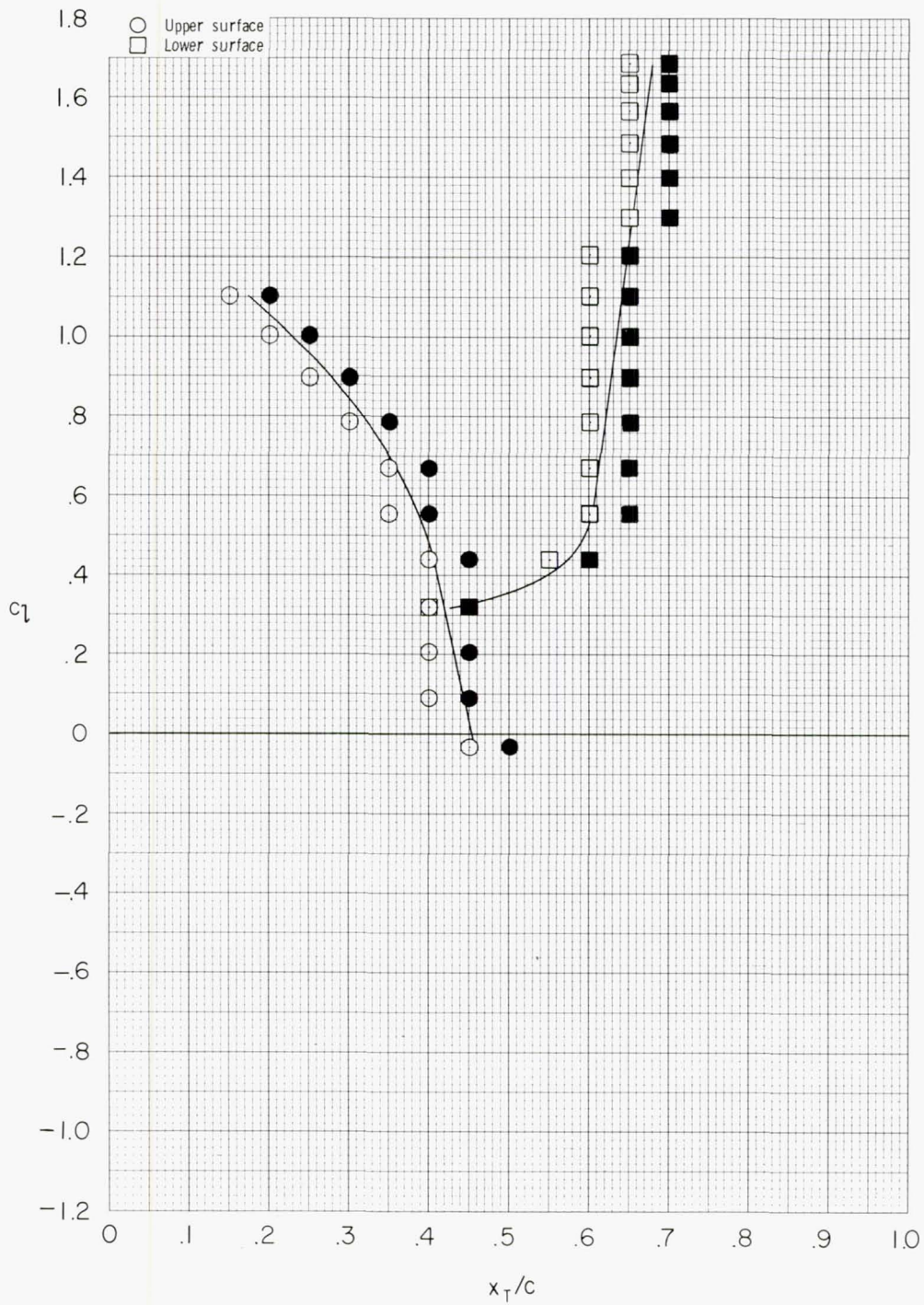
(a) $R = 1.0 \times 10^6$.

Figure 9.- Transition location ($M = 0.10$). Open symbols correspond to orifices at which flow is laminar; solid symbols, orifices at which flow is turbulent.



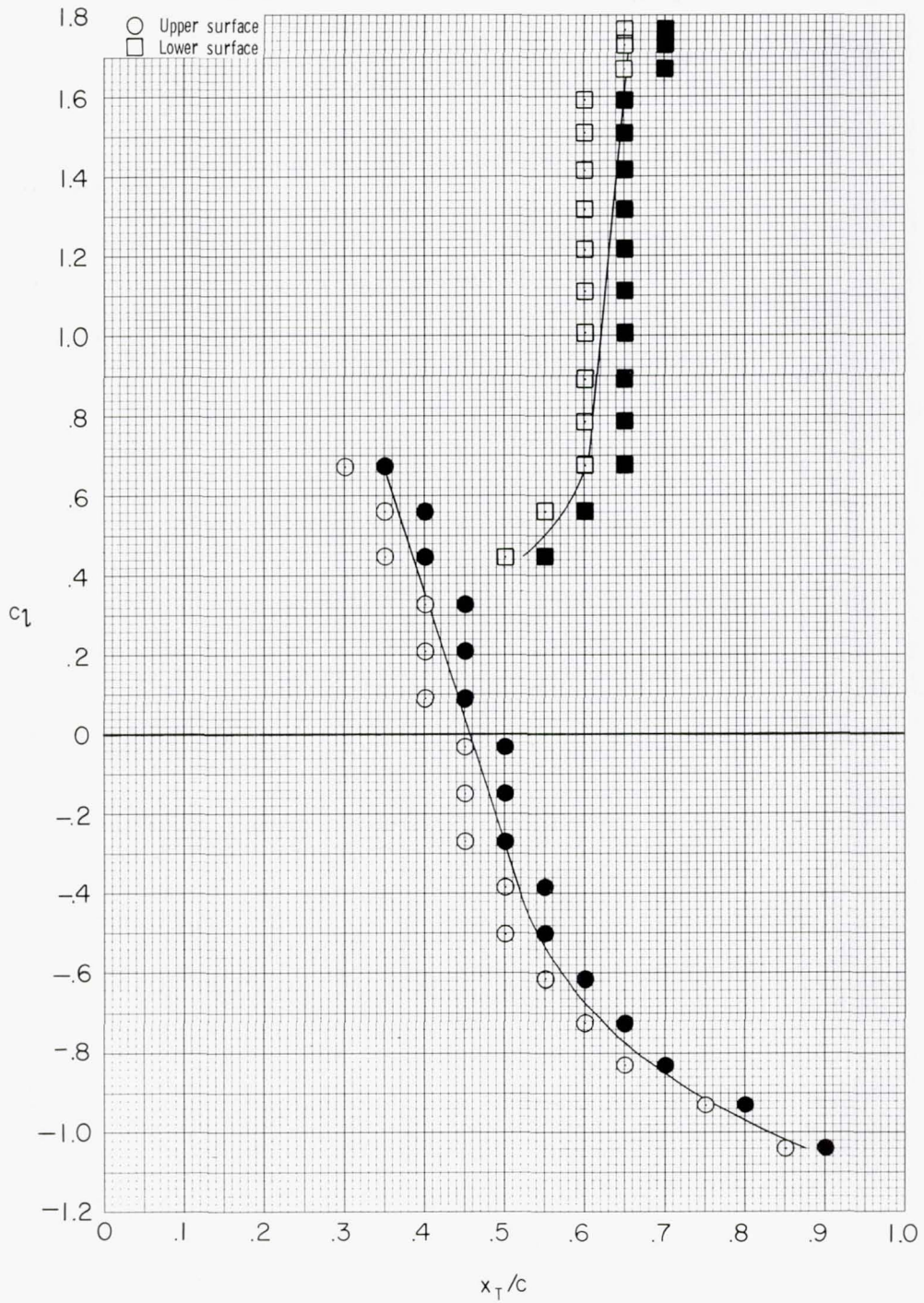
(b) $R = 2.0 \times 10^6$.

Figure 9.- Continued.



(c) $R = 3.0 \times 10^6$.

Figure 9.- Continued.



(d) $R = 4.0 \times 10^6$.

Figure 9.- Concluded.

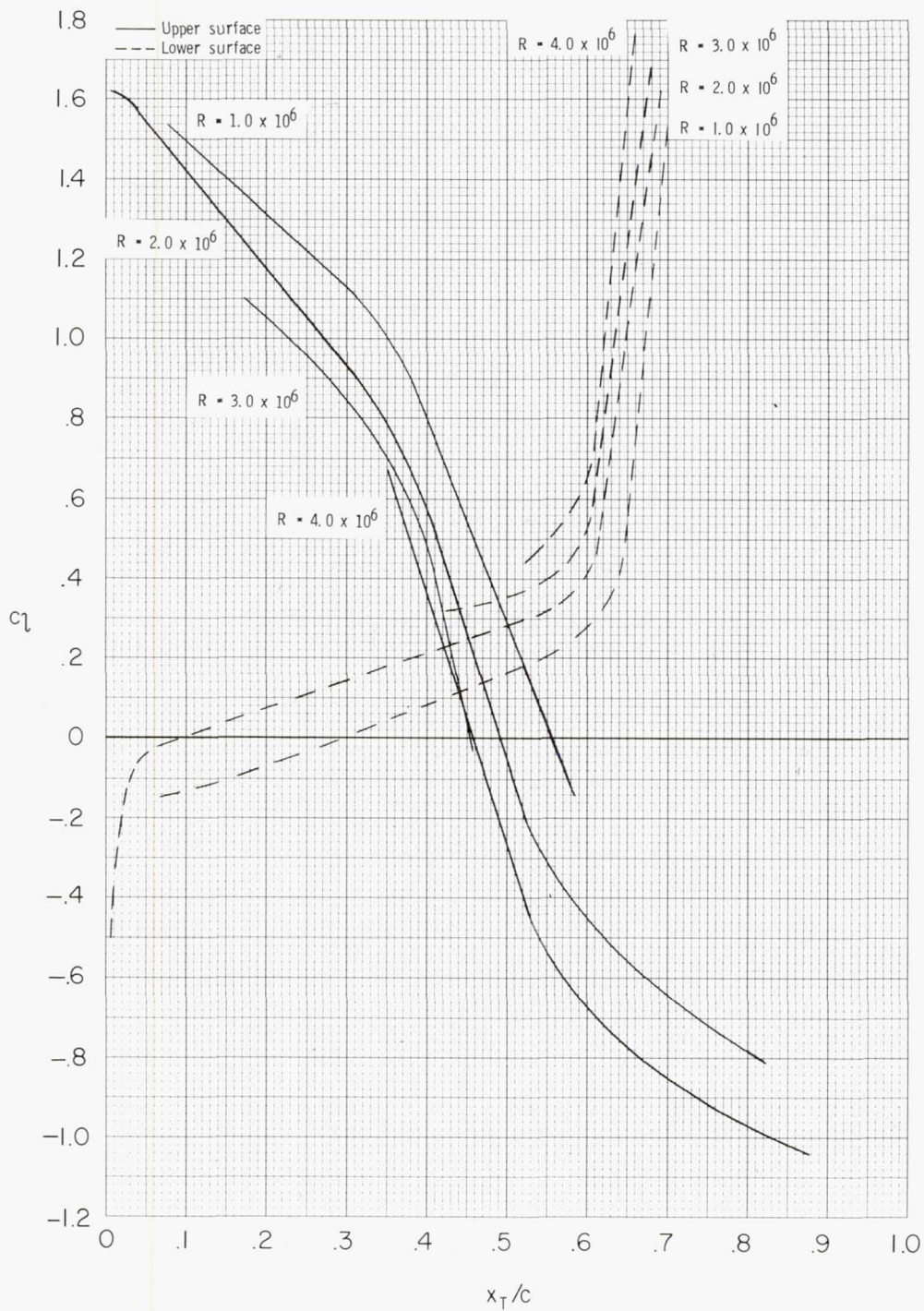
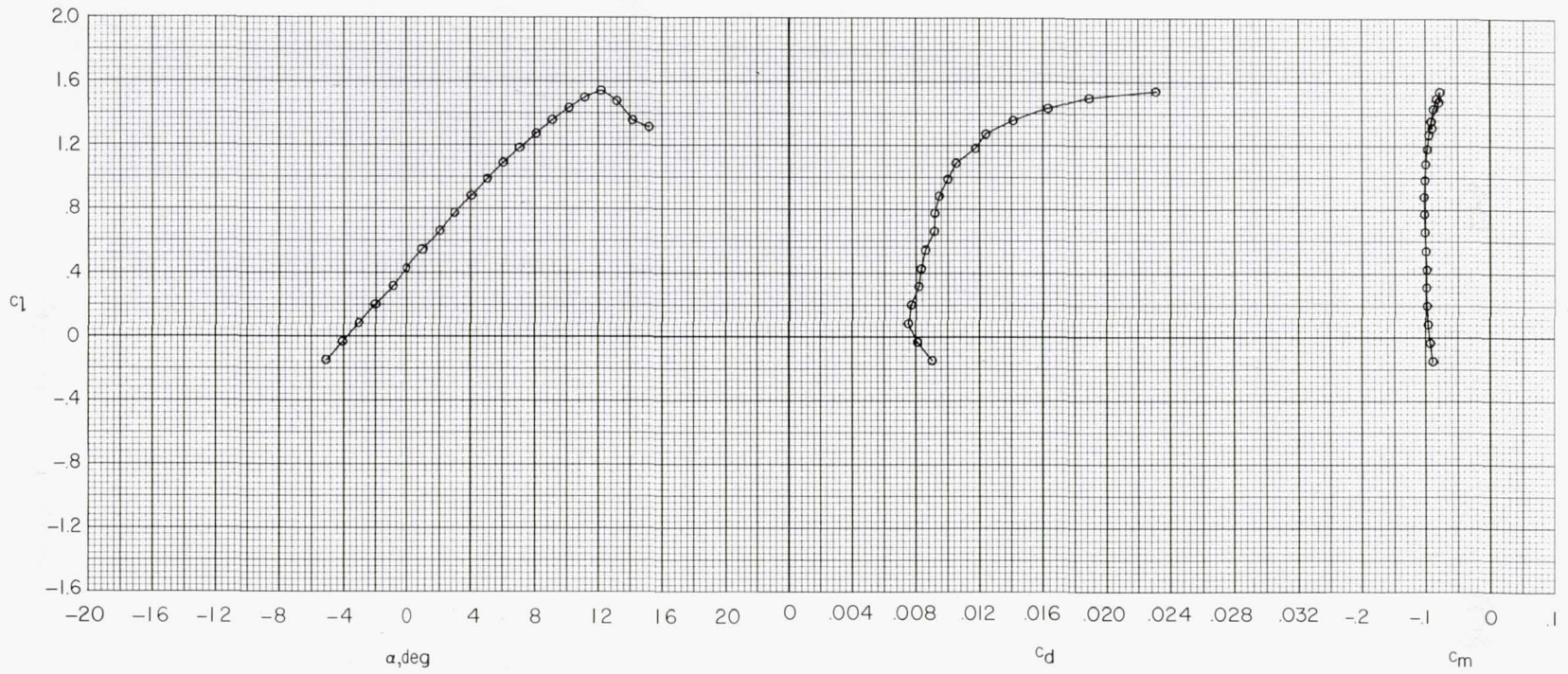
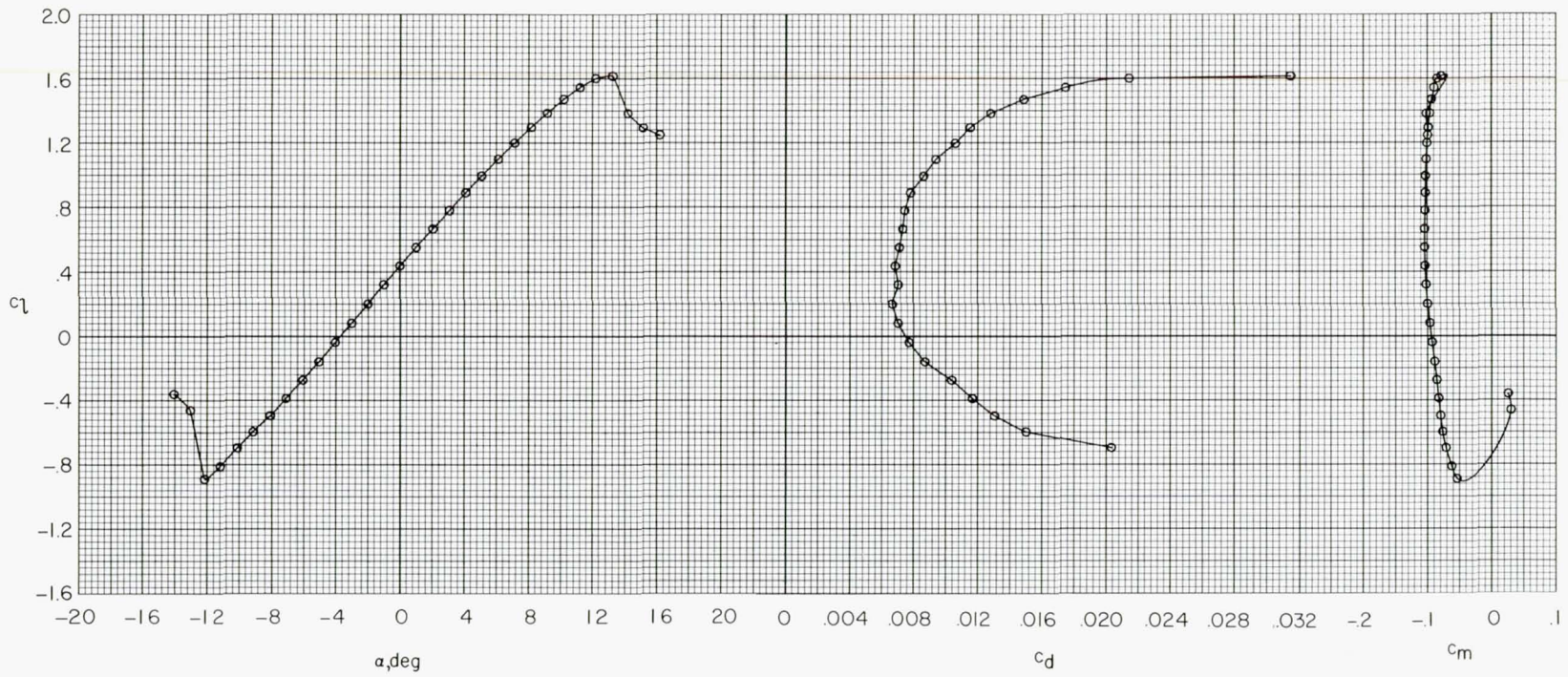


Figure 10.- Effect of Reynolds number on transition location; $M = 0.10$.



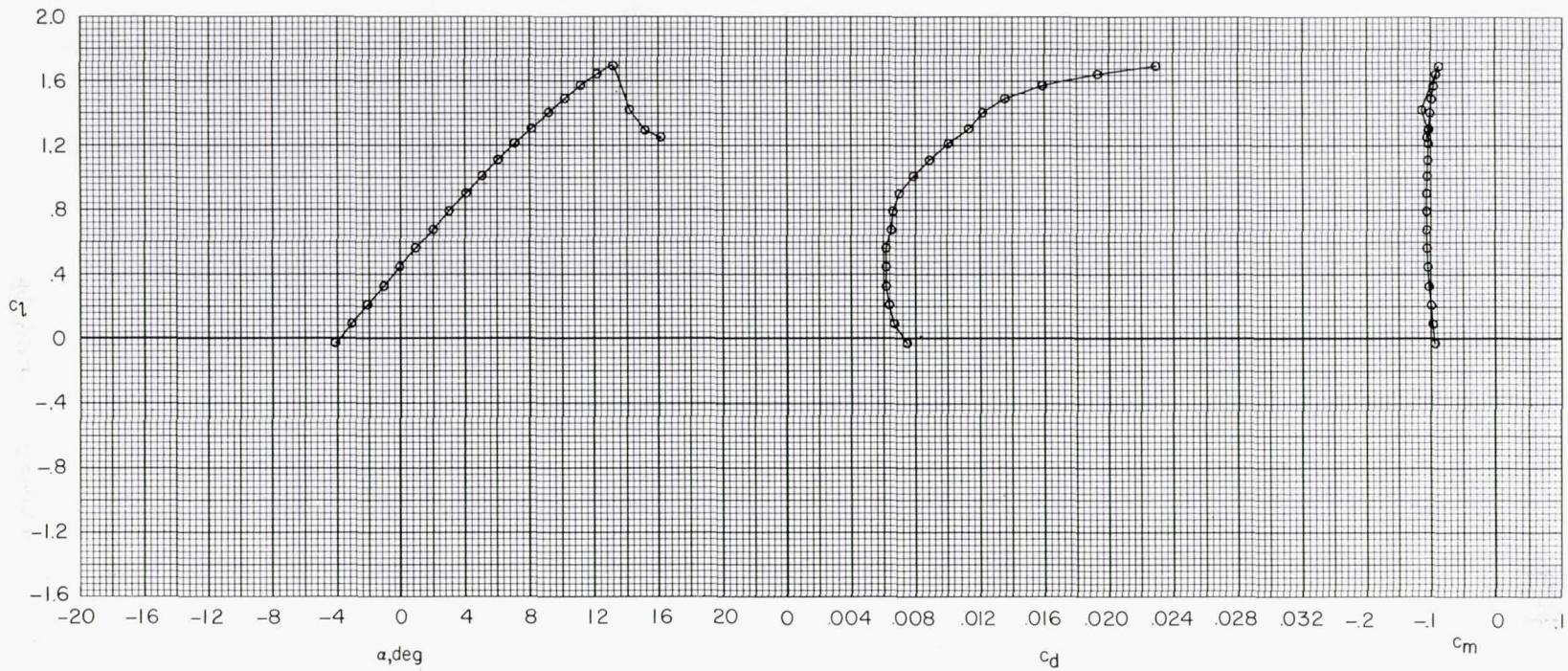
(a) $R = 1.0 \times 10^6$.

Figure 11.- Section characteristics for various Reynolds numbers at $M = 0.10$.



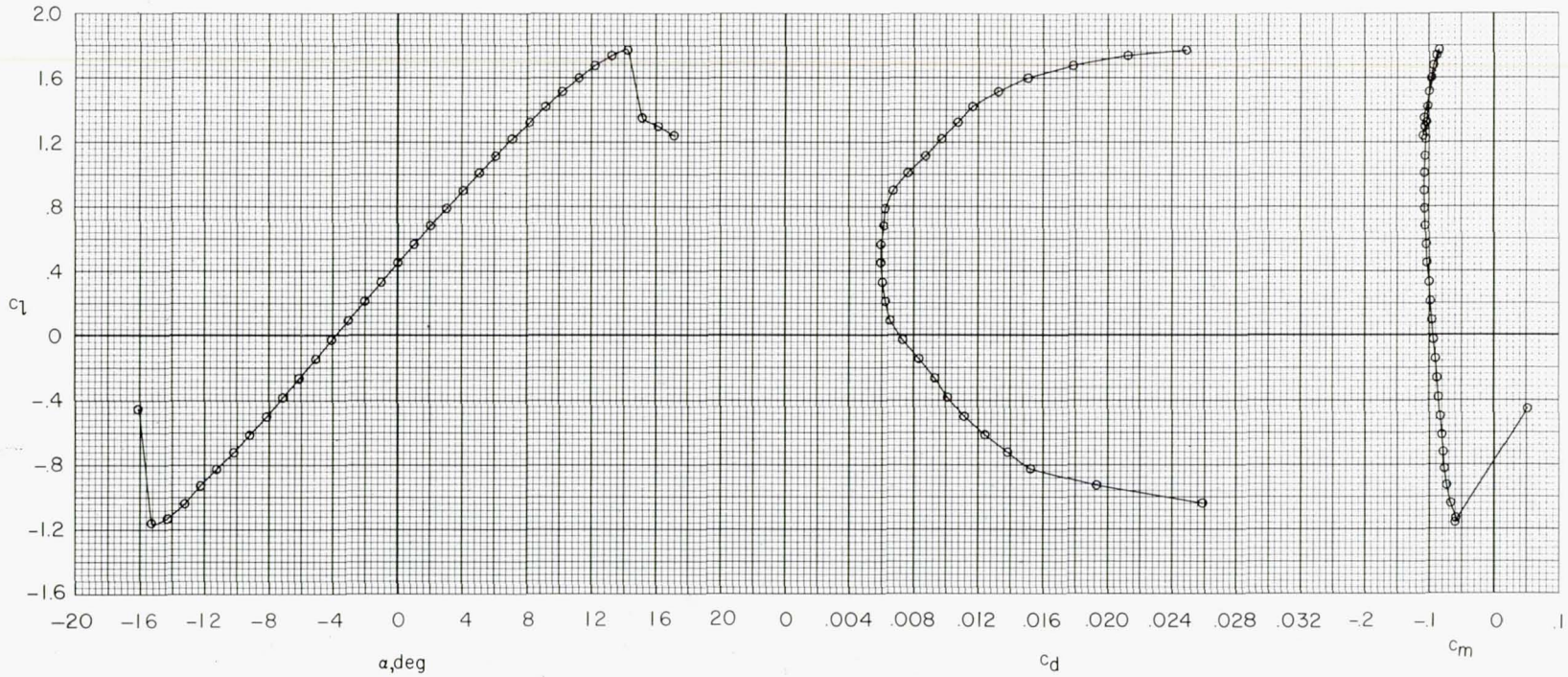
(b) $R = 2.0 \times 10^6$.

Figure 11.- Continued.



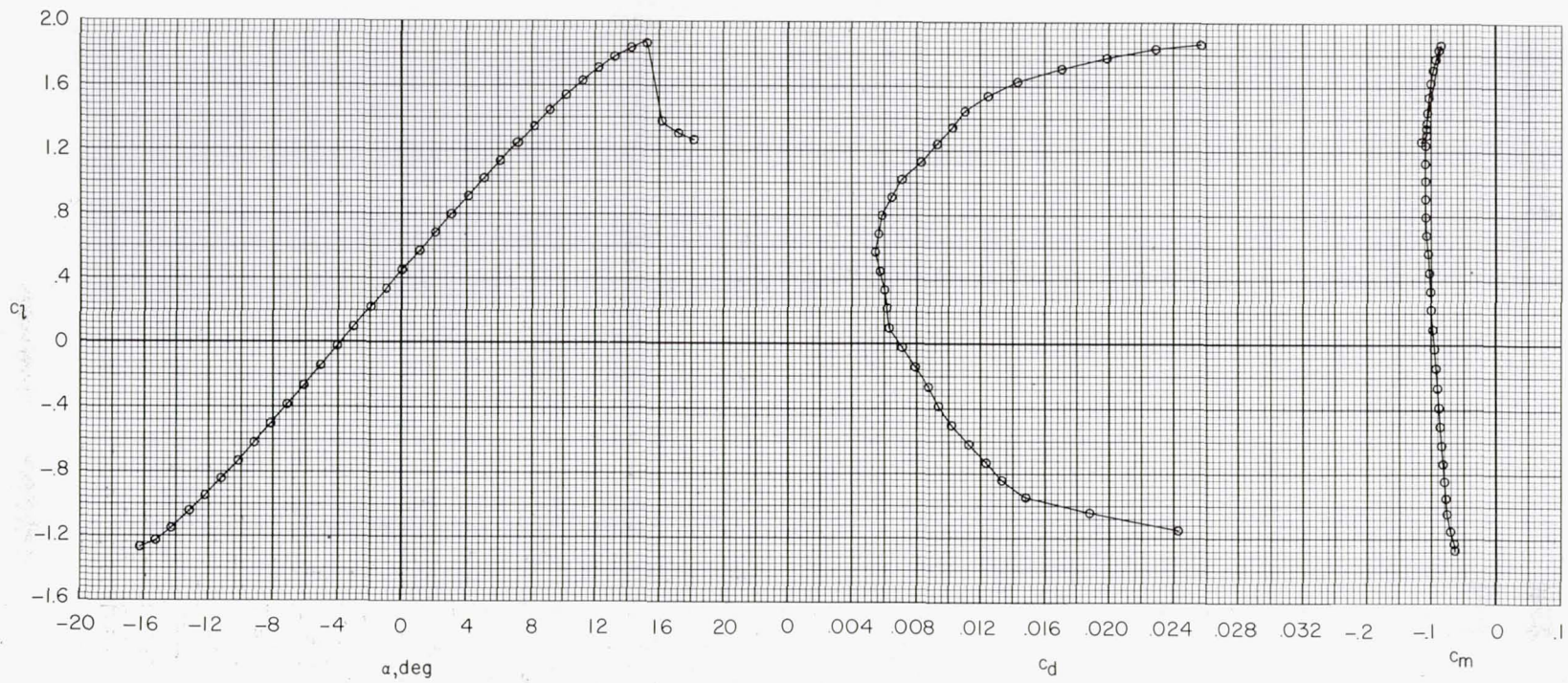
(c) $R = 3.0 \times 10^6$.

Figure 11.- Continued.



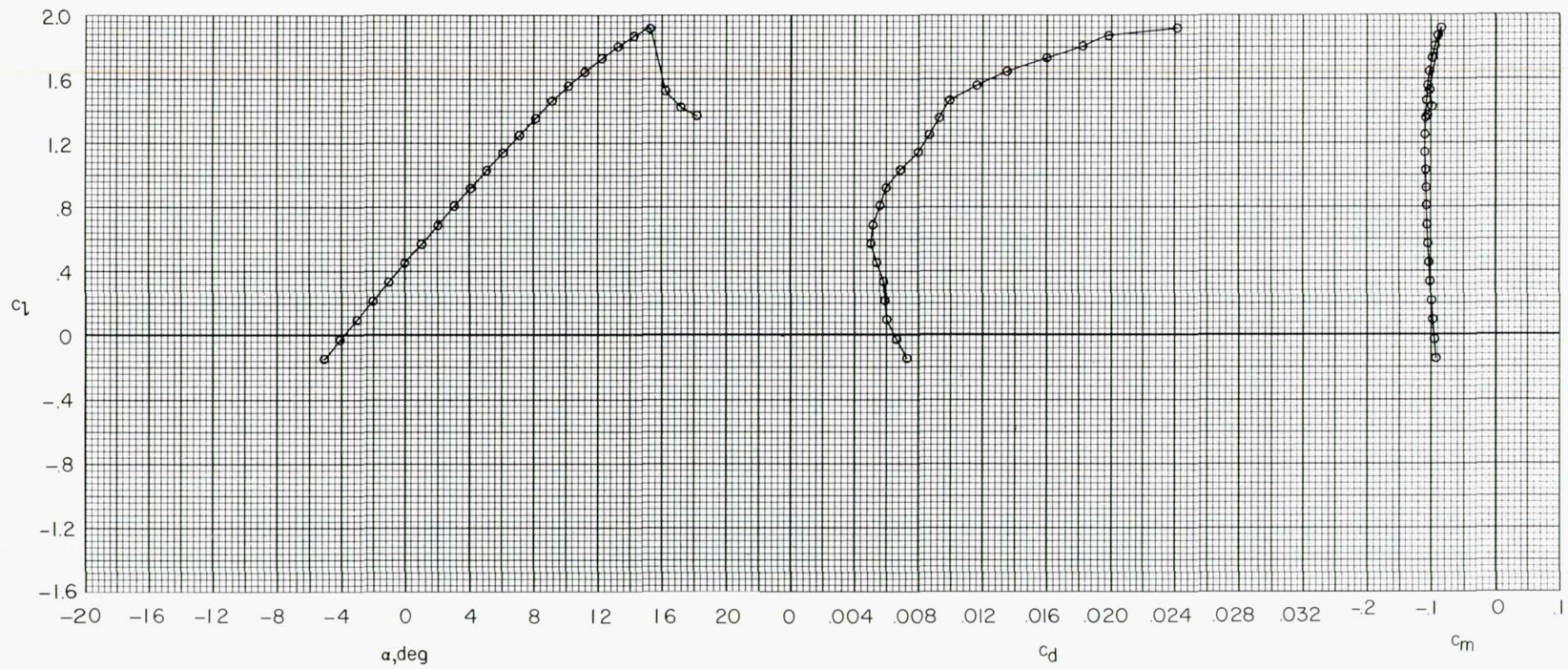
(d) $R = 4.0 \times 10^6$.

Figure 11.- Continued.



(e) $R = 6.0 \times 10^6$.

Figure 11.- Continued.



(f) $R = 9.0 \times 10^6$.

Figure 11.- Concluded.

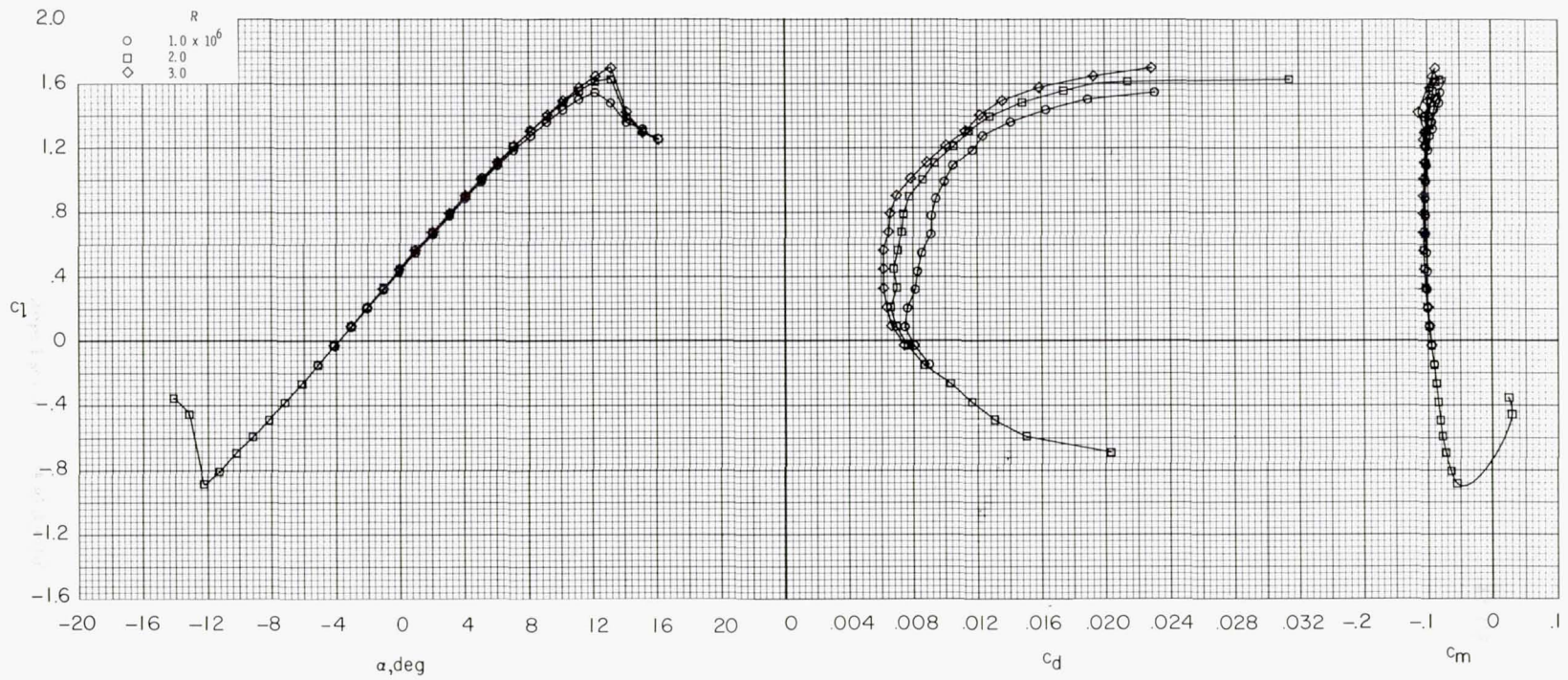


Figure 12.- Effects of Reynolds number on section characteristics at $M = 0.10$.

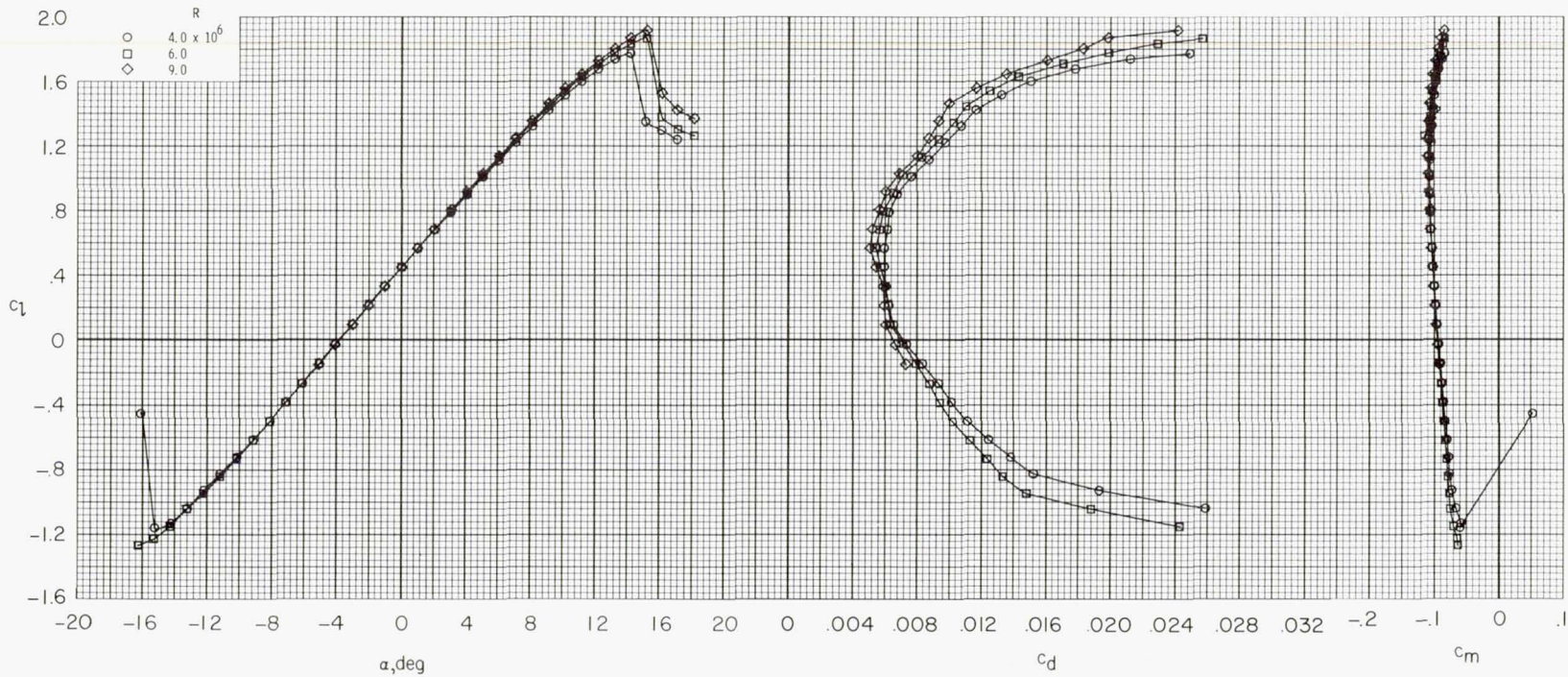


Figure 12.- Concluded.

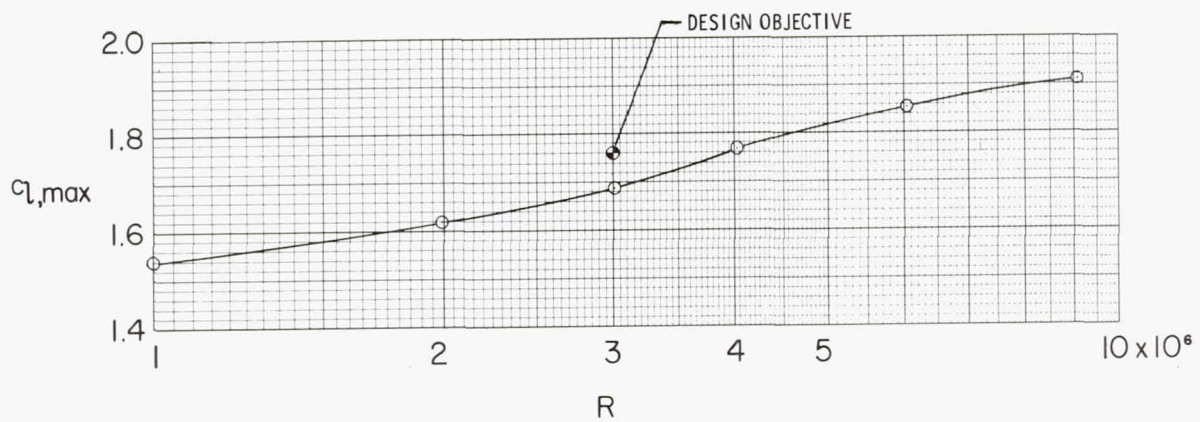


Figure 13.- Effect of Reynolds number on maximum lift coefficient at $M = 0.10$.

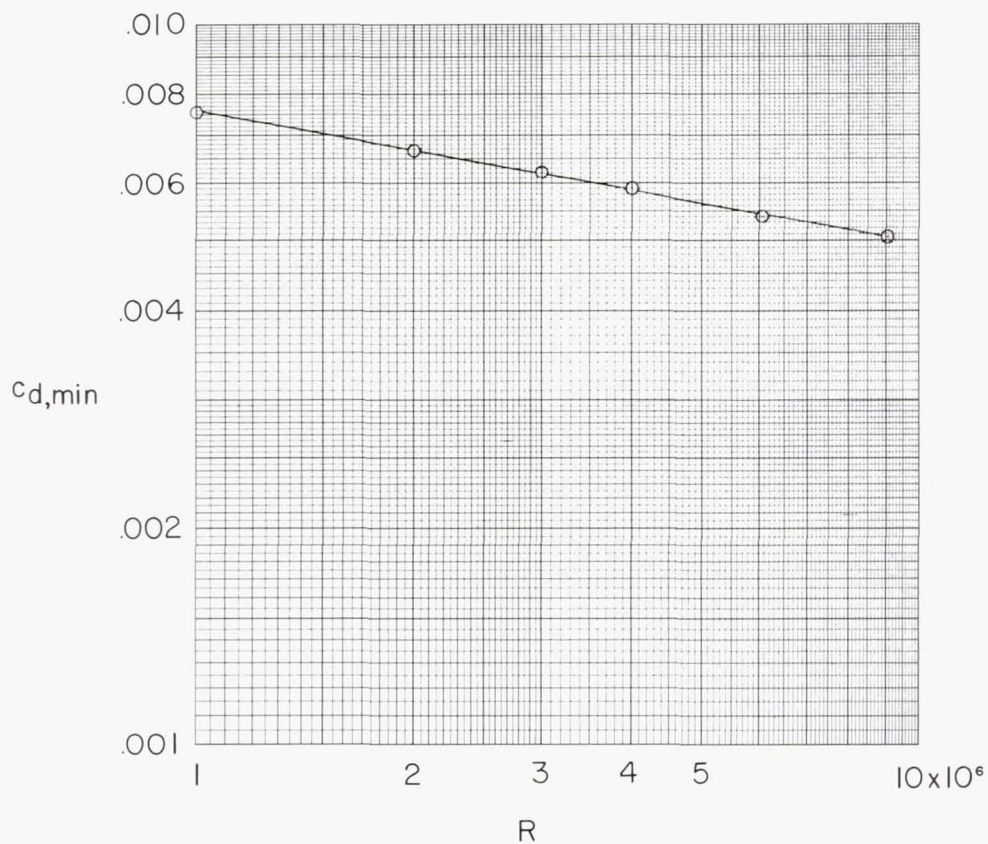


Figure 14.- Effect of Reynolds number on minimum drag coefficient at $M = 0.10$.

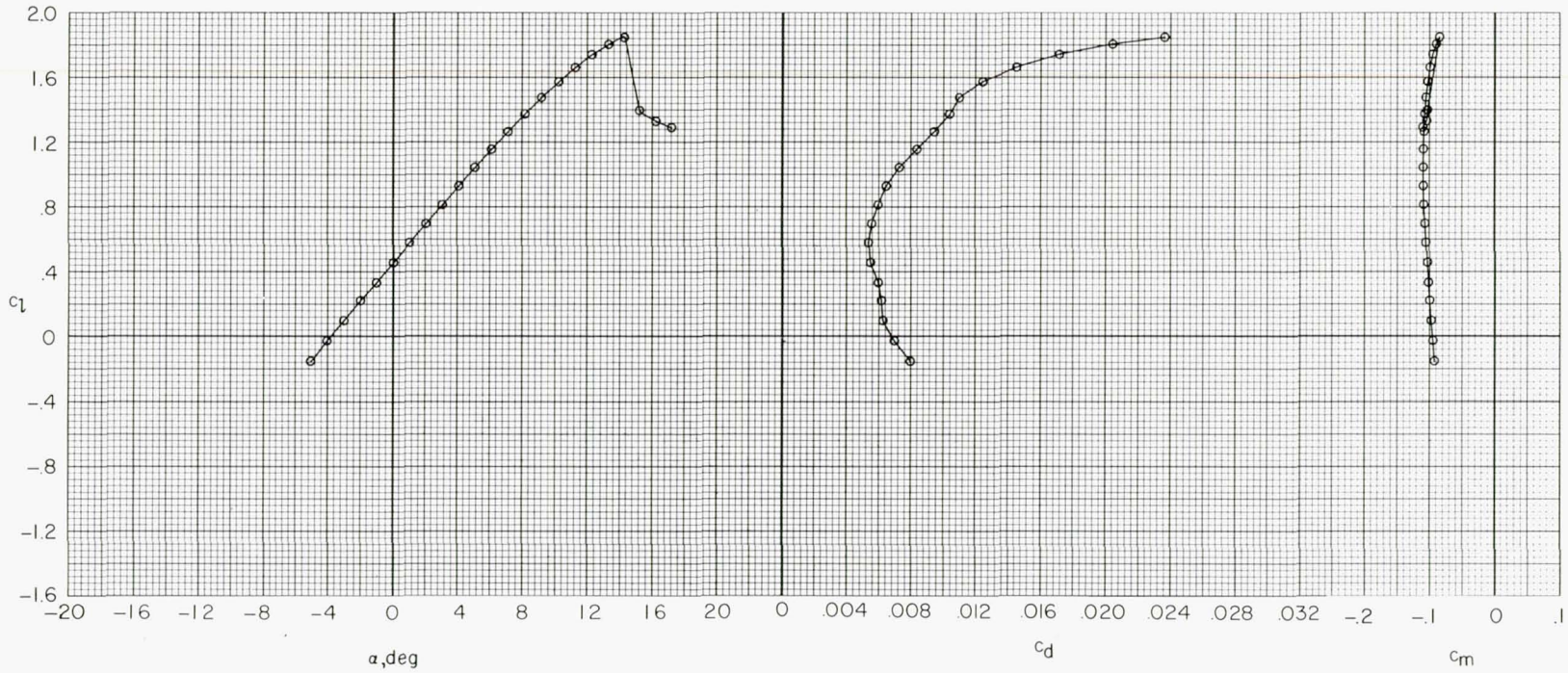
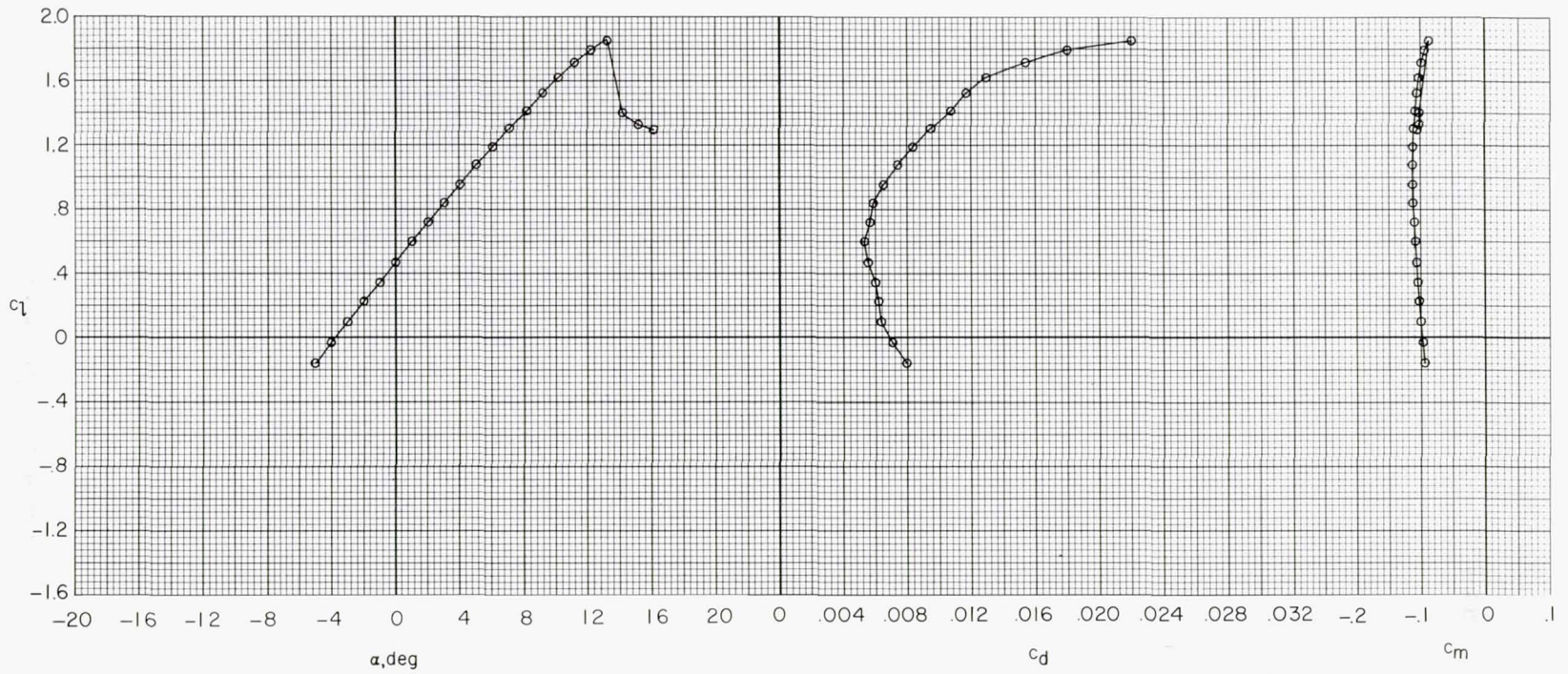
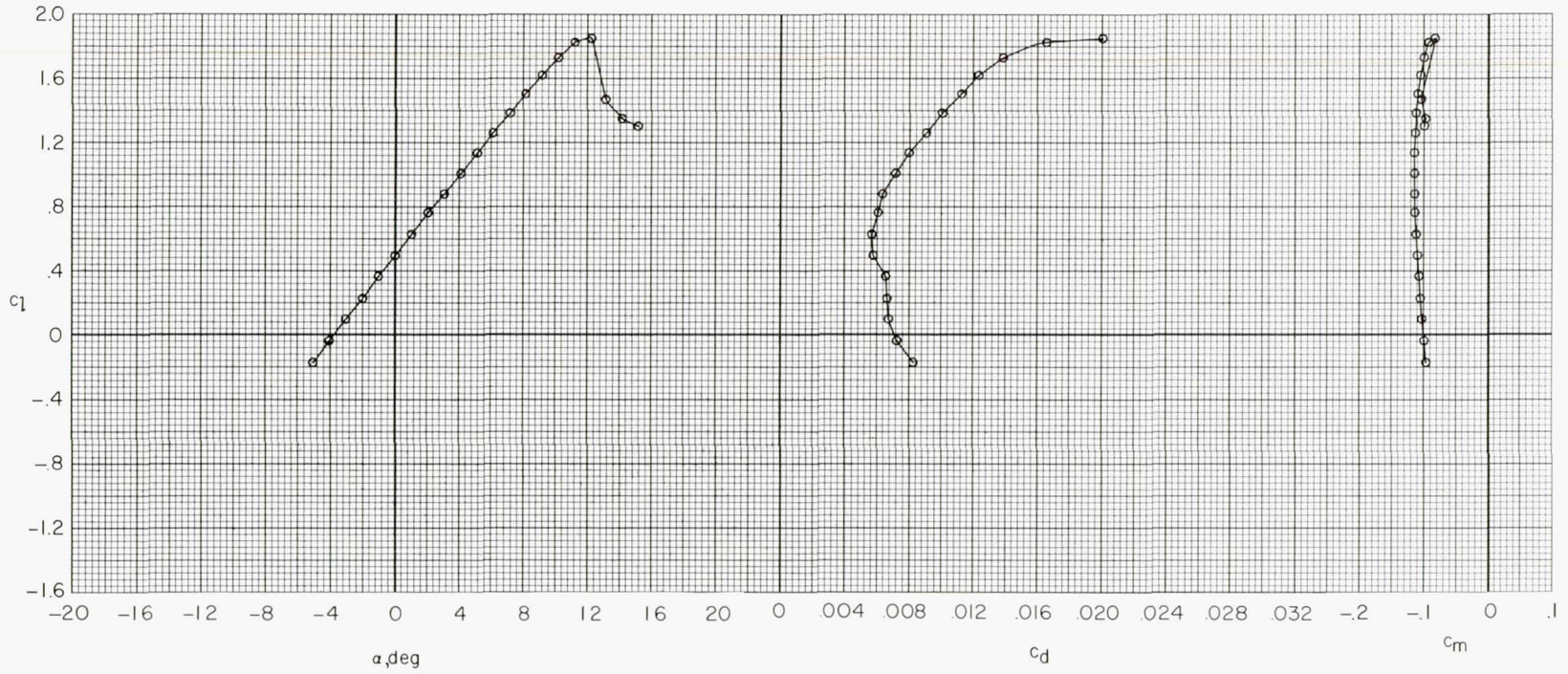
(a) $M = 0.20$.

Figure 15.- Section characteristics for $R = 6.0 \times 10^6$ at various Mach numbers.



(b) $M = 0.30$.

Figure 15.- Continued.



(c) $M = 0.40$.

Figure 15.- Concluded.

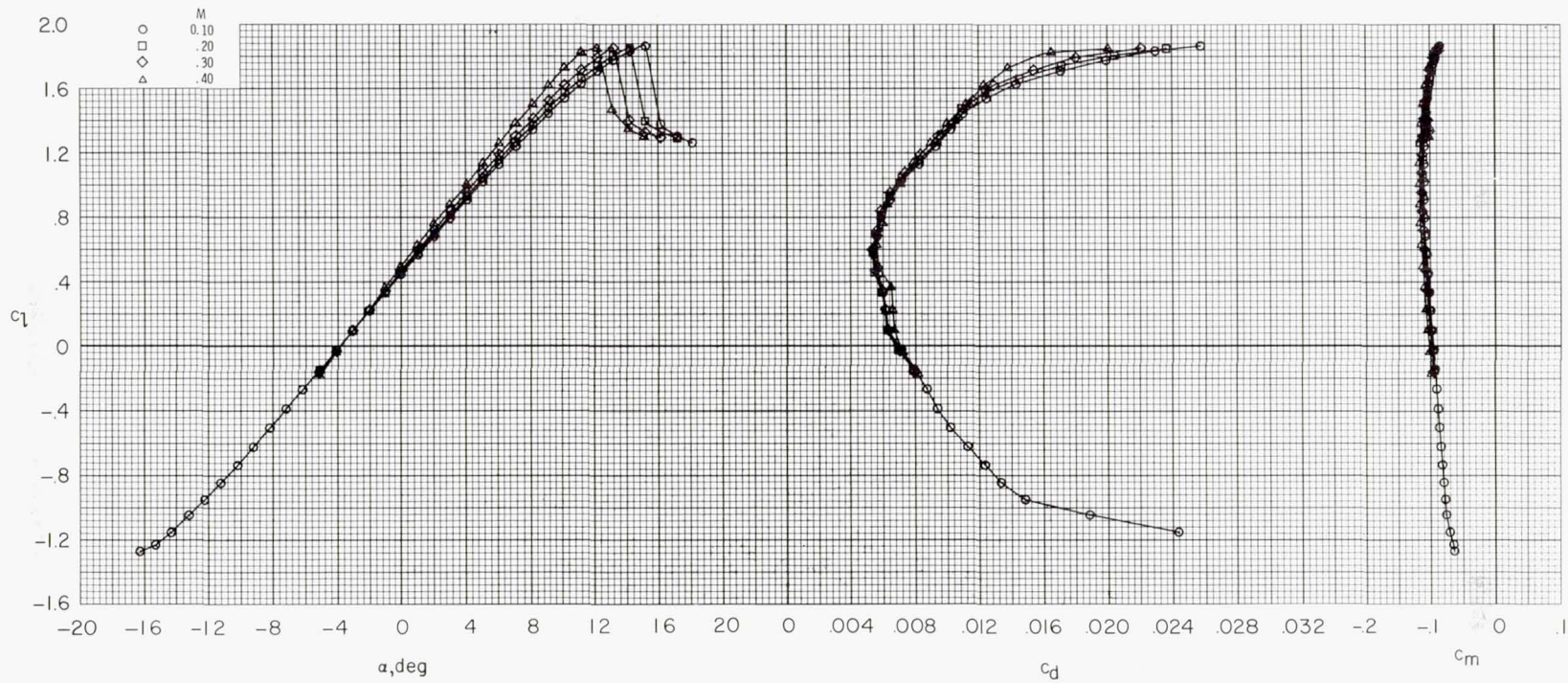


Figure 16.- Effects of Mach number on section characteristics for $R = 6.0 \times 10^6$.

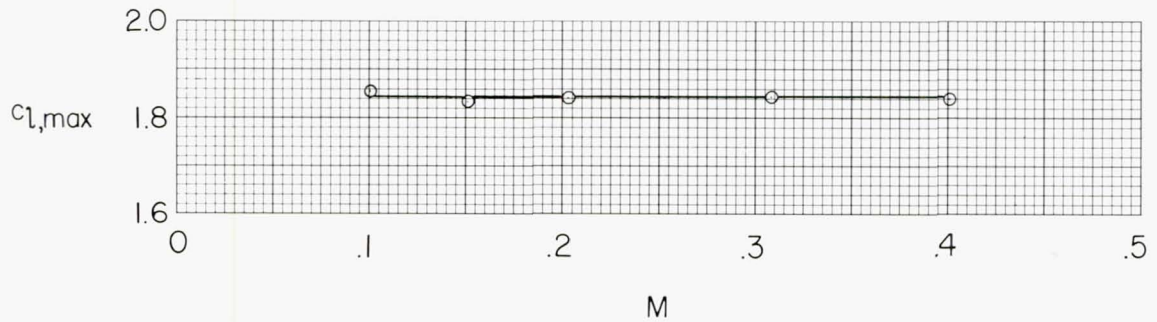


Figure 17.- Effect of Mach number on maximum lift coefficient for $R = 6.0 \times 10^6$.

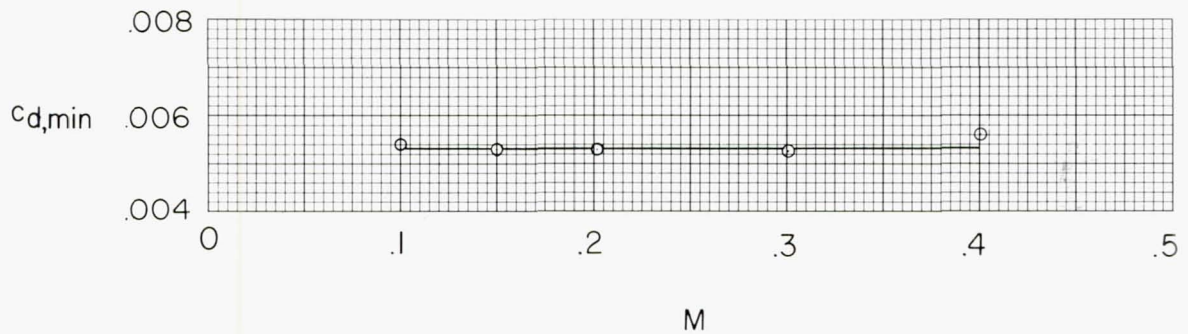
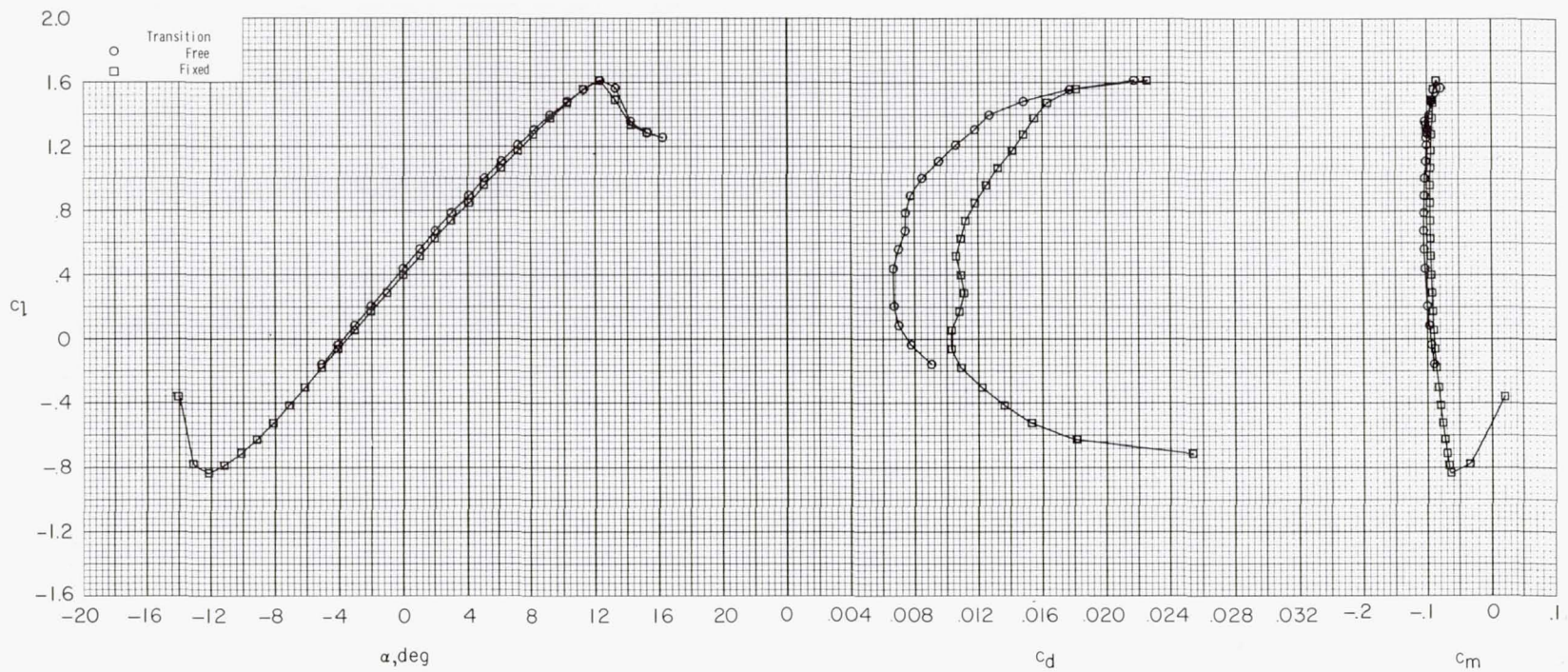
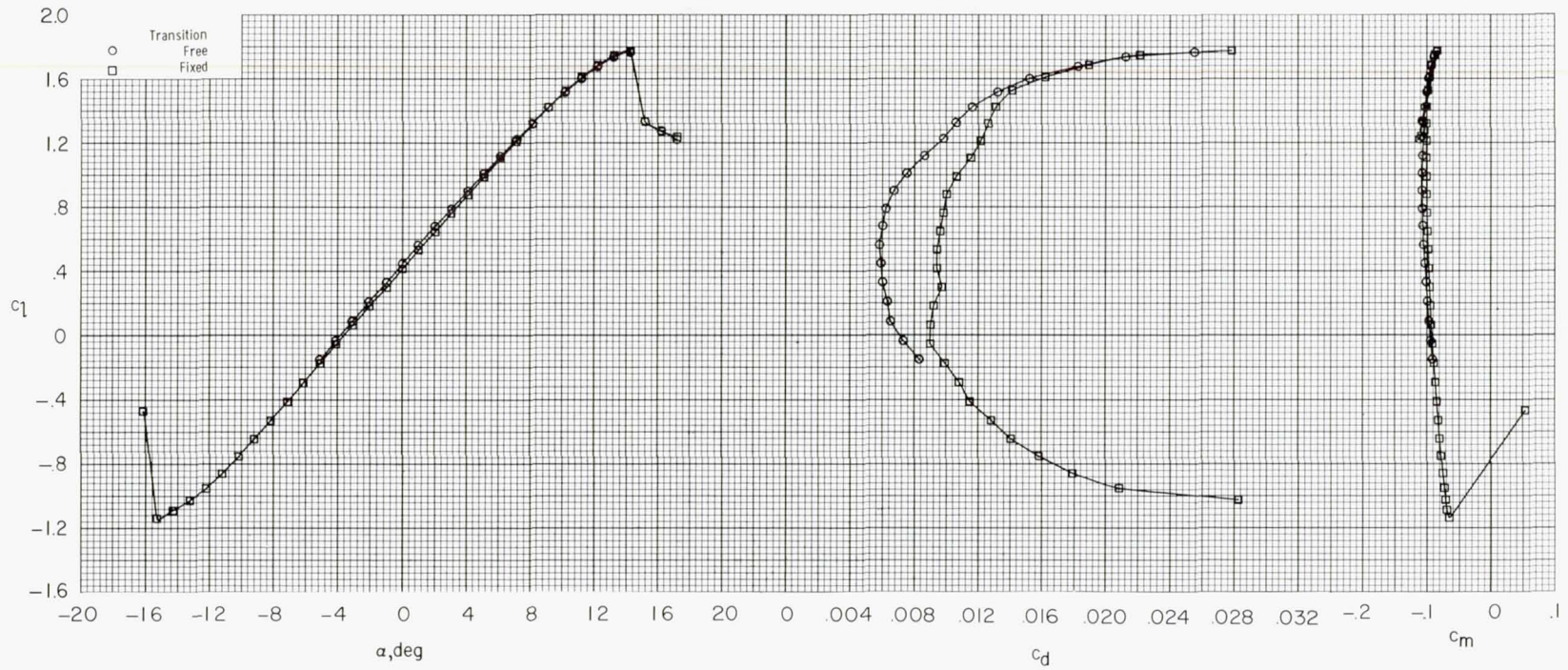


Figure 18.- Effect of Mach number on minimum drag coefficient for $R = 6.0 \times 10^6$.



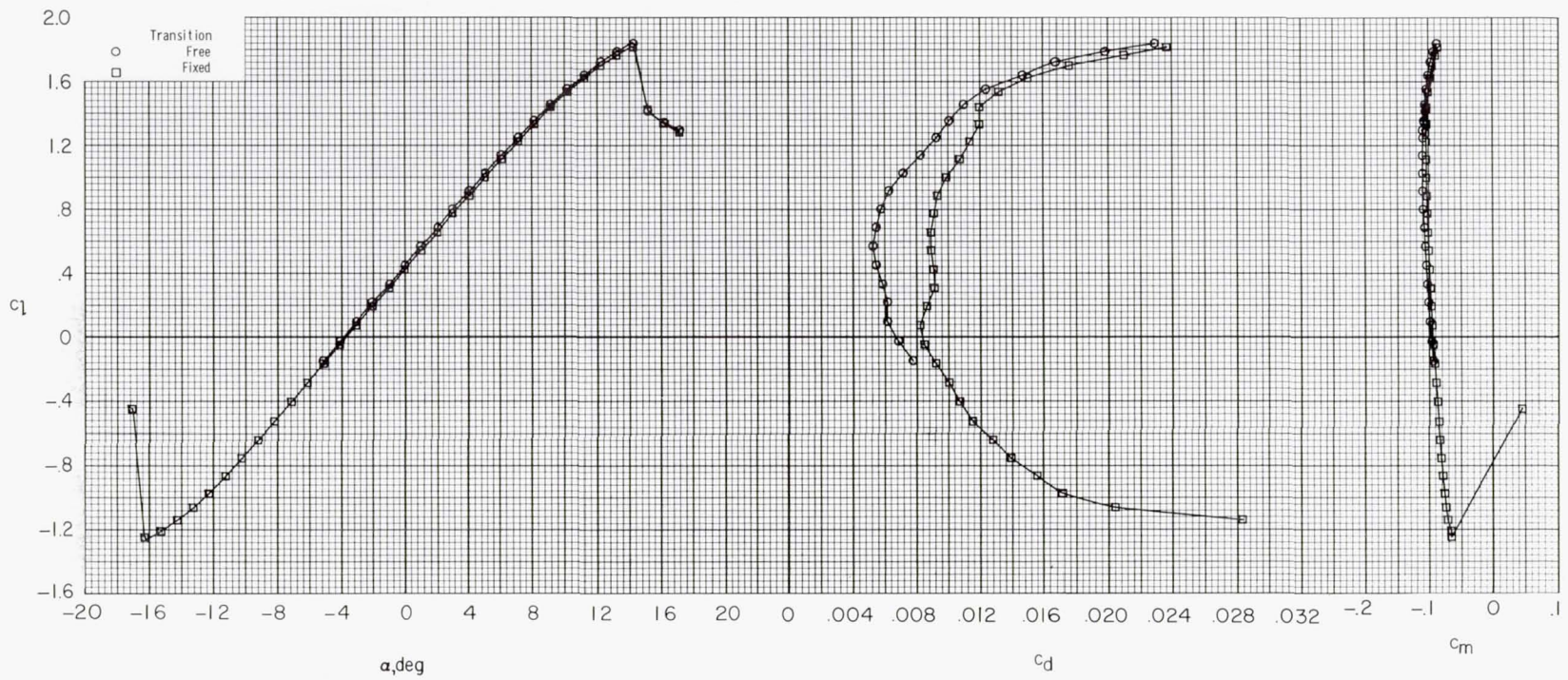
(a) $R = 2.0 \times 10^6$.

Figure 19.- Effect of roughness on section characteristics for various Reynolds numbers at $M = 0.15$.



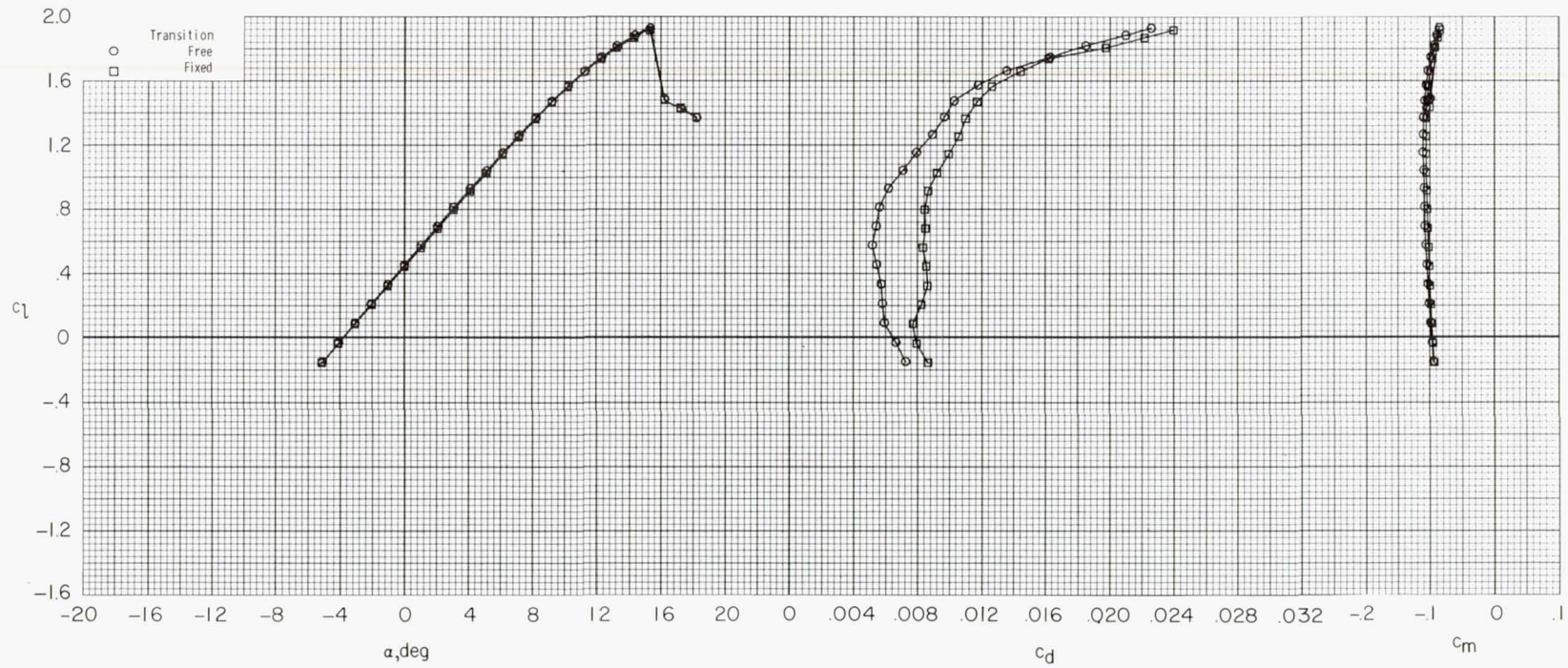
(b) $R = 4.0 \times 10^6$.

Figure 19.- Continued.



(c) $R = 6.0 \times 10^6$.

Figure 19.- Continued.



(d) $R = 9.0 \times 10^6$.

Figure 19.- Concluded.

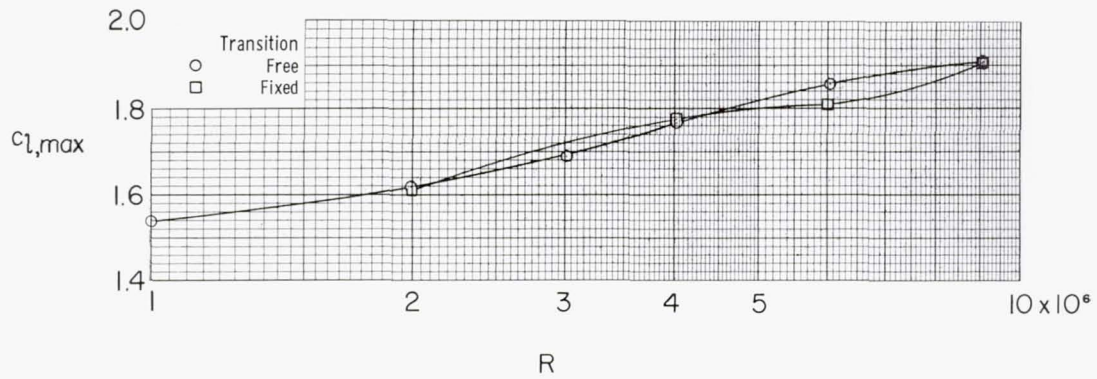


Figure 20.- Effect of roughness on maximum lift coefficient for various Reynolds numbers.

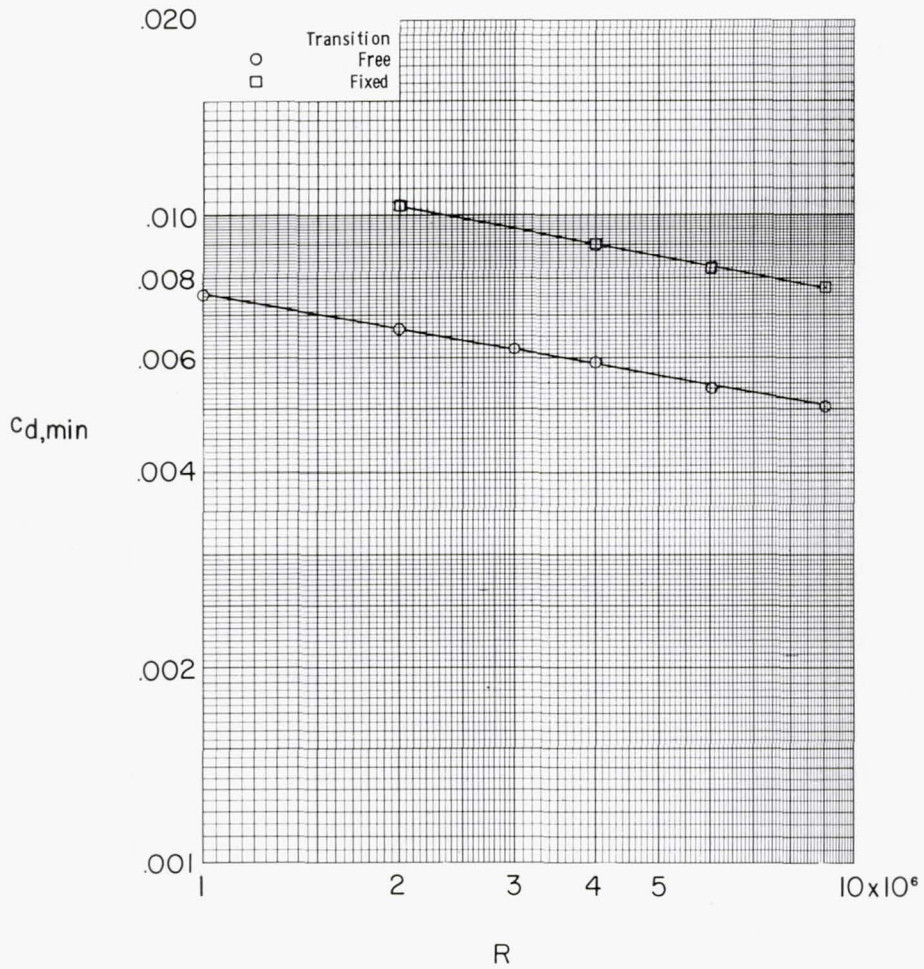
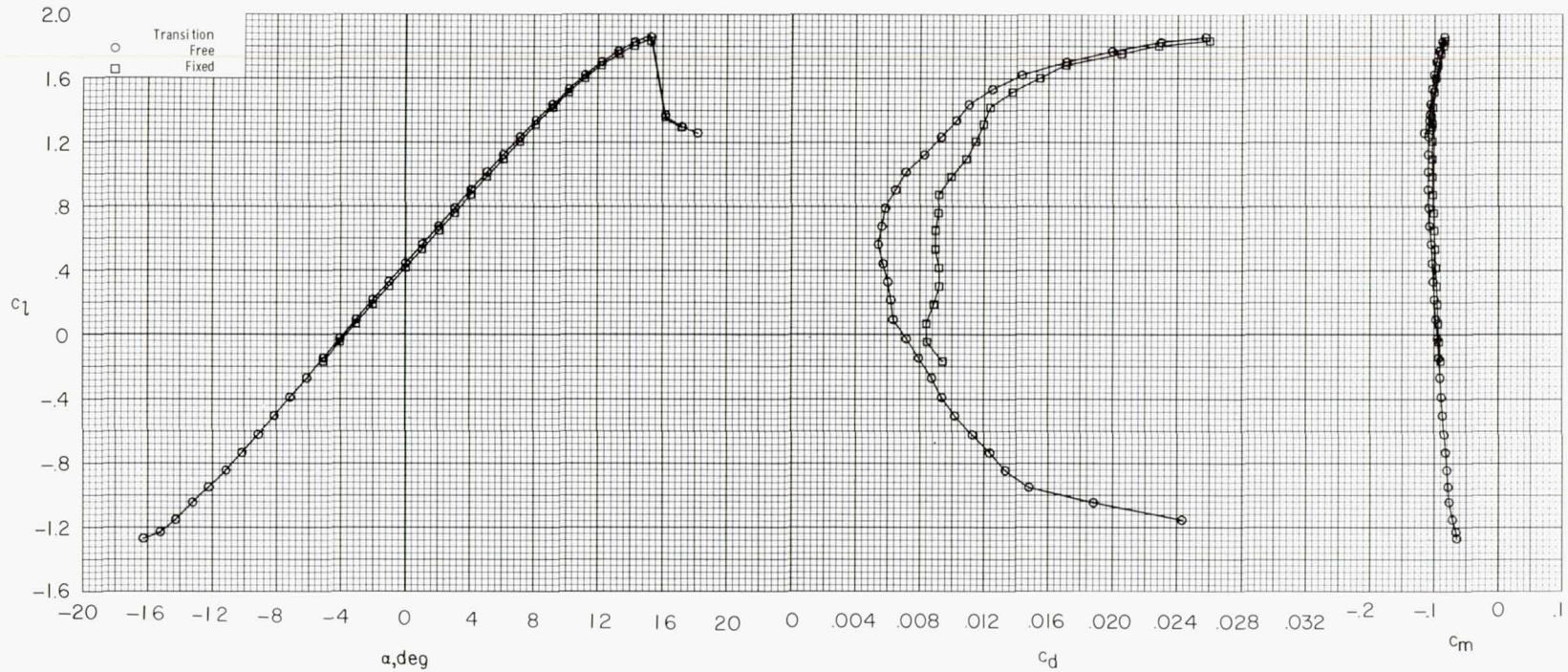
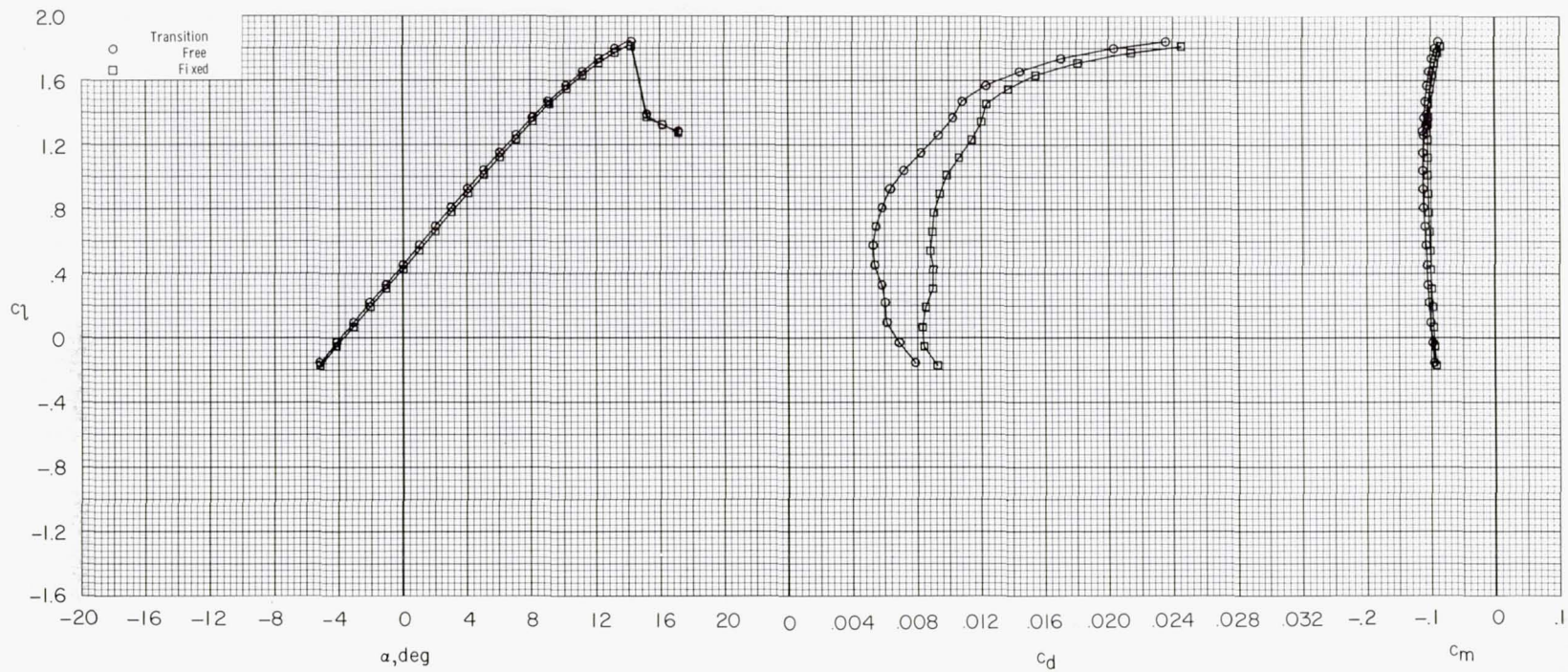


Figure 21.- Effect of roughness on minimum drag coefficient for various Reynolds numbers.



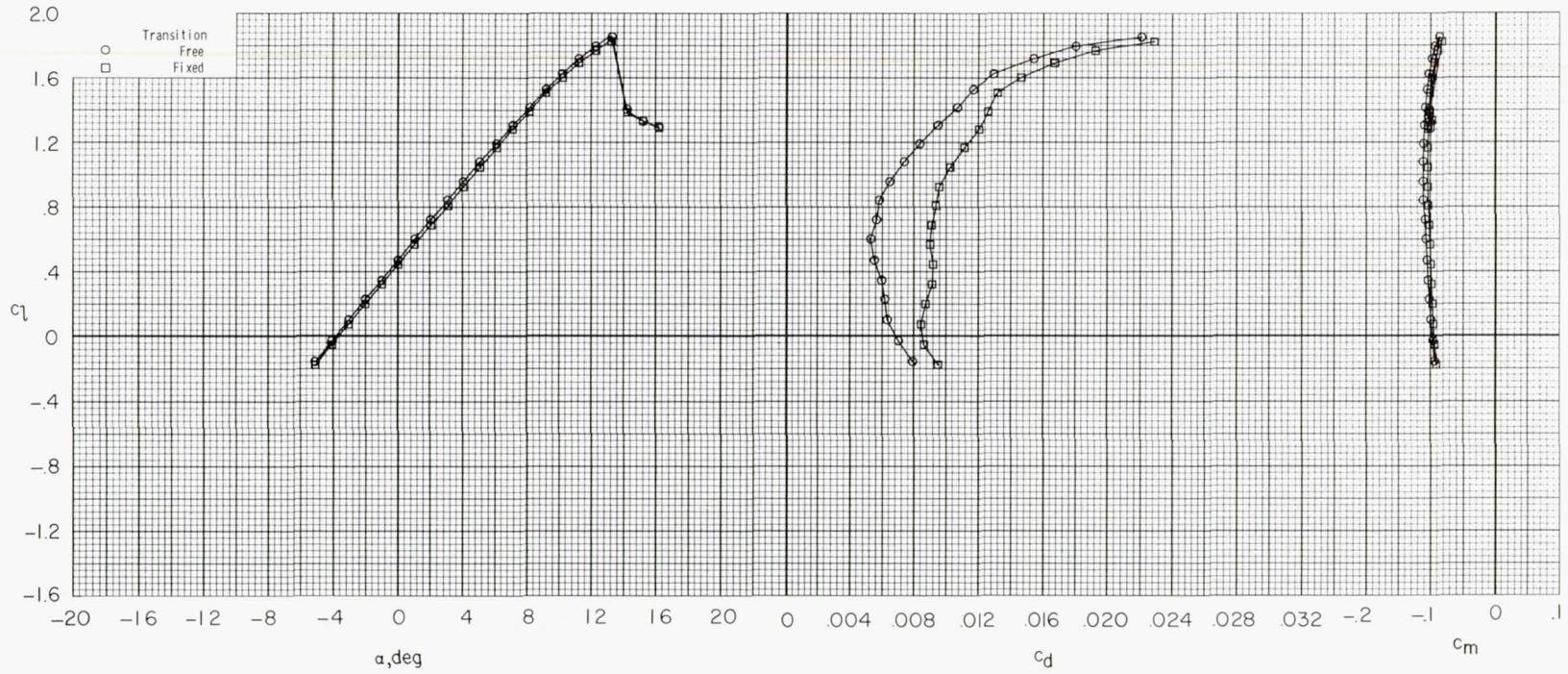
(a) $M = 0.10$.

Figure 22.- Effect of roughness on section characteristics for $R = 6.0 \times 10^6$ at various Mach numbers.



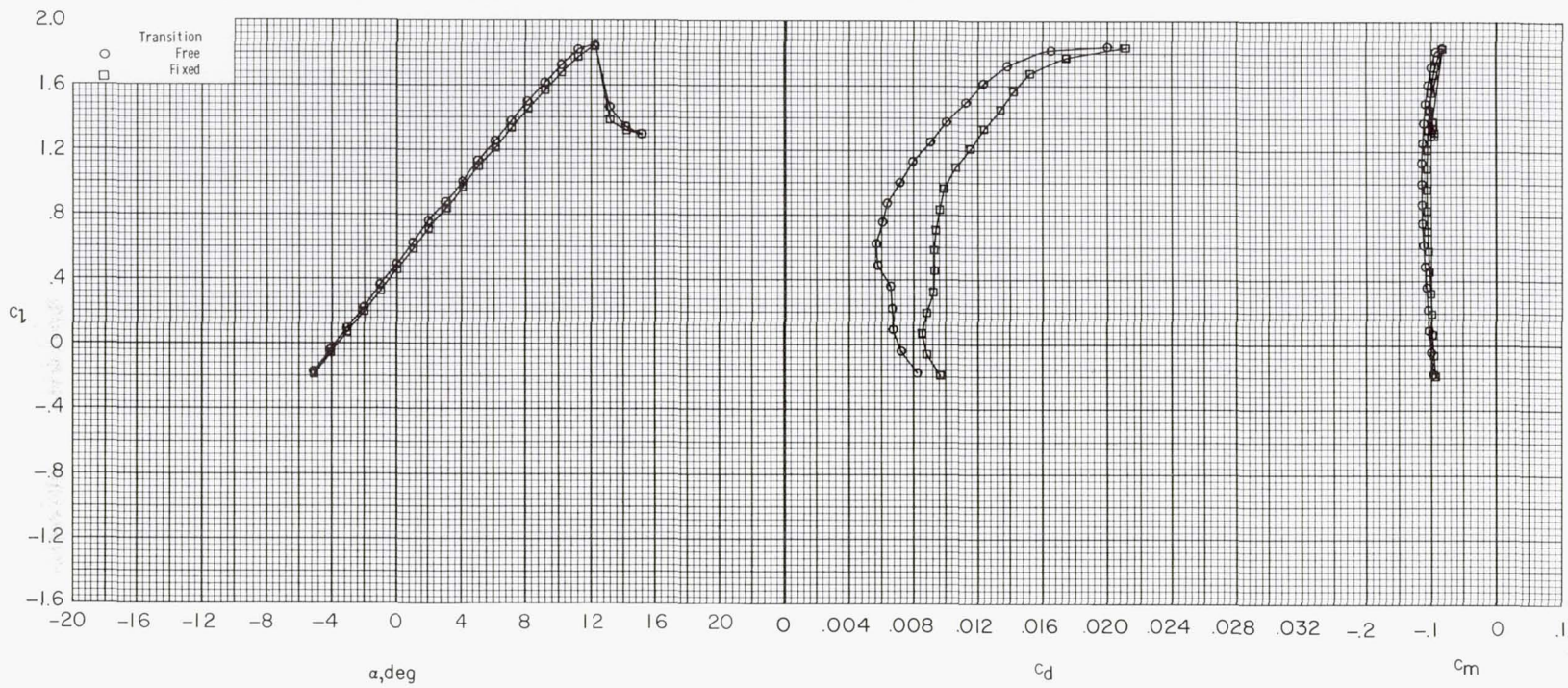
(b) $M = 0.20$.

Figure 22.- Continued.



(c) $M = 0.30$.

Figure 22.- Continued.



(d) $M = 0.40$.

Figure 22.- Concluded.

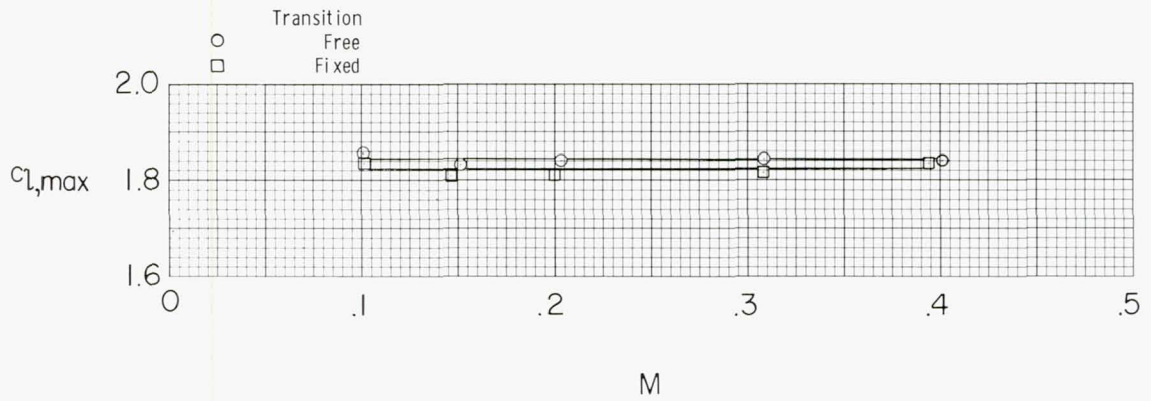


Figure 23.- Effect of roughness on maximum lift coefficient at various Mach numbers.

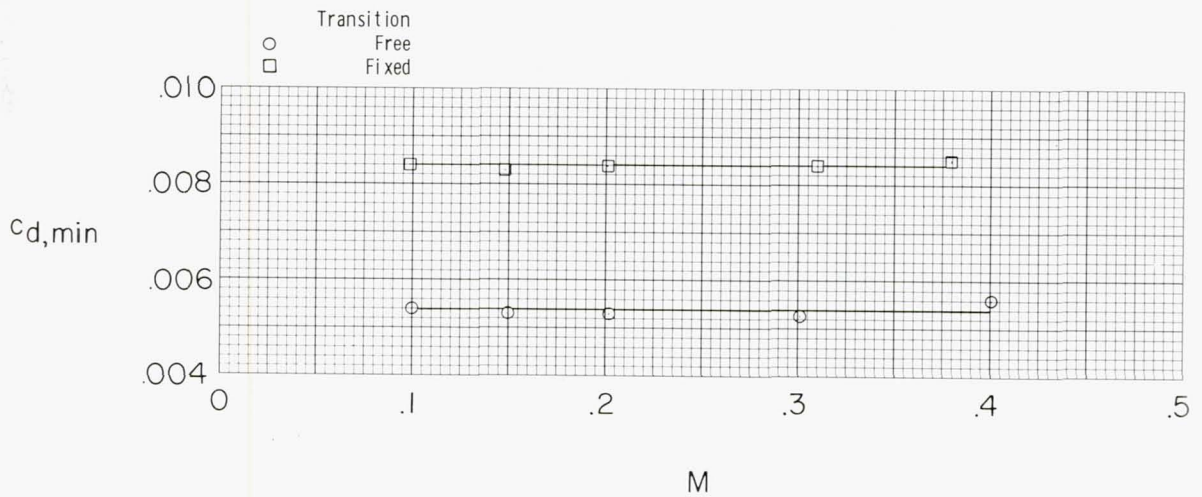
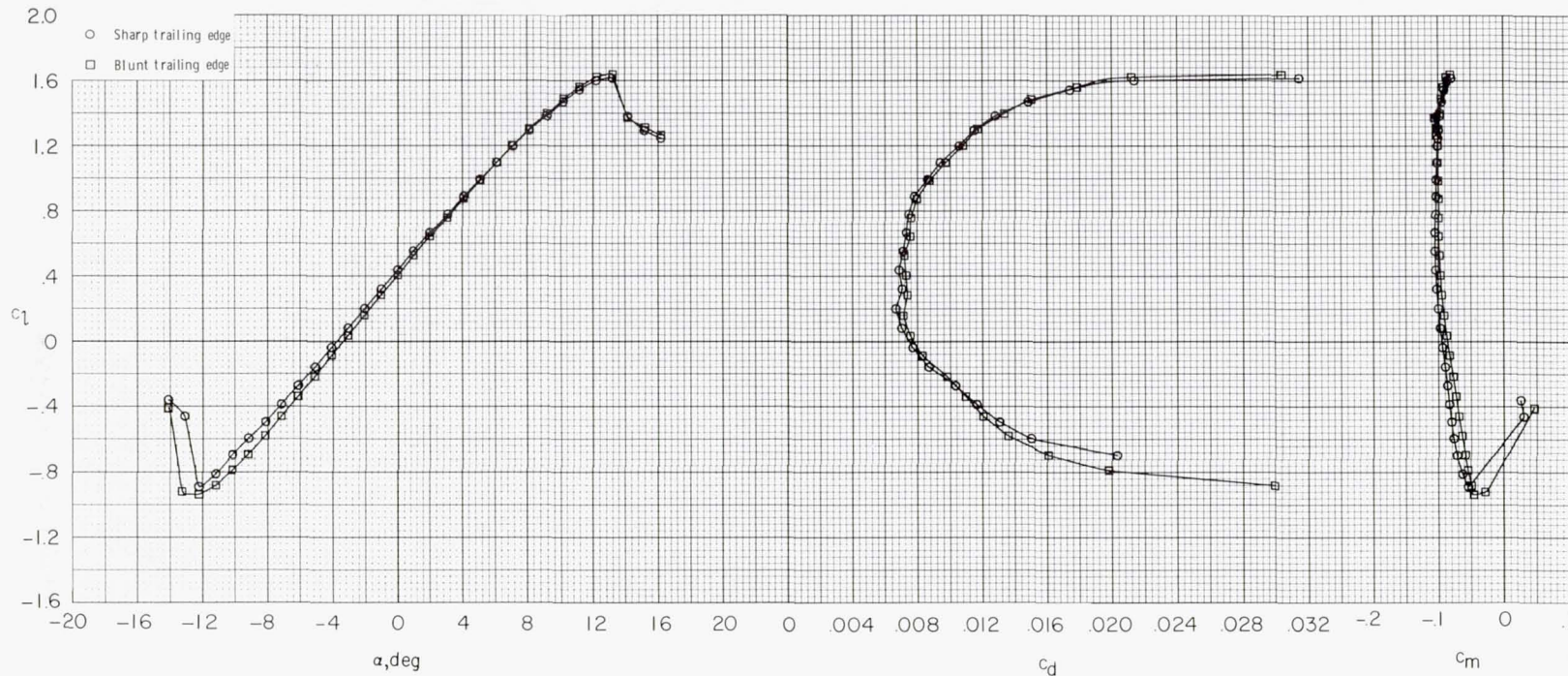
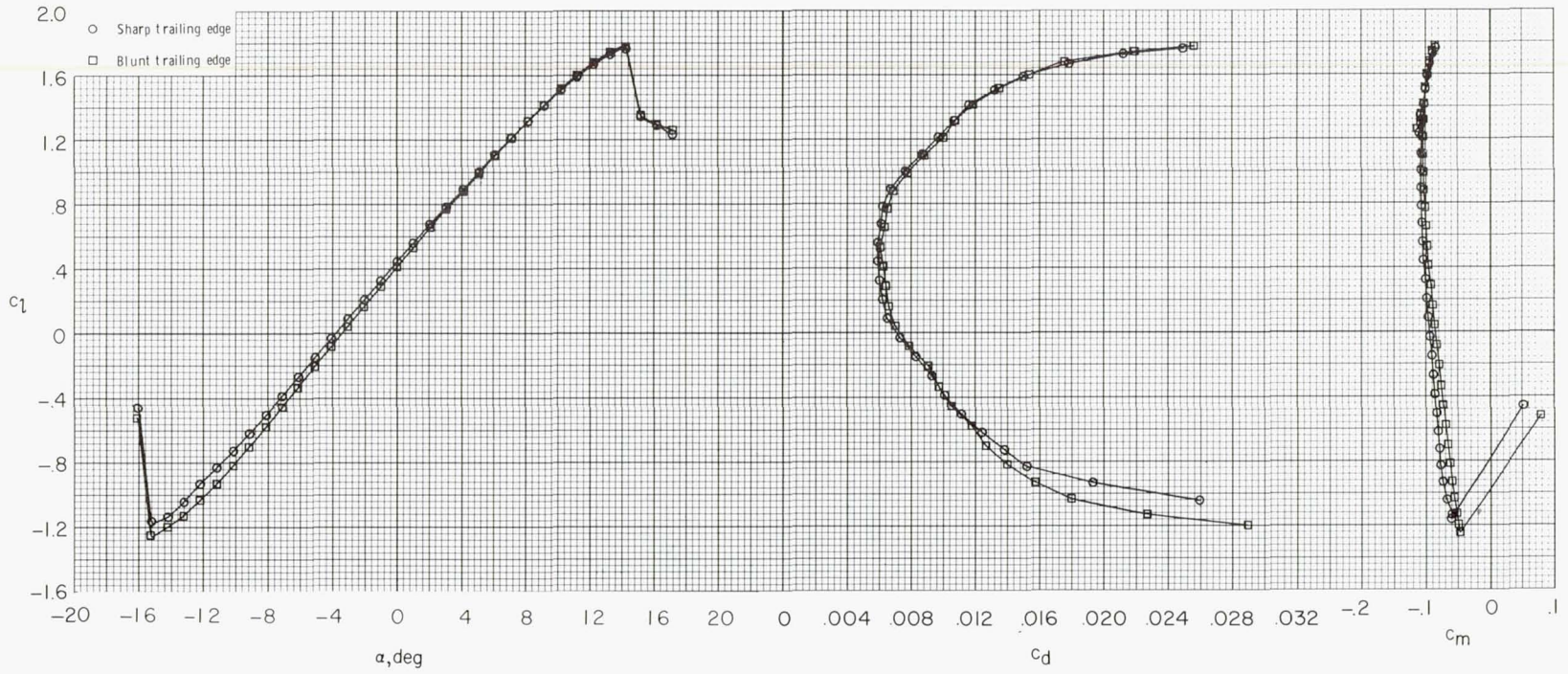


Figure 24.- Effect of roughness on minimum drag coefficient at various Mach numbers.



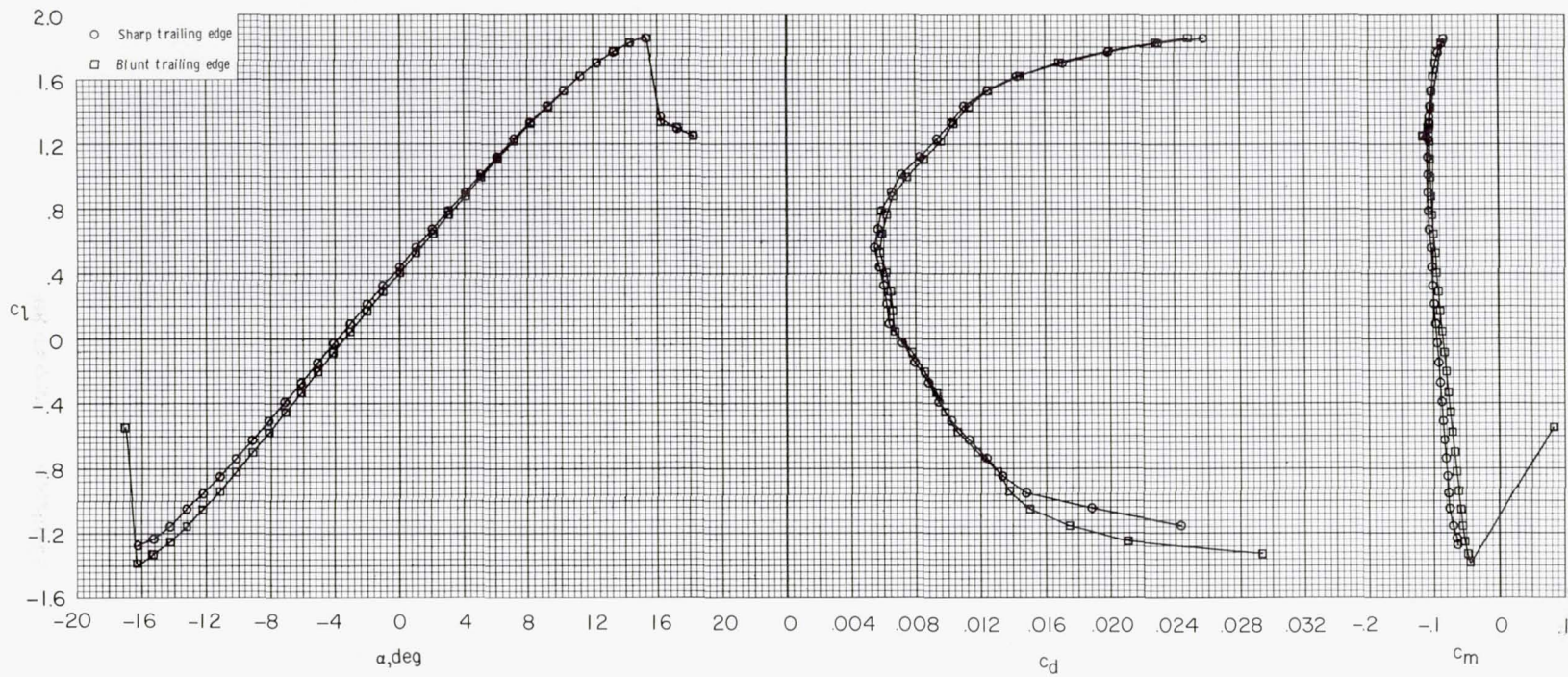
(a) $R = 2.0 \times 10^6$.

Figure 25.- Effect of blunt trailing edge on section characteristics for various Reynolds numbers at $M = 0.10$ with transition free.



(b) $R = 4.0 \times 10^6$.

Figure 25.- Continued.



(c) $R = 6.0 \times 10^6$.

Figure 25.- Concluded.

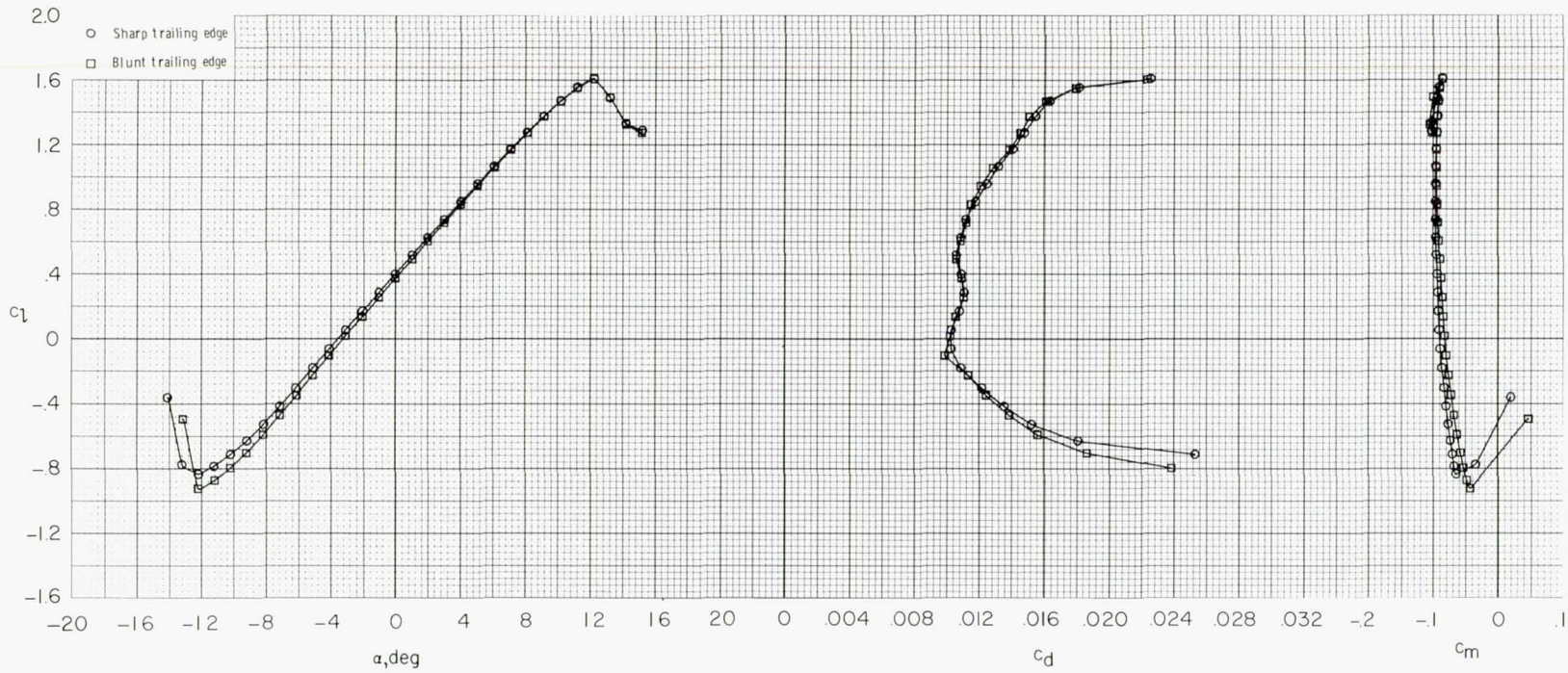


Figure 26.- Effect of blunt trailing edge on section characteristics for $R = 2.0 \times 10^6$ and $M = 0.15$ with transition fixed.

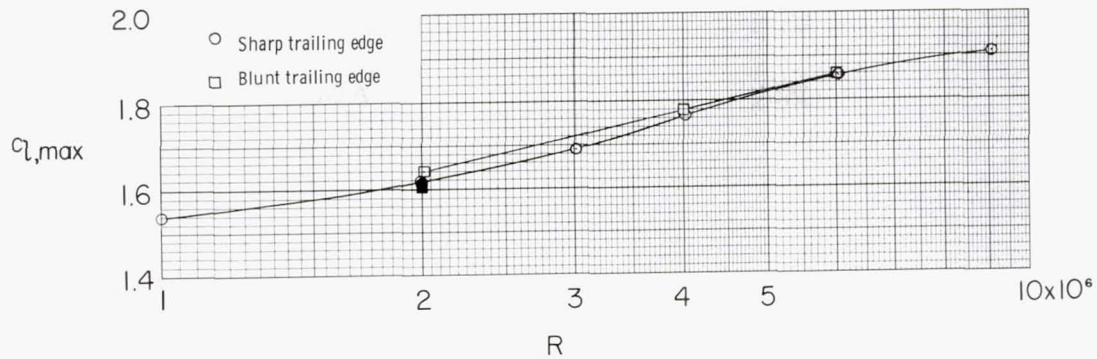


Figure 27.- Effect of blunt trailing edge on maximum lift coefficient for various Reynolds numbers. Open symbols represent data with transition free; solid symbols, data with transition fixed.

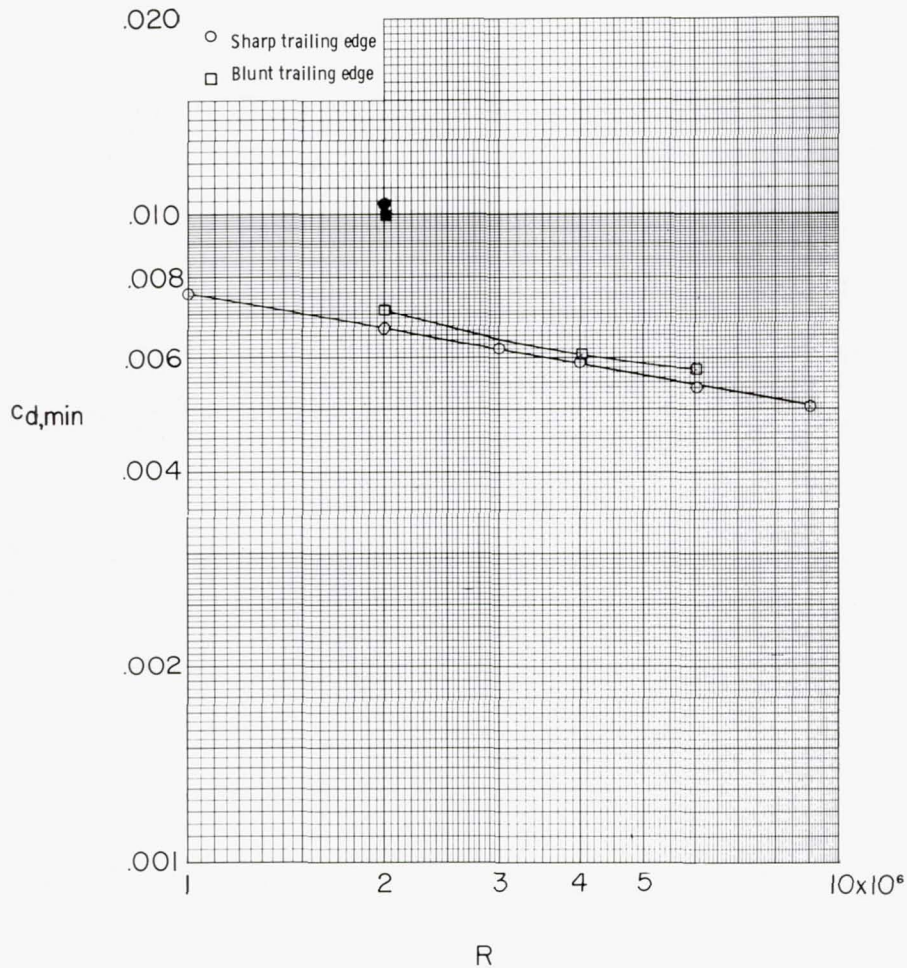
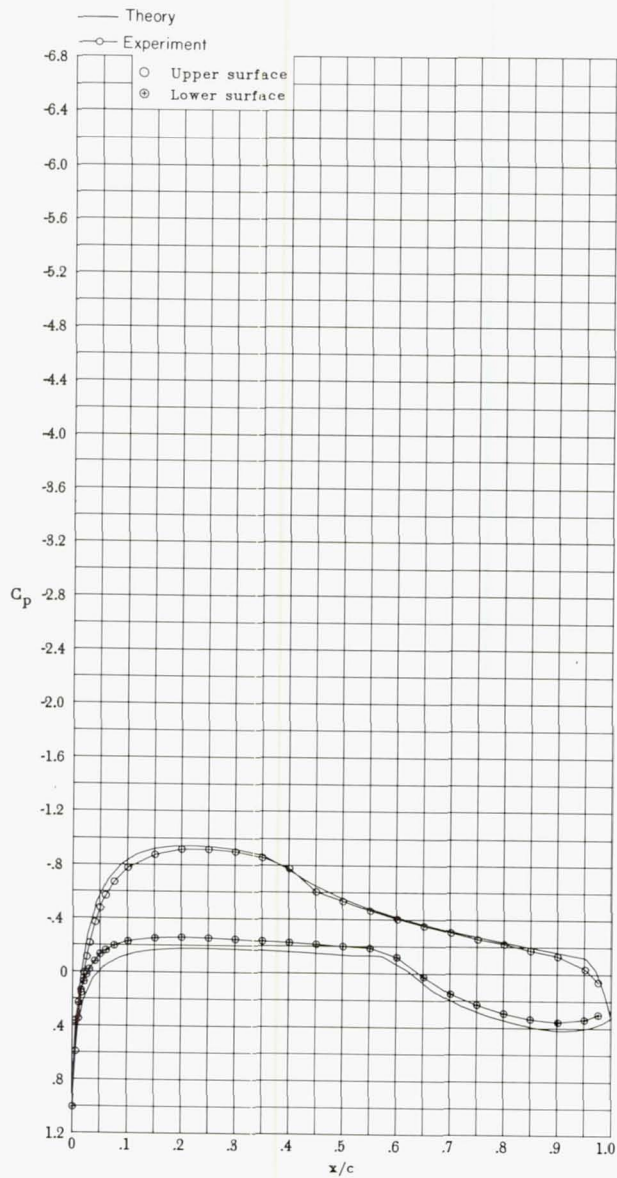
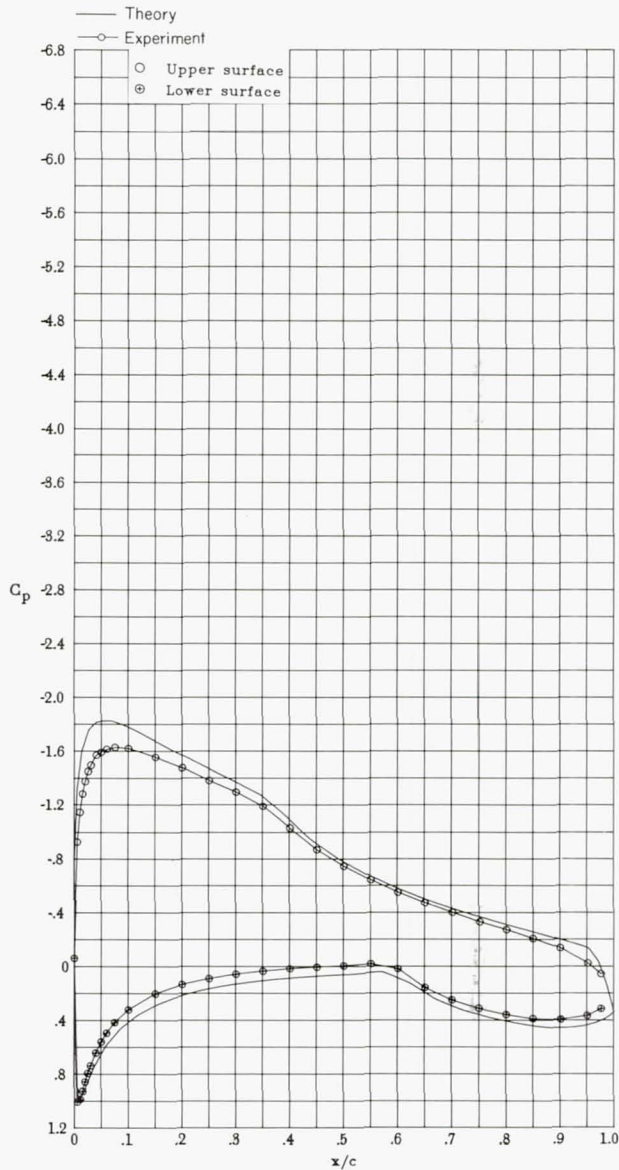


Figure 28.- Effect of blunt trailing edge on minimum drag coefficient for various Reynolds numbers. Open symbols represent data with transition free; solid symbols, data with transition fixed.

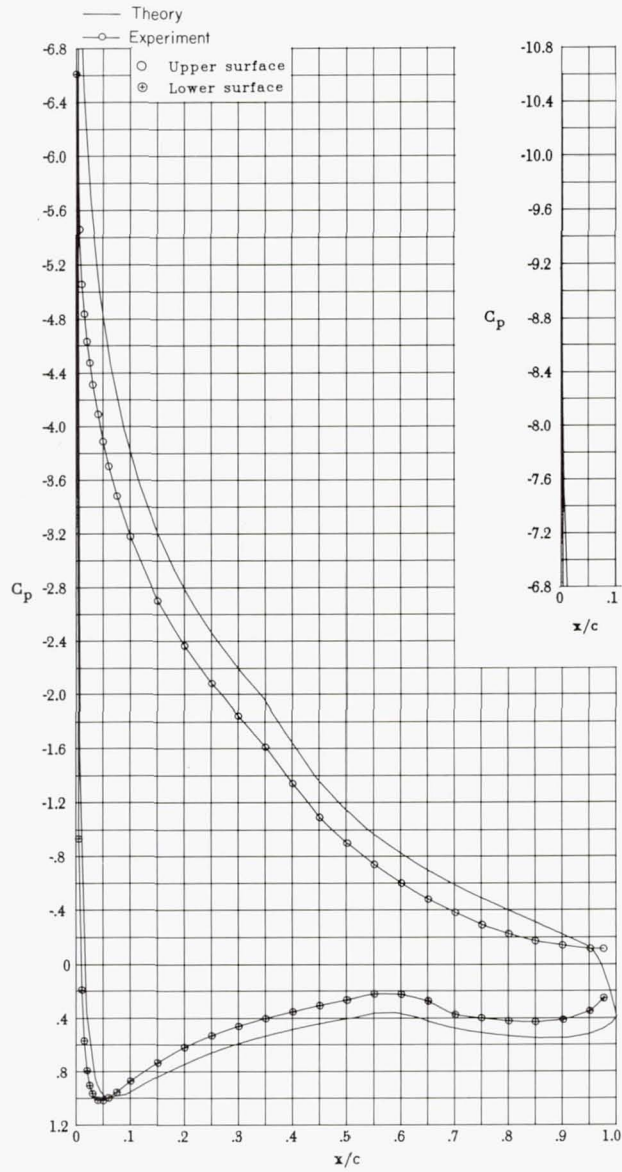


(a) $\alpha = 0.01^\circ$.



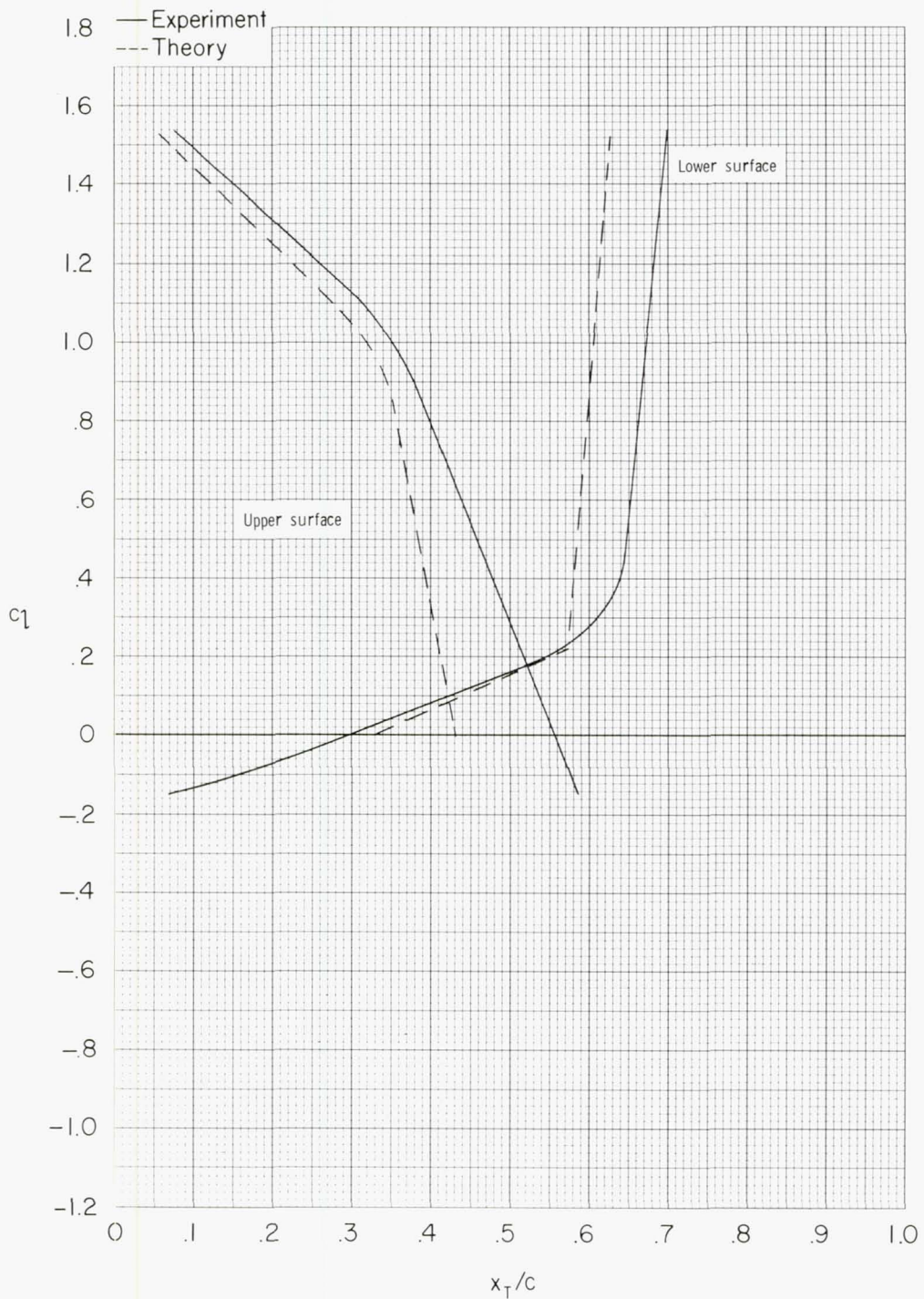
(b) $\alpha = 5.09^\circ$.

Figure 29.- Comparison of theoretical and experimental pressure distributions.



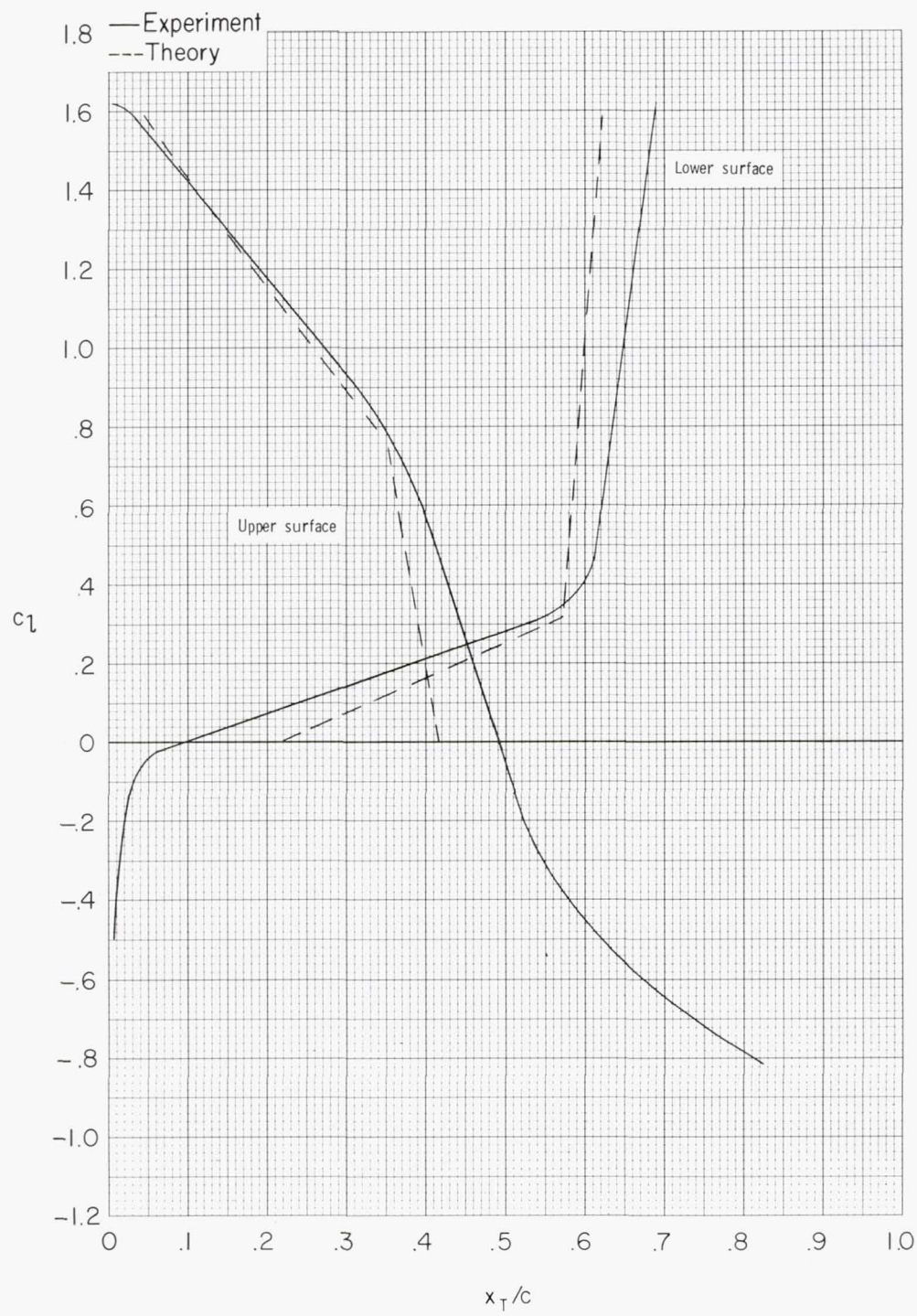
(c) $\alpha = 14.23^\circ$.

Figure 29.- Concluded.



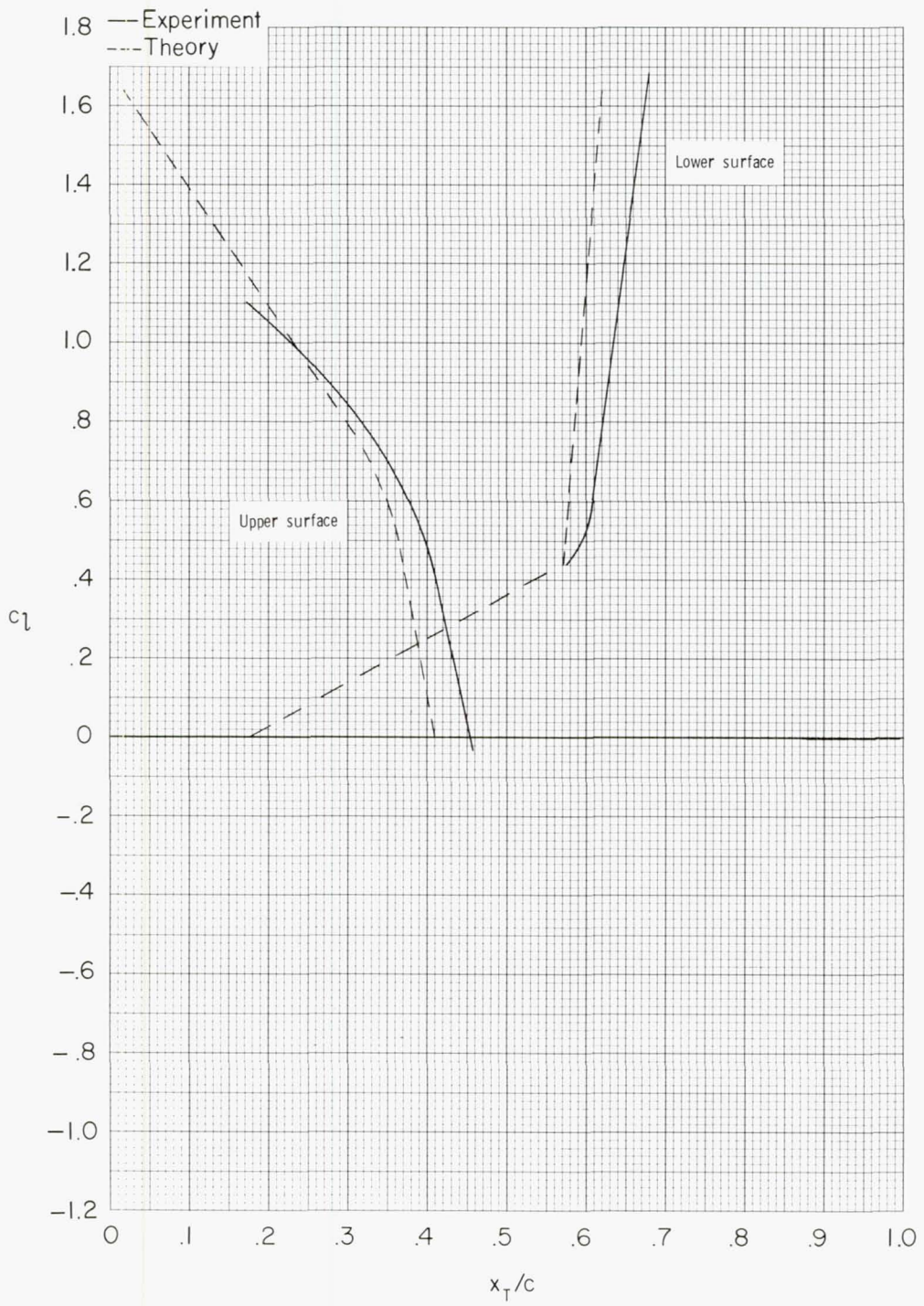
(a) $R = 1.0 \times 10^6$.

Figure 30.- Comparison of theoretical and experimental transition locations.



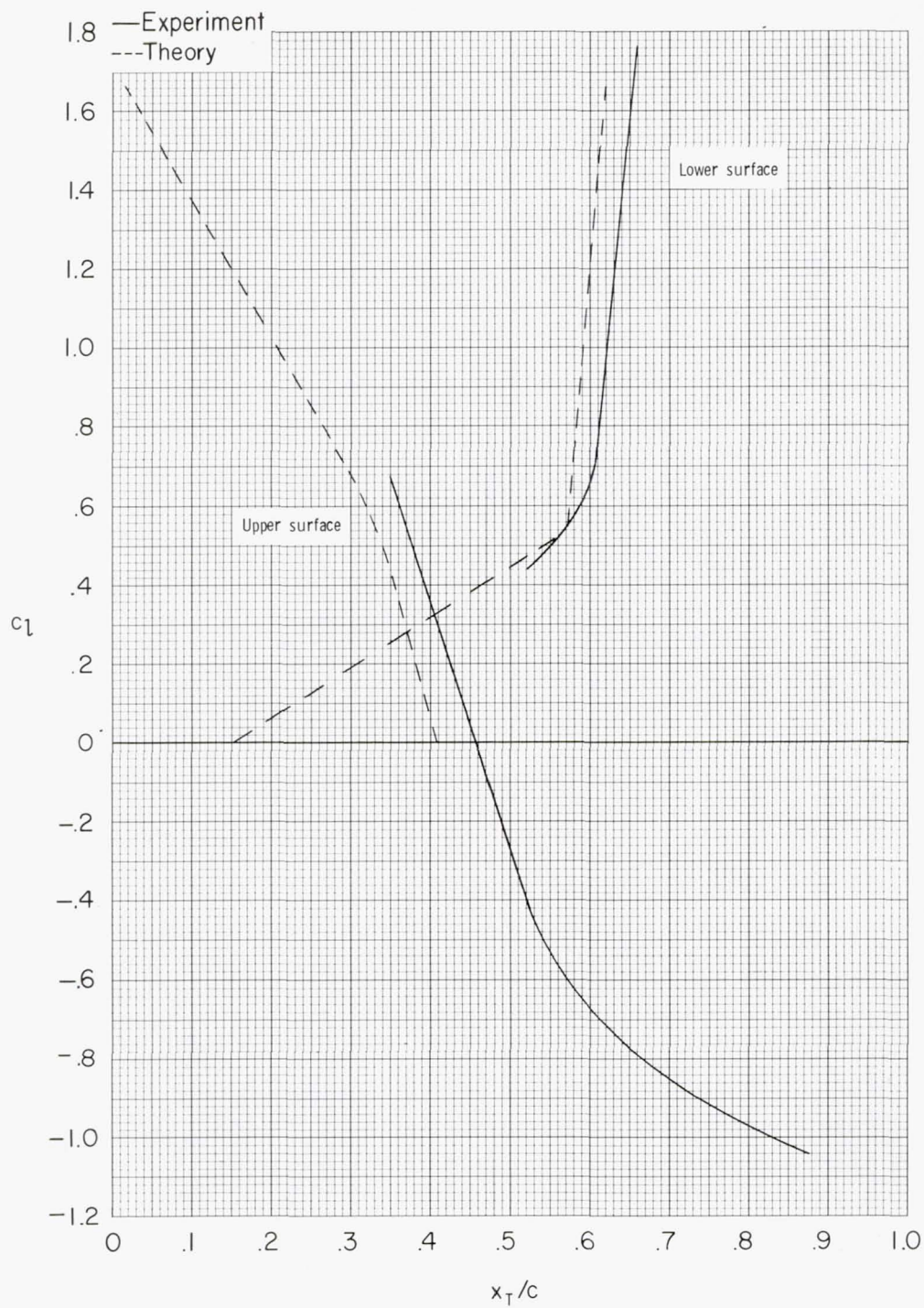
(b) $R = 2.0 \times 10^6$.

Figure 30.- Continued.



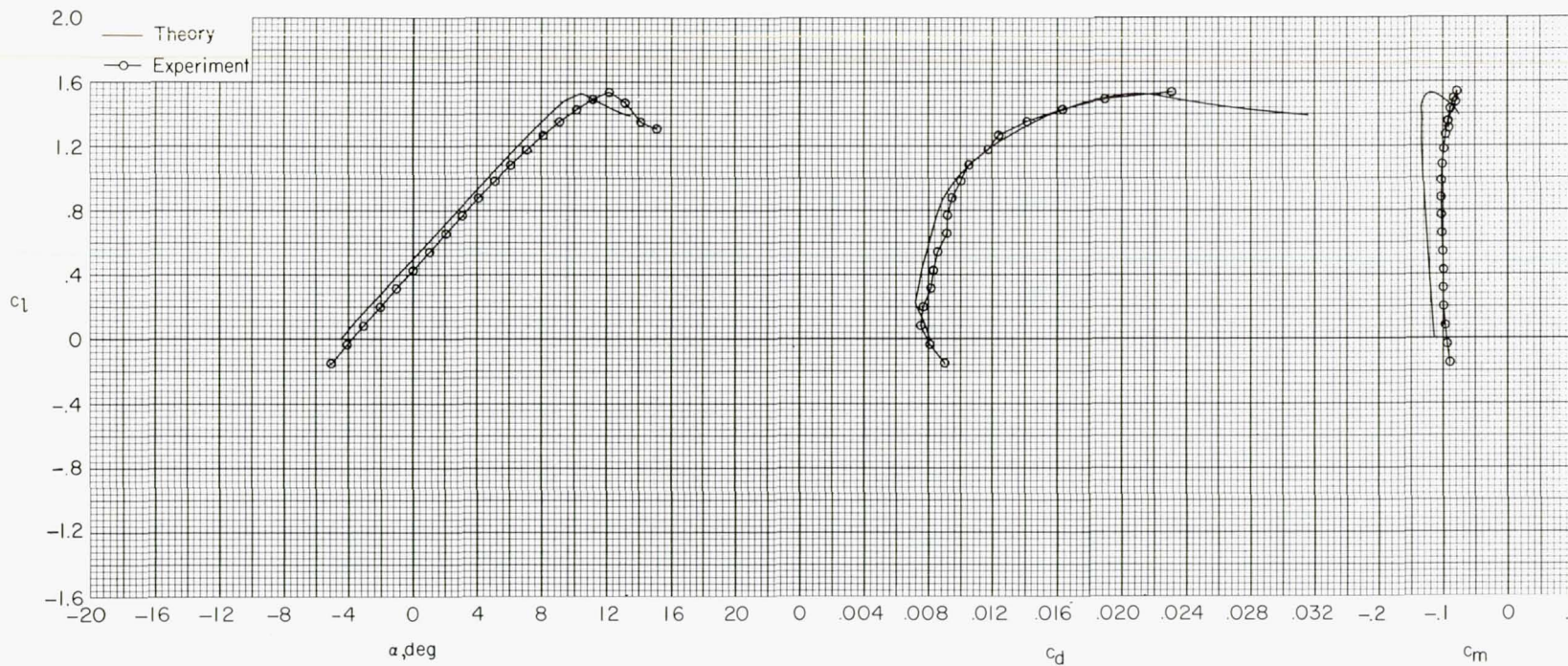
(c) $R = 3.0 \times 10^6$.

Figure 30.- Continued.



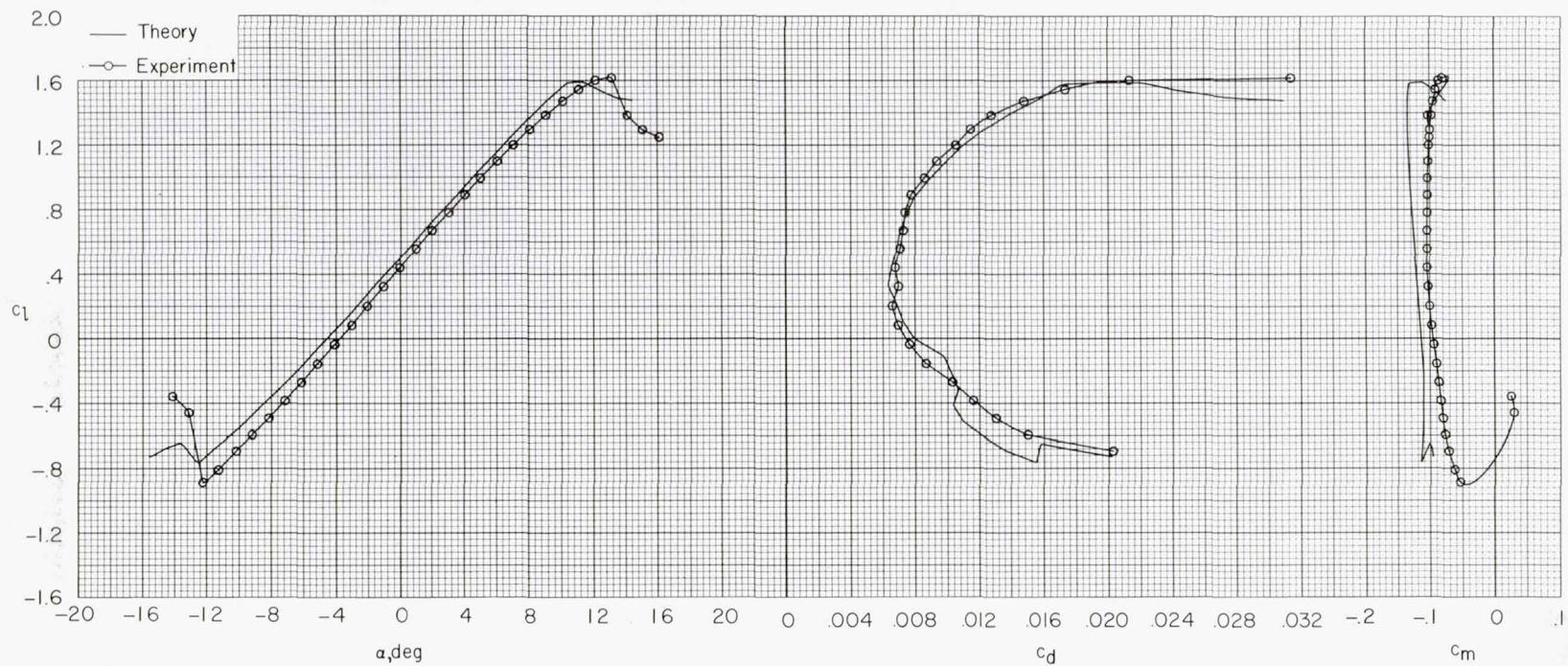
(d) $R = 4.0 \times 10^6$.

Figure 30.- Concluded.



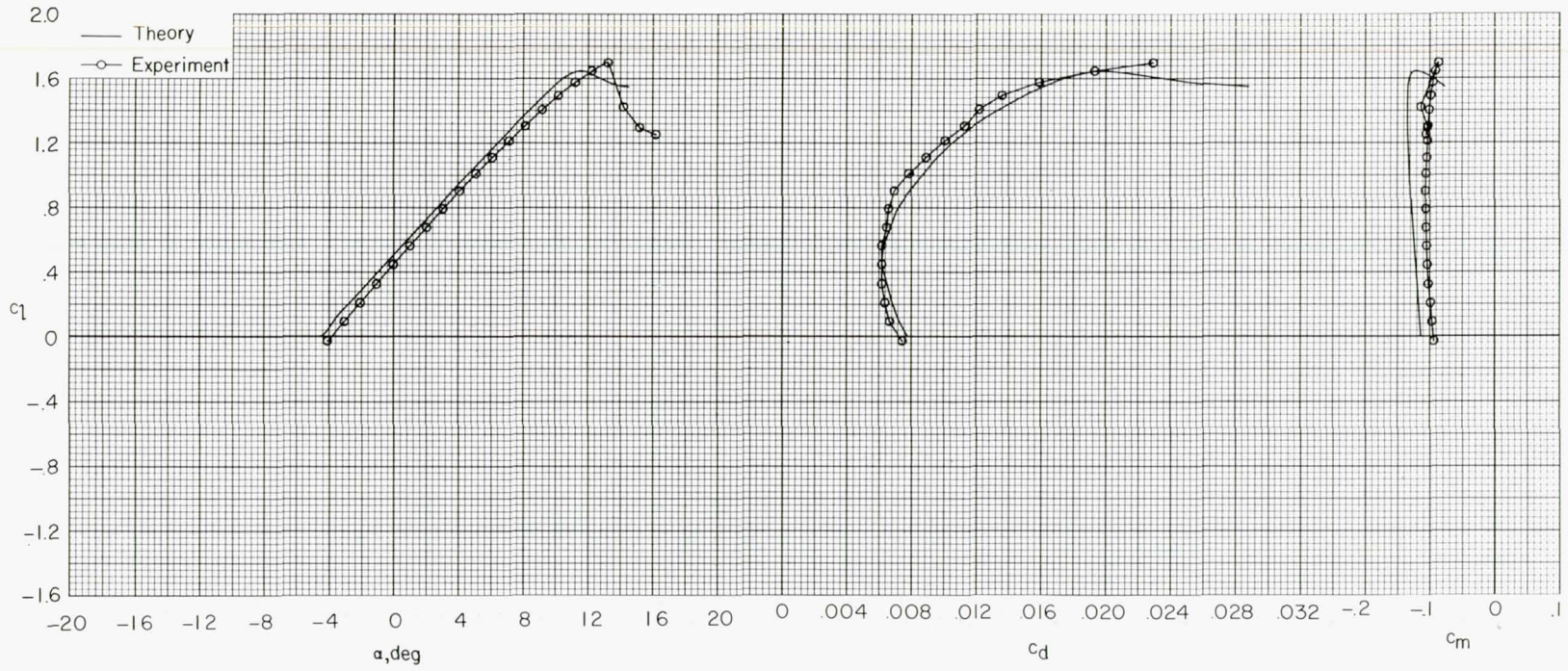
(a) $R = 1.0 \times 10^6$.

Figure 31.- Comparison of theoretical and experimental section characteristics with transition free.



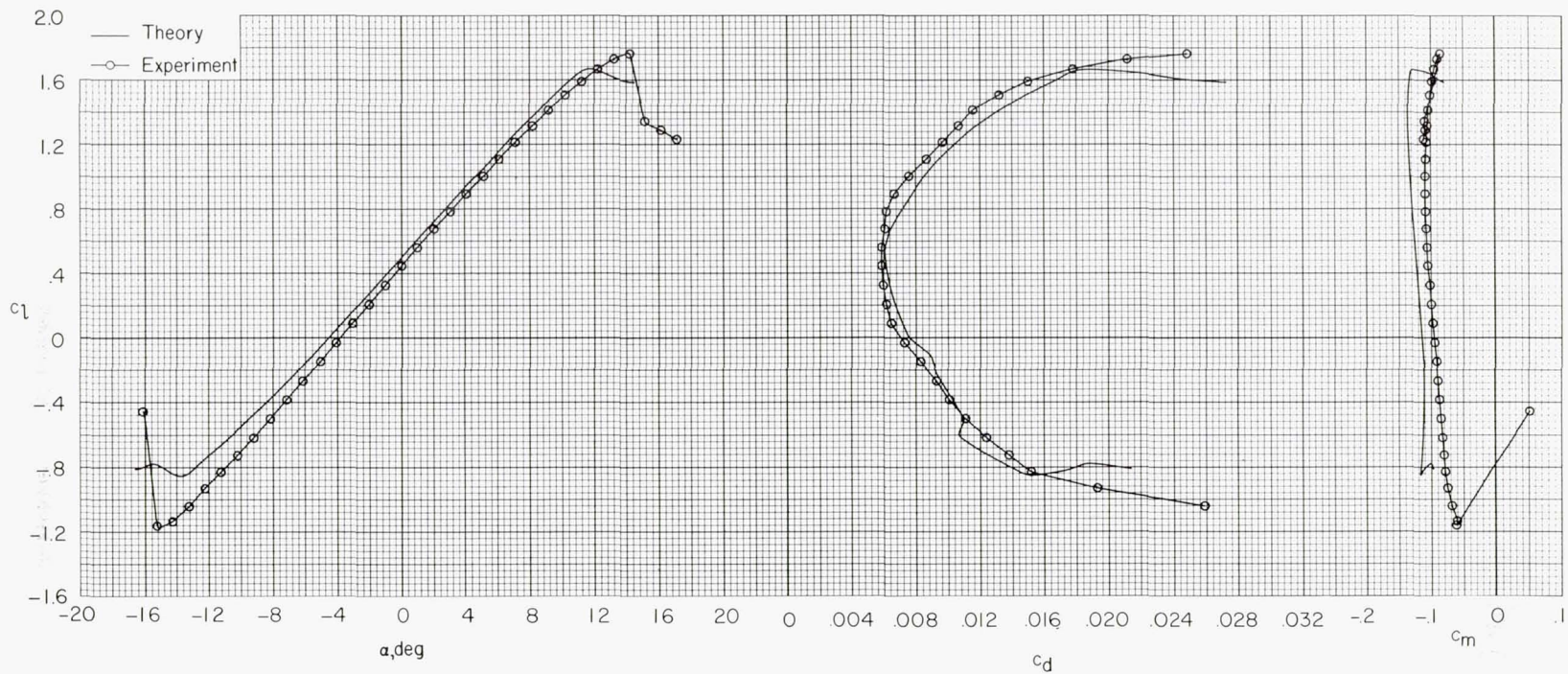
(b) $R = 2.0 \times 10^6$.

Figure 31.- Continued.



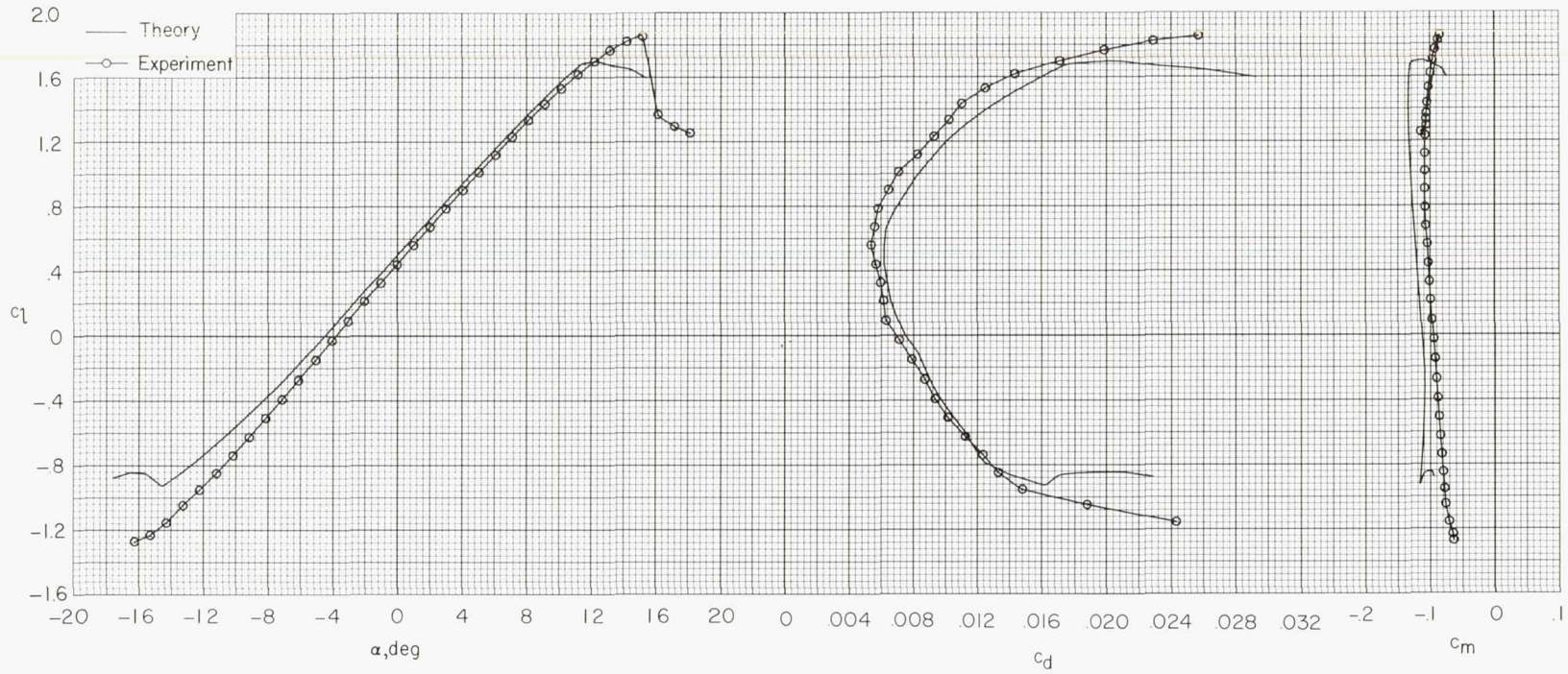
(c) $R = 3.0 \times 10^6$.

Figure 31.- Continued.



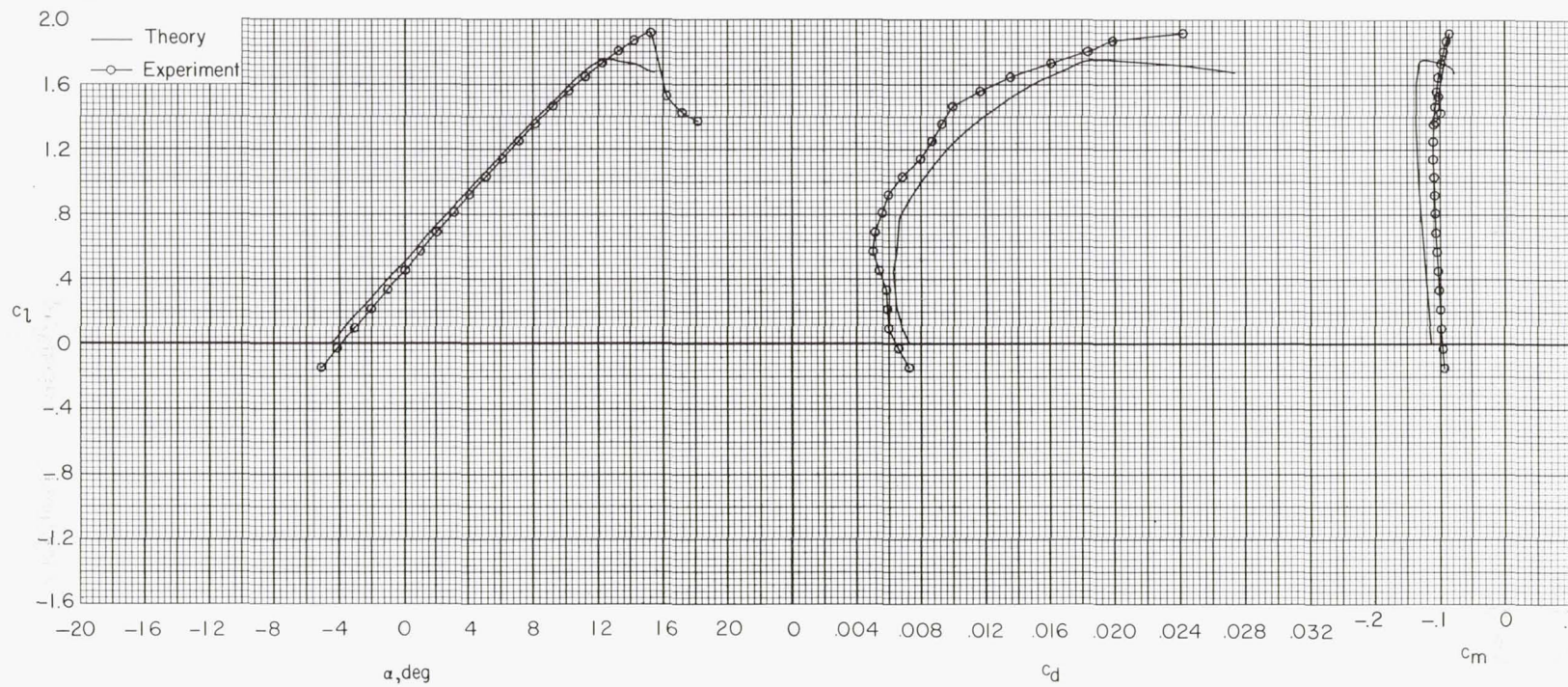
(d) $R = 4.0 \times 10^6$.

Figure 31.- Continued.



(e) $R = 6.0 \times 10^6$.

Figure 31.- Continued.



(f) $R = 9.0 \times 10^6$.

Figure 31.- Concluded.

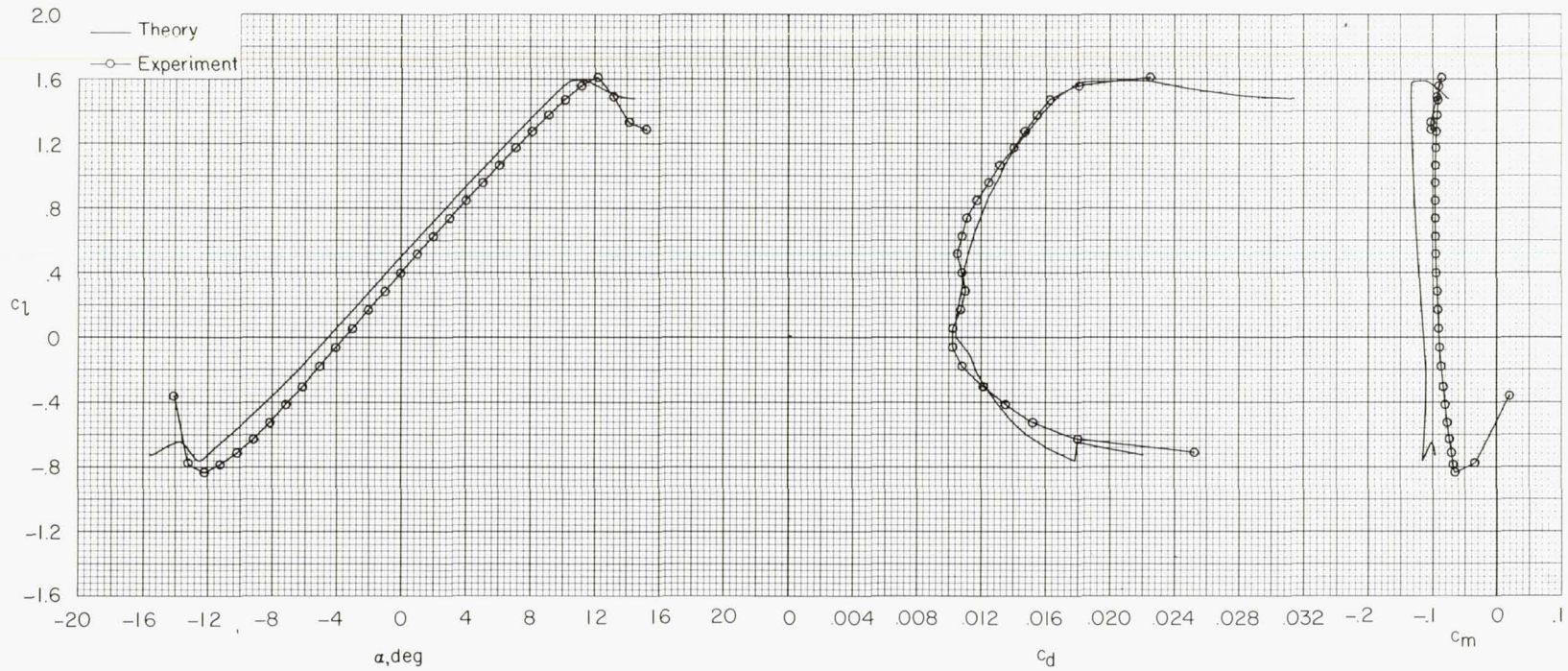
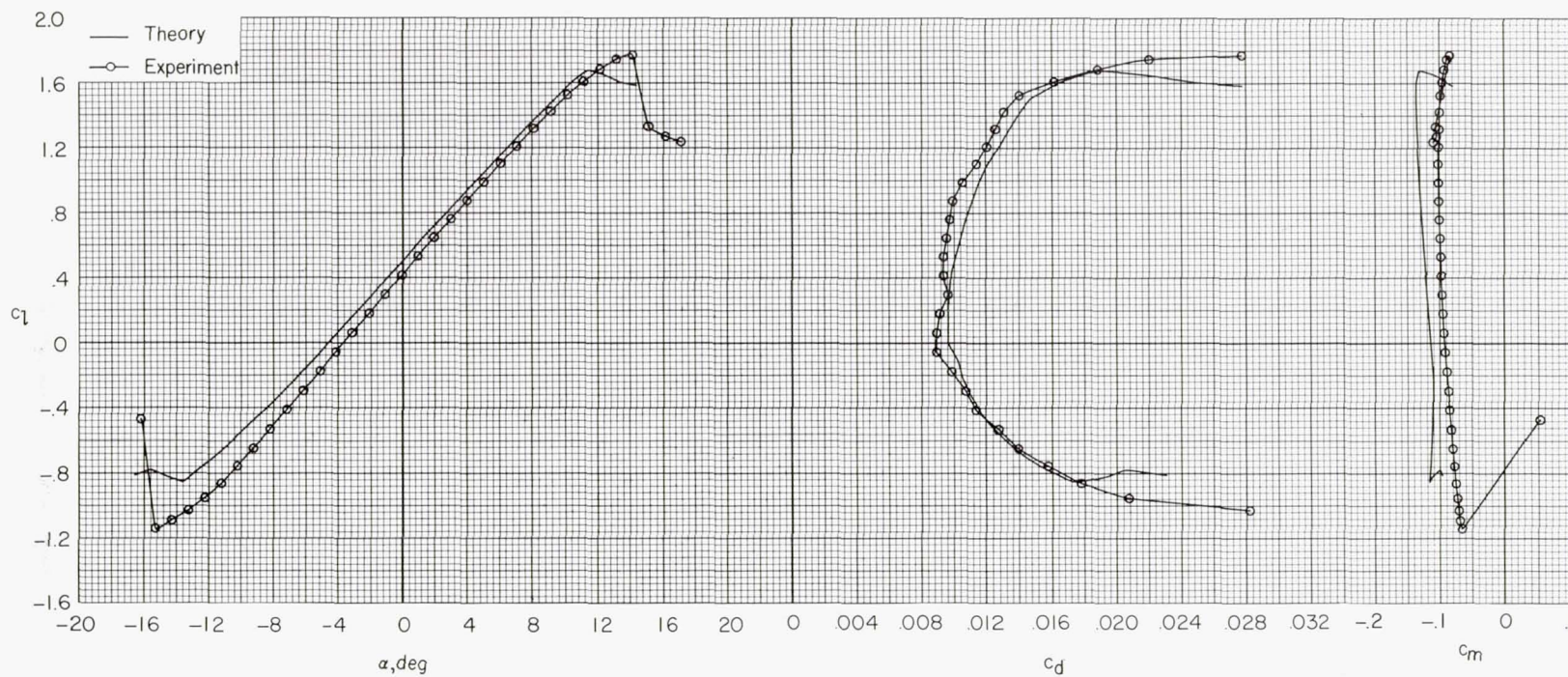
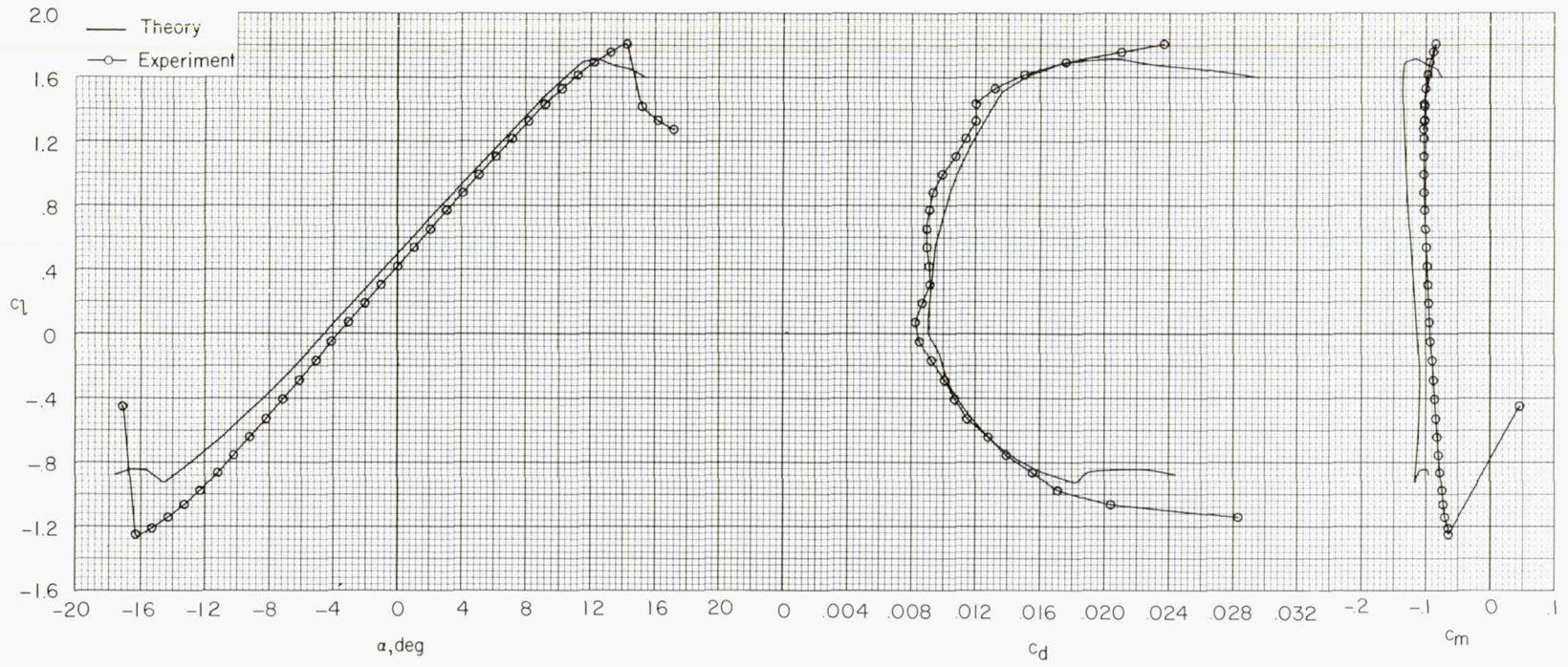
(a) $R = 2.0 \times 10^6$.

Figure 32.- Comparison of theoretical and experimental section characteristics with transition fixed.



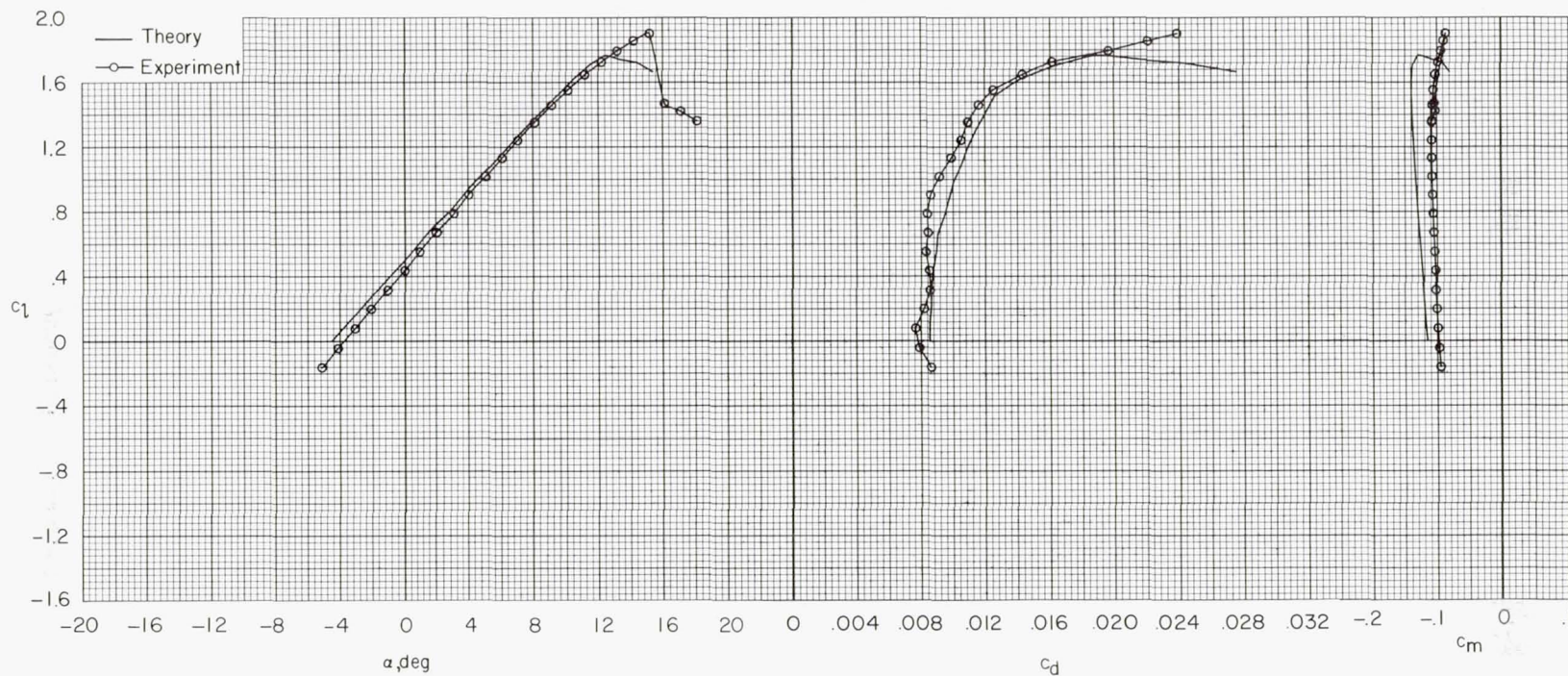
(b) $R = 4.0 \times 10^6$.

Figure 32.- Continued.



(c) $R = 6.0 \times 10^6$.

Figure 32.- Continued.



(d) $R = 9.0 \times 10^6$.

Figure 32.- Concluded.

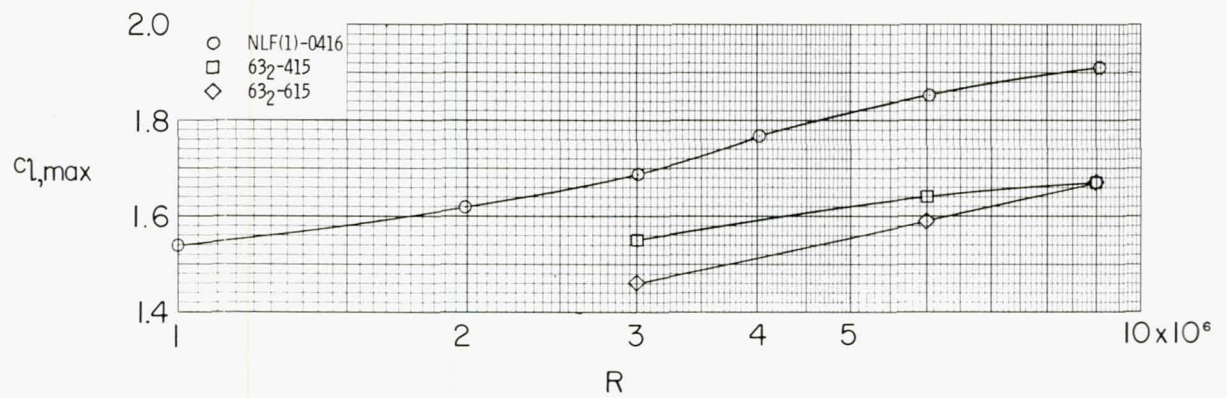


Figure 33.- Comparison of maximum lift coefficients for NLF(1)-0416 airfoil and NACA 632-415 and 632-615 airfoils.

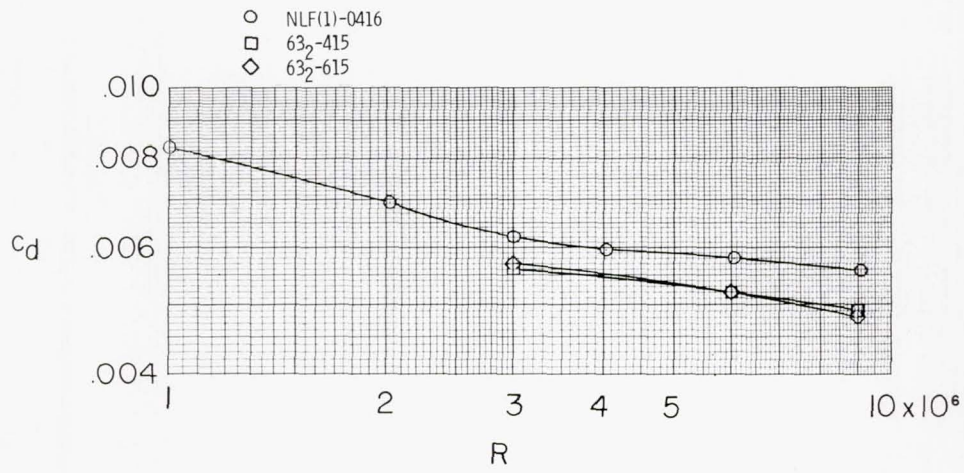


Figure 34.- Comparison of drag coefficients at $c_l = 0.4$ for NLF(1)-0416 airfoil and NACA 632-415 and 632-615 airfoils.

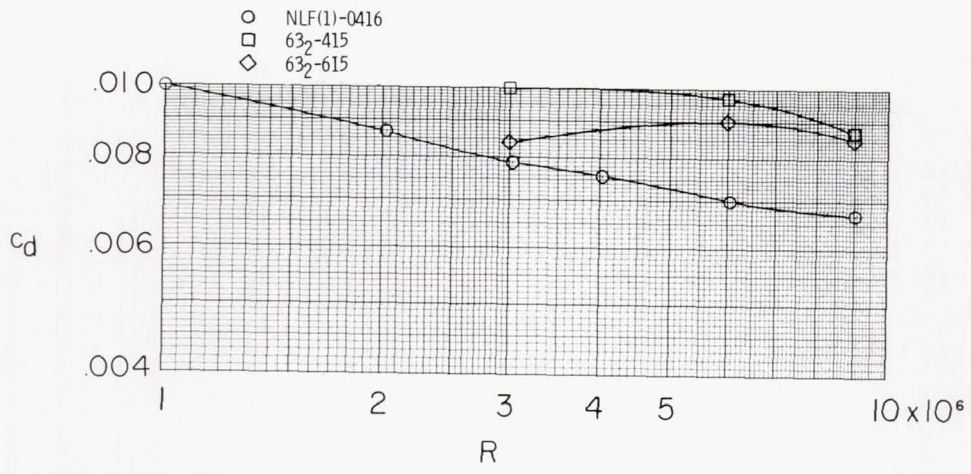


Figure 35.- Comparison of drag coefficients at $c_l = 1.0$ for NLF(1)-0416 airfoil and NACA 632-415 and 632-615 airfoils.

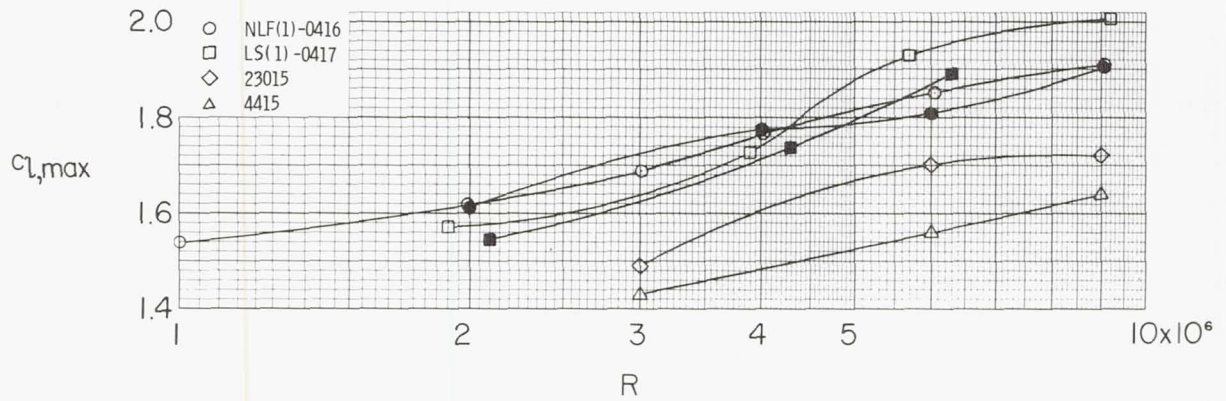


Figure 36.- Comparison of maximum lift coefficients for NLF(1)-0416, LS(1)-0417, NACA 23015, and NACA 4415 airfoils. Open symbols represent data with transition free; solid symbols, data with transition fixed.

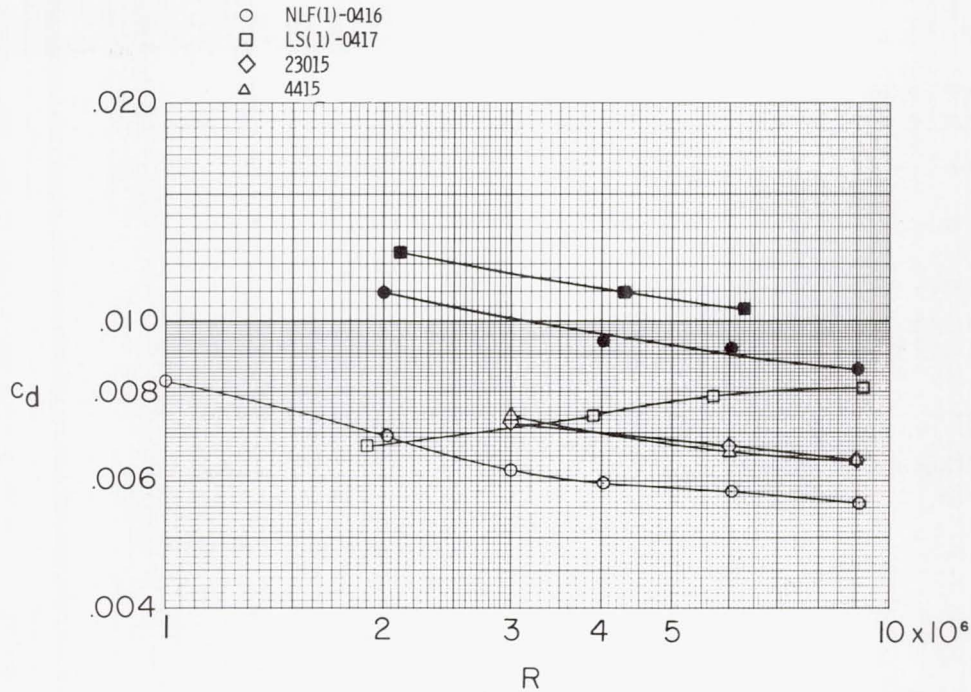


Figure 37.- Comparison of drag coefficients at $c_l = 0.4$ for NLF(1)-0416, LS(1)-0417, NACA 23015, and NACA 4415 airfoils. Open symbols represent data with transition free; solid symbols, data with transition fixed.

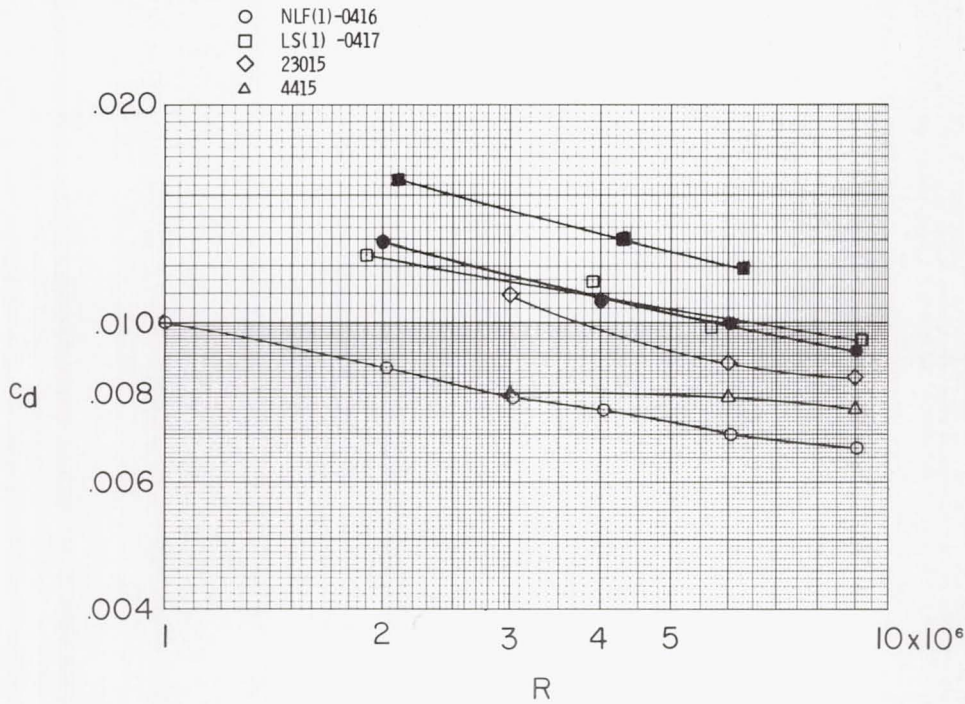


Figure 38.- Comparison of drag coefficients at $c_l = 1.0$ for NLF(1)-0416, LS(1)-0417, NACA 23015, and NACA 4415 airfoils. Open symbols represent data with transition free; solid symbols, data with transition fixed.

1. Report No. NASA TP-1861		2. Government Accession No.		3. Recipient's Catalog No.	
4. Title and Subtitle DESIGN AND EXPERIMENTAL RESULTS FOR A NATURAL-LAMINAR-FLOW AIRFOIL FOR GENERAL AVIATION APPLICATIONS				5. Report Date June 1981	
				6. Performing Organization Code 505-31-33-05	
7. Author(s) Dan M. Somers				8. Performing Organization Report No. L-14117	
				10. Work Unit No.	
9. Performing Organization Name and Address NASA Langley Research Center Hampton, VA 23665				11. Contract or Grant No.	
				13. Type of Report and Period Covered Technical Paper	
12. Sponsoring Agency Name and Address National Aeronautics and Space Administration Washington, DC 20546				14. Sponsoring Agency Code	
15. Supplementary Notes					
16. Abstract A new natural-laminar-flow airfoil for general aviation applications, the NLF(1)-0416, has been designed and analyzed theoretically and verified experimentally in the Langley Low-Turbulence Pressure Tunnel. The basic objective of combining the high maximum lift of the NASA low-speed airfoils with the low cruise drag of the NACA 6-series airfoils has been achieved. The safety requirement that the maximum lift coefficient not be significantly affected with transition fixed near the leading edge has also been met. Comparisons of the theoretical and experimental results show excellent agreement. Comparisons with other airfoils, both laminar flow and turbulent flow, confirm the achievement of the basic objective.					
17. Key Words (Suggested by Author(s)) NLF(1)-0416 Airfoils Low speed Laminar flow General aviation				18. Distribution Statement Unclassified - Unlimited Subject Category 02	
19. Security Classif. (of this report) Unclassified		20. Security Classif. (of this page) Unclassified		21. No. of Pages 101	22. Price A06